A&A 648, A127 (2021)
https://doi.org/10.1051/0004-6361/202039708
© ESO 2021

Astronomy & Astrophysics

Evidence for disequilibrium chemistry from vertical mixing in hot Jupiter atmospheres

A comprehensive survey of transiting close-in gas giant exoplanets with warm-*Spitzer*/IRAC

Claire Baxter[1], Jean-Michel Désert[1], Shang-Min Tsai[2], Kamen O. Todorov[1], Jacob L. Bean[3], Drake Deming[4], Vivien Parmentier[2], Jonathan J. Fortney[6], Michael Line[5], Daniel Thorngren[7], Raymond T. Pierrehumbert[2], Adam Burrows[8], and Adam P. Showman[9,10]

[1] Anton Pannekoek Institute for Astronomy, University of Amsterdam, Science Park 904, 1098 XH Amsterdam, The Netherlands
e-mail: c.j.baxter@uva.nl
[2] Atmospheric, Ocean, and Planetary Physics, Department of Physics, University of Oxford, Oxford, OX1 3PU, UK
[3] Department of Astronomy & Astrophysics, University of Chicago, 5640 S. Ellis Avenue, Chicago, IL 60637, USA
[4] Department of Astronomy University of Maryland at College Park, College Park, MD 20742, USA
[5] School of Earth & Space Exploration, Arizona State University, Tempe AZ 85287, USA
[6] Department of Astronomy and Astrophysics, University of California, Santa Cruz, CA 95064, USA
[7] Institut de Recherche sur les Exoplanètes, Université de Montréal, Canada
[8] Department of Astrophysical Sciences, Princeton University, 4 Ivy Lane, Princeton, NJ 08544, USA
[9] Department of Atmospheric and Oceanic Sciences, Peking University, Beijing, PR China
[10] Department of Planetary Sciences and Lunar and Planetary Laboratory, The University of Arizona, 1629 University Blvd., Tucson, AZ 85721 USA

Received 17 October 2020 / Accepted 9 February 2021

ABSTRACT

Aims. We present a large atmospheric study of 49 gas giant exoplanets using infrared transmission photometry with *Spitzer*/IRAC at 3.6 and 4.5 μm.

Methods. We uniformly analyze 70 photometric light curves of 33 transiting planets using our custom pipeline, which implements pixel level decorrelation. Augmenting our sample with 16 previously published exoplanets leads to a total of 49. We use this survey to understand how infrared photometry traces changes in atmospheric chemical properties as a function of planetary temperature. We compare our measurements to a grid of 1D radiative-convective equilibrium forward atmospheric models which include disequilibrium chemistry. We explore various strengths of vertical mixing (K_{zz} = 0–10^{12} cm^2 s^{-1}) as well as two chemical compositions (1x and 30x solar).

Results. We find that, on average, *Spitzer* probes a difference of 0.5 atmospheric scale heights between 3.6 and 4.5 μm, which is measured at 7.5σ level of significance. Changes in the opacities in the two *Spitzer* bandpasses are expected with increasing temperature due to the transition from methane-dominated to carbon-monoxide-dominated atmospheres at chemical equilibrium. Comparing the data with our model grids, we find that the coolest planets show a lack of methane compared to expectations, which has also been reported by previous studies of individual objects. We show that the sample of coolest planets rule out 1x solar composition with >3σ confidence while supporting low vertical mixing (K_{zz} = 10^8 cm^2 s^{-1}). On the other hand, we find that the hot planets are best explained by models with 1x solar metallicity and high vertical mixing (K_{zz} = 10^{12} cm^2 s^{-1}). We interpret this as the lofting of CH_4 to the upper atmospheric layers. Changing the interior temperature changes the expectation for equilibrium chemistry in deep layers, hence the expectation of disequilibrium chemistry higher up. We also find a significant scatter in the transmission signatures of the mid-temperate and ultra-hot planets, likely due to increased atmospheric diversity, without the need to invoke higher metallicities. Additionally, we compare *Spitzer* transmission with emission in the same bandpasses for the same planets and find no evidence for any correlation. Although more advanced modelling would test our conclusions further, our simple generic model grid points towards different amounts of vertical mixing occurring across the temperature range of hot Jupiters. This finding also agrees with the observed scatter with increasing planetary magnitude seen in *Spitzer*/IRAC color-magnitude diagrams for planets and brown dwarfs.

Key words. planets and satellites: atmospheres – planets and satellites: composition – planets and satellites: gaseous planets – surveys – techniques: photometric

1. Introduction

Studying exoplanets is critical in order to gain insight into the dominant composition and physical atmospheric processes and for understanding the theory of planet formation and evolution (Seager & Deming 2010; Crossfield 2015; Deming & Seager 2017). Hot Jupiters with large scale heights are ideal targets for detecting molecular signatures in their atmospheres via transmission spectroscopy (Seager & Sasselov 2000; Brown 2001). The atmospheres of such planets have been studied across a large

range of wavelengths with a myriad of different instruments. Given the number of exoplanet atmospheres already observed, we now enter the era of statistical study of exoplanet atmospheres (e.g., Triaud 2014; Beatty et al. 2014; Gao et al. 2020; Keating et al. 2019; Garhart et al. 2020; Baxter et al. 2020; Fu et al. 2017; Tsiaras et al. 2018; Wallack et al. 2019).

Wavelength-dependent transit depths are in principle primarily sensitive to the atmospheric composition (Seager & Sasselov 2000), but in practice these observations have often been plagued by the presence of clouds/hazes dampening the expected molecular signals (e.g., Fortney 2005; Sing et al. 2016; Barstow et al. 2017). Nevertheless, Cloud-free hot Jupiter atmospheres in chemical equilibrium are predicted to exhibit traces of water, carbon monoxide, and methane (Seager & Sasselov 2000; Fortney 2005; Fortney et al. 2010). Studies are conducted to demonstrate whether such elements are statistically and systematically observed in exoplanets (Tsai et al. 2018). However, non-equilibrium chemistry and clouds are predicted to be present in close-in giant exoplanet atmospheres, and will impact their observations (e.g., Agúndez et al. 2012; Drummond et al. 2016; Steinrueck et al. 2019). Sing et al. (2016) performed a mini-survey of the transmission spectra of ten hot Jupiters, which they characterize in terms of a cloud index, and found a transition between cloudy and cloud-free atmospheres. They note that a temperature-pressure profile crossing a condensation curve is not solely responsible for the resulting dampened spectra, but rather it is likely that nonequilibrium effects such as atmospheric circulation and vertical mixing play a role.

There are several important atmospheric processes to consider that can drive atmospheres away from cloud-free chemical equilibrium. Zhang et al. (2018) showed that atmospheric transport can move atmospheric abundances away from chemical equilibrium and greatly alter the expected spectroscopic observations. They develop a 1D framework to capture these complex atmospheric processes and parameterize it with an eddy diffusion co-efficient (K_{zz}). For hot Jupiters, K_{zz} ranges from 10^8 to 10^{12} cm^2 s^{-1} according to estimations of the mean vertical wind in global circulation models (GCMS; Moses et al. 2011; Parmentier et al. 2013). Additionally, Komacek et al. (2019) estimated that the strength of vertical mixing will increase for hotter planets. Particularly relevant to this work is the recent advances made in the field of brown dwarf atmospheres: Miles et al. (2020) study the strength of vertical mixing in cool brown dwarf atmospheres with temperatures of 250–750 K, and find that the cooler objects support mixing close to the theoretical maximum yet the warmer objects show weaker than predicted mixing.

Additionally, the atmospheres of warm giant close-in exoplanets seem to be deficient in methane. According to equilibrium chemistry, methane is predicted to be abundant in the atmospheres of exoplanets with equilibrium temperatures cooler than 1100 K (Madhusudhan 2012). In this context, Stevenson et al. (2010b) showed that the atmosphere of GJ436b is substantially methane deficient relative to chemical equilibrium models, suggesting the presence of nonequilibrium processes such as those induced by vertical mixing, which has been tested by follow-up studies (Knutson et al. 2011; Lanotte et al. 2014). Several other studies have attempted to model the methane depletion of GJ 436b: using nonequilibrium photochemical models (Line et al. 2011), high-metallicity (230–1000x solar) models (Moses et al. 2013), models with hydrogen depletion (Hu et al. 2015), and invoking tidal heating due to high eccentricity (Agúndez et al. 2014). Morley et al. (2017) provide new data along with a reanalysis and new modeling, and confirm the methane depletion and find the best-fitting models have high metallicity, disequilibrium chemistry, and tidal heating resulting in an intrinsic temperature ($T_{\rm int}$) of 300–350 K. $T_{\rm int}$ characterizes the heat flux escaping from the planetary interior, which is written as $\sigma T_{\rm int}^4$. Recently, Fortney et al. (2020) suggested that the ongoing eccentricity damping of three warm Neptunes, including GJ 436b, heats their atmospheres and drives strong convective mixing resulting in a decreased CH_4/CO ratio.

Furthermore, methane depletion has been observed in a slew of other warm giant planets. HST/WFC3 observations of the transmission spectra of both WASP-107b and WASP-117 b reveal no detection of methane expected from chemical equilibrium, but only upper limits, suggesting a methane depletion in these atmospheres (Kreidberg et al. 2018b; Spake et al. 2018; Carone et al. 2021). Additionally, combined HST/WFC3 and *Spitzer*/IRAC transmission spectra observations of GJ3470 b (Benneke et al. 2019), HAT-P-11 b (Chachan et al. 2019), HAT-P-26 b (Wakeford et al. 2017), and WASP-39 b (Wakeford et al. 2018) all have lower-than-expected abundances of methane given their temperatures. All in all, methane has only been sparsely detected in the atmospheres of a few exoplanets (Swain et al. 2008; Tinetti et al. 2010; Guilluy et al. 2019).

In this paper, we aim to statistically characterize a large sample of hot Jupiters using the two remaining active detectors on *Spitzer*/IRAC at 3.6 and 4.5 μm. (Fazio et al. 2004; Werner et al. 2004). At these two wavelengths, we expect to see the absorption of methane (CH_4) and carbon monoxide or carbon dioxide (CO or CO_2) respectively. We uniformly analyze *Spitzer*/IRAC photometric transit light curves of a survey of 34 gas giant planets. This survey represents the largest analysis of *Spitzer*/IRAC observations of gas giants in transmission to date, and spans equilibrium temperatures from 500 to 2700 K.

This paper is organized as follows: In Sect. 2 we describe the observations and the survey of planets. In Sect. 3 we describe the data reduction, photometric extraction, light-curve fitting, and the creation of our grid of 1D atmospheric models. Section 4 describes the results for the transit survey and the statistical survey comparison to the grid of models. In Sect. 5 we discuss the context and implications for the different trends and statistics that we observe. Additionally, in Sect. 5 we describe the collection and combination of the secondary eclipse data with *Gaia* distances and discuss our comparison between transits and eclipses.

2. Observations

As part of the survey programs 90092 (PI: Desert) and 13044 (PI: Deming), we present the transit depth analysis using 70 transit light curves of 33 planets in the Post Cryogenic Warm *Spitzer*/IRAC bandpasses of 3.6 and 4.5 μm. With the goal of gaining a stronger understanding of the origins and nature of the exoplanets already discovered, we designed the survey to probe a wide range of masses, radii, and equilibrium temperatures: ranging from cooler long-period gas giants (~200 K) from the *Kepler* mission to close-in hot Jupiters (up to 2300 K). Table 1 presents the observational information for the 33 planets in the survey. These exoplanets were selected due to their high expected signal-to-noise ratio (S/N) and, in the case of the *Kepler* planets, their multiplicity. Additionally, we augment this sample with two extra planets to probe the coolest and the hottest regions of parameter space; these are WASP-121b from program 13044 (PI: Deming) and WASP-107b from program 13052 (PI: Werner). A full list of the observations is displayed in Table 1.

All observations from our survey were taken in "peak-up" mode, meaning the main observation was preceded by a 30-min peak-up observation allowing for accurate pointing, allowing us

Table 1. Details of the *Spitzer* observations used in our survey analysis.

Target	λ μm	UT start date	Duration hours	Program ID	Target	λ μm	UT start date	Duration hours	Program ID
GJ3470 b	4.5	2013 Jan. 01	4.4	90092	WASP-17 b	4.5	2013 May 14	8.2	90092
GJ3470 b	3.6	2012 Dec. 22	4.4	90092	WASP-17 b	3.6	2013 May 10	8.2	90092
HAT-P-12 b	4.5	2013 Mar. 11	4.5	90092	WASP-1 b	4.5	2013 Mar. 20	6.8	90092
HAT-P-12 b	3.6	2013 Mar. 08	4.5	90092	WASP-1 b	3.6	2013 Mar. 10	6.8	90092
HAT-P-18 b	3.6	2013 Jun. 17	5.0	90092	WASP-21 b	4.5	2013 Sep. 01	6.1	90092
HAT-P-18 b	4.5	2013 Jul. 09	5.0	90092	WASP-21 b	3.6	2013 Aug. 27	6.1	90092
HAT-P-1 b	4.5	2013 Sep. 20	5.2	90092	WASP-29 b	4.5	2017 Mar. 14	7.8	13044
HAT-P-1 b	3.6	2013 Sep. 11	5.2	90092	WASP-29 b	3.6	2017 Feb. 22	7.8	13044
HAT-P-26 b	3.6	2013 Sep. 09	4.5	90092	WASP-31 b	4.5	2013 Mar. 19	4.6	90092
HAT-P-26 b	4.5	2013 Apr. 23	4.5	90092	WASP-31 b	3.6	2013 Mar. 09	4.6	90092
HAT-P-32 b	3.6	2012 Nov. 18	5.4	90092	WASP-34 b	4.5	2013 Mar. 25	4.5	90092
HAT-P-32 b	4.5	2013 Mar. 18	5.4	90092	WASP-34 b	3.6	2013 Mar. 17	4.5	90092
HAT-P-41 b	3.6	2017 Jan. 18	12.1	13044	WASP-36 b	3.6	2017 Feb. 20	7.3	13044
HAT-P-41 b	4.5	2017 Feb. 03	12.1	13044	WASP-36 b	4.5	2017 Aug. 10	7.3	13044
HATS-7 b	4.5	2016 Nov. 04	5.2	13044	WASP-39 b	4.5	2013 Oct. 10	5.0	90092
HATS-7 b	3.6	2016 Nov. 01	5.2	13044	WASP-39 b	3.6	2013 Apr. 18	5.0	90092
KELT-7 b	4.5	2017 Jan. 04	10.3	13044	WASP-4 b	4.5	2012 Dec. 31	4.3	90092
KELT-7 b	3.6	2016 Dec. 27	10.3	13044	WASP-4 b	3.6	2012 Dec. 27	4.3	90092
Kepler-45 b	4.5	2013 Sep. 29	4.5	90092	WASP-62 b	3.6	2016 Nov. 24	11.3	13044
Kepler-45 b	3.6	2013 Sep. 22	4.5	90092	WASP-62 b	4.5	2016 Dec. 07	11.3	13044
Kepler-45 b	4.5	2013 Sep. 12	4.5	90092	WASP-63 b	4.5	2017 Jun. 17	15.8	13044
Kepler-45 b	3.6	2013 Sep. 07	4.5	90092	WASP-63 b	3.6	2017 Apr. 21	15.8	13044
Kepler-45 b	3.6	2013 Oct. 16	4.5	90092	WASP-67 b	3.6	2017 Jan. 22	5.6	13044
Kepler-45 b	4.5	2013 Nov. 15	4.5	90092	WASP-67 b	4.5	2017 Aug. 13	5.6	13044
Kepler-45 b	4.5	2013 Aug. 21	4.5	90092	WASP-69 b	4.5	2017 Aug. 30	6.5	13044
Kepler-45 b	3.6	2013 Aug. 06	4.5	90092	WASP-69 b	3.6	2017 Aug. 26	6.5	13044
TrES-2 b	4.5	2012 Nov. 26	4.3	90092	WASP-6 b	3.6	2013 Jan. 21	4.6	90092
TrES-2 b	3.6	2012 Nov. 21	4.3	90092	WASP-6 b	4.5	2013 Jan. 14	4.6	90092
WASP-101 b	4.5	2017 Jan. 17	8.0	13044	WASP-74 b	4.5	2017 Jan. 16	6.7	13044
WASP-101 b	3.6	2017 Jan. 06	8.0	13044	WASP-74 b	3.6	2017 Jan. 14	6.7	13044
WASP-107 b	3.6	2017 May 02	8.7	13052	WASP-79 b	4.5	2016 Nov. 27	11.1	13044
WASP-107 b	4.5	2017 Apr. 26	8.7	13052	WASP-79 b	3.6	2016 Nov. 20	11.1	13044
WASP-121 b	4.5	2017 Jun. 05	8.5	13044	WASP-94 Ab	3.6	2017 Feb. 10	13.3	13044
WASP-121 b	3.6	2017 Jun. 02	8.5	13044	WASP-94 Ab	4.5	2017 Aug. 06	13.3	13044
WASP-131 b	4.5	2017 Jun. 04	11.3	13044	XO-1 b	4.5	2013 May 25	5.4	90092
WASP-131 b	3.6	2016 Nov. 04	11.3	13044	XO-1 b	3.6	2013 May 13	5.4	90092
WASP-13 b	3.6	2013 Jul. 07	7.5	90092	XO-2 b	3.6	2013 Jan. 02	4.9	90092
WASP-13 b	4.5	2013 Jan. 22	7.5	90092	XO-2 b	4.5	2012 Dec. 31	4.9	90092

Notes. Columns are: UT date of observation, duration of observation in hours, and program ID of each transit.

to obtain precise positioning of the target to within 0.1 pixels throughout the observations. This significantly reduces the ramp effect caused by the intrapixel sensitivity (discussed in Sect. 3.1.2).

We expand our survey to other transiting planets for which the transit depths in the *Spitzer* bandpasses are taken from the literature. First, we performed a search on `exoplanets.org` (Wright et al. 2011) which yielded 3.6 and 4.5 μm transits for 16 additional planets. Combining these with our survey allows us to gain insights into the current state of infrared exoplanet transmission spectra in a statistical manner. These additional planets and their transit depths are listed in Table 2. Figure 1 presents a visualization of the parameter space covered by all the planets in our survey (analyzed and literature).

WASP-6b and WASP-34b are part of the original survey program 90092, but we exclude them from our analysis because the transits were missed. In the case of WASP-6b, the predicted mid-transit times had a large degree of uncertainty on the ephemeris, and the observed transits in both channels did not have sufficient baseline to gain accurate constraints on the atmosphere. In the case of WASP-34b, both transits were missed due to an error in the ephemeris.

3. Analysis

3.1. Transit light-curve analysis

3.1.1. Extracting *Spitzer* photometric light curves

We designed a custom pipeline to produce a photometric light curve from the Basic Calibrated Data frames produced by the *Spitzer* level 1 pipeline. As is standard for these data, our pipeline corrects dark current, flat fields, corrects for pixel nonlinearity, and converts to flux units.

We first calculate the mid-exposure timing of each data point in our transit light curves using the UTC-based MBJD values

Table 2. *Spitzer* measurements at 3.6 and 4.5 μm for planets that have already been published.

Planet	T_{eq} (K)	$\delta_{3.6}$ (%)	$\delta_{4.5}$ (%)	References
GJ 1214 b	560 ± 30	1.354 ± 0.009	1.367 ± 0.004	1
GJ 436 b	649 ± 59	0.695 ± 0.011	0.705 ± 0.012	2, 16
HAT-P-11 b	871 ± 16	0.338 ± 0.002	0.336 ± 0.003	3
HAT-P-7 b	2225 ± 41	0.629 ± 0.024	0.604 ± 0.012	4
HD 149026 b	1673 ± 65	0.269 ± 0.004	0.253 ± 0.004	5
HD 189733 b	1200 ± 22	2.405 ± 0.008	2.416 ± 0.011	6
HD 209458 b	1446 ± 19	1.481 ± 0.012	1.466 ± 0.007	7
WASP-103 b	2505 ± 78	1.401 ± 0.033	1.433 ± 0.026	8
WASP-12 b	2584 ± 91	1.341 ± 0.02	1.306 ± 0.031	9
WASP-14 b	1864 ± 60	0.887 ± 0.013	0.888 ± 0.013	10
WASP-18 b	2398 ± 73	0.959 ± 0.057	0.972 ± 0.049	11
WASP-19 b	2066 ± 46	1.957 ± 0.05	2.036 ± 0.051	4
WASP-33 b	2694 ± 53	1.166 ± 0.022	1.061 ± 0.023	5
WASP-43 b	1375 ± 79	2.496 ± 0.009	2.525 ± 0.016	12
WASP-80 b	775 ± 25	2.937 ± 0.013	2.969 ± 0.014	13
K2-25b	482 ± 20	1.143 ± 016	1.158 ± 018	14
HD97658b	733 ± 23	074 ± 002	08 ± 002	15
HAT-P-2 b	1540 ± 30	0.465 ± 01	0.496 ± 008	17

Notes. We include these measurements in our survey.
References. (1) Fraine et al. (2013); (2) Knutson et al. (2011); (3) Chachan et al. (2019); (4) Wong et al. (2016); (5) Zhang et al. (2018); (6) Pont et al. (2013); (7) Sing et al. (2016); (8) Kreidberg et al. (2018a); (9) Stevenson et al. (2014); (10) Wong et al. (2015); (11) Maxted et al. (2013); (12) Stevenson et al. (2016); (13) Triaud et al. (2015); (14) Thao et al. (2020); (15) Guo et al. (2020); (16) Morley et al. (2017) and (17) Lewis et al. (2013).

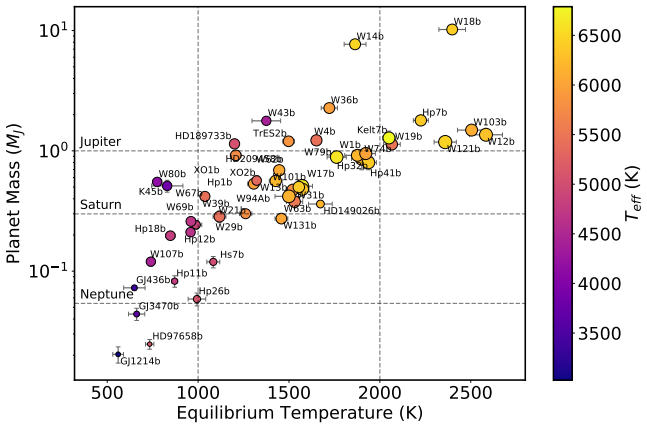


Fig. 1. Planet mass (M_{jup}) versus equilibrium temperature in Kelvin (assuming zero albedo and full redistribution) for all the planets presented in the current survey. The color of the points shows the stellar temperature (T_{eff}) in Kelvin and the size of the points is proportionate to the planetary radius. The gray dashed horizontal lines mark the masses of Jupiter, Saturn, and Neptune. The gray dashed vertical lines mark the temperature regions discussed in Sect. 4.1.5.

from the headers of each fits file. Our custom pipeline then corrects transient bad pixels in the image time series by comparing each pixel intensity to a median of the 30 preceding and 30 following frames. We replace the pixel intensity with the median value if it is $\geq 4\sigma$ from this value. The fraction of transient bad pixels that are corrected is displayed in Table A.4; this varies around 0.5 and 0.06% for channel 1 and channel 2, respectively. Our pipeline also consists of several different functions for three important steps in the data reduction: background sky subtraction, finding the centroid of the object, and performing aperture photometry. Additionally, in between these steps, a sliding σclipping on any outliers is performed on the centroiding and on the resulting photometry.

Previous studies have demonstrated that the data reduction method chosen to produce the light curves can have significant effects on the resulting measured transit depths (Ingalls et al. 2016). We therefore optimized the background subtraction, centroiding, and aperture photometry methods by running the pipeline over a 3D grid of different methods for each step; we call these methods the pipeline parameters. We tested three methods of background subtraction:

1. The "Box" method: median value from a 2×2 or 4×4 pixel box in all four corners of the frame.
2. The "Annulus" method: the mean of an annulus centred on the star of radii 6 or 8 pixels and size 2 or 4 pixels (using photutils).
3. The "Histogram" method: fit a Gaussian to a histogram of all the pixels in the frame, excluding the star.

We also tested three methods of centroiding:

1. The "Barycenter" method: center of light of a 3×3, 5×5 or 7×7 pixel box centered on the approximate position of the star.
2. The "Gaussian" method: fit a 2D Gaussian function to the entire image using Astropy (Astropy Collaboration 2018). All of the parameters of the 2D Gaussian were let free $(A, x_0, y_0, \sigma_x, \sigma_y, \theta)$ for each frame. The centroid position was the x_0, y_0 from the Levenberg Marquardt least squares fit (Agol et al. 2010).
3. The "Moffat" method: same as above but instead a 2D Moffat function was fit to the entire image.

Finally, we varied the aperture radius from 2.5 to 5.0 pixels in increments of 0.25 pixels. For each instance of the grid and therefore each iteration of the data-reduction pipeline, we performed a least-squares fit to our model (transit + systematic) and

calculated the reduced χ^2. The parameters yielding the lowest reduced χ^2 were used to create the light curve used for further analysis. There are a few exceptions to this. For example, some of the cooler planets have a lower S/N meaning the systematic errors dominate and there is therefore a larger scatter in the measured parameters at each pipeline iteration. These planets were examined manually and pipeline parameters were chosen by looking for both repeatable measurements and those with close to the minimum reduced χ^2. The optimum pipeline parameters including centroiding method, aperture size, background subtraction method, and data reduction information for each planet are detailed in Table A.3. Although the observations were made in "peak-up" mode, it is common that there is still some persistence at the beginning of the light curves. To correct for this, we devised a similar χ^2 test for cutting out the ramp at the beginning of the observations. We performed a series of cuts at the beginning of the light curve and refitted the model. Similarly, we chose the time at which we trim off the beginning of the light curve as the one that gave the lowest reduced χ^2 and root mean square (RMS) of the residuals.

Prior to any further data analysis, the light-curve intensities are converted to electron counts following the method described in the *Spitzer* handbook (multiply by EXPTIME* GAIN/FLUXCONV). This allows us to calculate the photometric errors using Poisson statistics.

3.1.2. Instrumental systematic modeling

Spitzer light curves exhibit significant amounts of correlated noise, which has been extensively studied and documented in the literature (Charbonneau et al. 2005; Agol et al. 2010; Seager & Deming 2010; Stevenson et al. 2010a). The dominant source of this red noise at 3.6 and 4.5 μm is caused by an intrapixel sensitivity. Variations in the telescope pointing combined with undersampling of the stellar PSF results in variations in the centroiding with time of ∼10% of a pixel. When combined with the intrapixel sensitivity, this results in variations in the photometric light curve on the order of 1%, which is problematic because the atmospheric signal we are trying to extract is on the order of 0.01%. There have been many different methods developed for dealing with these systematic errors (e.g., Reach et al. 2005; Charbonneau et al. 2008; Ballard et al. 2010; Stevenson et al. 2012; Gibson et al. 2012; Morello et al. 2015; Deming et al. 2015). Ingalls et al. (2016) presented the results of a data challenge on synthetic and real eclipse data of XO-3b, in which several systematic correction methods were tested against each other. These latter authors found that BLISS (Stevenson et al. 2012), Pixel Level Decorrelation (PLD; Deming et al. 2015), and ICA techniques (Morello et al. 2015) were the most precise for correcting the systematic errors of data of similar quality to XO-3b. In particular, PLD achieved the highest accuracy to the synthetic input data (Deming et al. 2015). We therefore present the results of the PLD function for correcting our systematic errors and, for comparison, we also test the polynomial function presented in Knutson et al. (2008).

Pixel level decorrelation. Unlike most methods of systematic correction, PLD does not use the centroid position of the stellar PSF on the pixel as input (Deming et al. 2015). Alternatively, PLD relates the intensities of the individual pixels directly to the photometry in one numerical step, whereas the other methods used two numerical steps: first finding the centroid position of the star on the detector and then relating that to the measured photometry with a different numerical process. To bypass this secondary measurement, PLD assumes that the measured brightness of the star is a smooth function of position. One can perform a Taylor expansion of this continuous and differentiable function such that the flux of the star can be expressed as a linear sum of the individual pixel fluxes (described fully in Deming et al. 2015):

$$\Delta S^t = \sum_{i=1}^{N} c_i \hat{P}_i^t + DT(t) + ft + h, \quad (1)$$

where S^t is the flux measured over time and Δ represents the total fluctuations from all sources. $\hat{P}_i^t = \frac{P_i^t}{\Sigma_{i=1}^N P_i^t}$ represents the normalized flux from pixel i at time t. Here, i is an integer pixel number, where a 2D grid of pixels centered on the PSF is chosen, each pixel being indexed with a single number. The number of pixels included can be selected depending on the size of the PSF and the brightness of the star. In our survey, we uniformly take a 2D grid of 3×3 pixels containing the PSF of the star on the middle pixel. $DT(t)$ is the transit shape, and $ft + h$ is a temporal ramp which is a typical behavior seen in warm *Spitzer* light curves caused by the residual telescope pointing.

Polynomial. We also corrected the intrapixel variations using the polynomial function of the position presented in Knutson et al. (2008). $F_{\rm corr} = F(K_0 + K_1(x - x_0) + K_2(x - x_0)^2 + K_3(y - y_0) + K_4(y - y_0)^2)$, where x_0 and y_0 are the integer pixel numbers plus 0.5, such that the polynomial is a function of the distance from the center of the pixel, where it is understood to be the most sensitive (Stevenson et al. 2012). Similarly to the PLD, we opted to use a linear function of time to correct the ramp over the entire light curve.

3.1.3. Fitting light curves to obtain transit parameters

Transit model. The transit shape ($DT(t)$) was calculated using Batman (Kreidberg 2015). Batman produces a transit light curve with nine tunable parameters: time of inferior conjunction (days), orbital period (days), planet radius (in units of R_s), semi-major axis (in units of R_s), orbital inclination (deg), eccentricity, angle of periastron (deg), limb darkening model, and limb darkening coefficients.

We fixed the orbital period for all of our planets to the values from the literature (Table A.1). Several planets in our sample have reported values of the eccentricity and angle of periastron passage. As a test for these planets we ran a fit of both a circular and an eccentric orbit and found that the eccentricity did not affect the measured transit depth. We therefore fixed the eccentricity and angle of periastron to zero for the remainder of the analysis.

Limb darkening. Southworth (2008) demonstrated that the choice of limb darkening can affect the measured planetary radius. This is particularly important in the optical wavelengths where the limb-darkening effects are stronger, but we investigated the effects for each of our planets as a standard output of our pipeline. We started by using linear coefficients for the limb-darkening law, which were calculated using the 1D Atlas code from Sing (2010) for the 3.6 and 4.5 μm *Spitzer* channels. We translated the interpolation routine from IDL to Python and interpolated the linear limb-darkening values and their 1σ errors using the effective temperature, surface gravity, and metallicity of every star in our sample (Table A.1). We were then able to vary the limb-darkening coefficients within the uncertainties and confirm that the limb-darkening does not have significant impact

on the resulting measured transit depth at these wavelengths. For this reason, we fixed the limb darkening to the linear coefficients for the remainder of the analysis.

This leaves four tunable parameters: the time of inferior conjunction (t_0), planet radius (R_p/R_s), semi-major axis (a/R_s), and the orbital inclination (i). The fixing and varying of these parameters is discussed in Sect. 3.1.3.

Estimating uncertainties using MCMC. After determining the optimum pipeline parameters and the cutting time at the beginning and end of the light curve, we performed a full statistical analysis of the photometric transit light curves to estimate the uncertainties and study the co-variances of the parameters.

Before performing any fitting, we normalized the light curves, which allowed us to directly compare the PLD coefficients and the photon flux time-series. An initial normalization was done by taking the median of the first 100 data points in the light curve. We then performed an initial Levenberg-Marquardt least-squares fit to get the preliminary transit parameters, which were then used to cut out the transit, and we recalculated the normalisation scale such that the median of the out-of-transit flux was 1.

Following a second least-squares fit, we performed a 4σ clip of the residuals to remove any outlying photometric points not captured in the centroiding clipping. We performed a final least-squares fit on the normalized σ clipped data to determine the initial guess for the parameters as an input for our Markov chain Monte Carlo (MCMC) analysis. We first calculated the errors on the photometric points using Poisson statistics assuming photon noise ($\sqrt{N}$). Then, after the first initial least-squares fit, we determined how close we were to the photon noise for each fit and scaled up the uncertainties. The results are shown in Table A.4. As is commonly found for *Spitzer* time-series transit observations, our uncertainties are around 20–50% above the photon noise limit for the whole survey. Scaling up the uncertainties on the photometric points by this factor before running the final fit results in a reduced χ^2 of ∼1, which prevents us from underestimating the uncertainties on the physical transit parameters.

We estimated the uncertainties on the best-fit parameters using emcee, the open-source Affine-Invariant Metropolis-Hastings algorithm for MCMC analysis developed by Foreman-Mackey et al. (2013). We initialized the MCMC chains with 100 walkers, 1000 burn-in steps, and 2000 production steps. We also performed a prayer-bead analysis of the uncertainties as a sanity check, but here we adopt the results from the MCMC analysis because the sampling can be much larger. For each MCMC run, we checked for convergence with the emcee recommended acceptance fraction (0.2–0.5) and the Gelmin-Rubin statistic (≤1.1) (Gelman & Rubin 1992). If the S/N of the data was low, sometimes the MCMC had an extremely low acceptance fraction. When this happened, we doubled the number of walkers until proper convergence was achieved. We derived the 1σ error bars asymmetrically as 34% above and below the median.

Our combined astrophysical and instrumental (PLD) noise model has 14 free parameters in total for the first fit. We treated the two distinct groups of planets slightly differently in our data reduction. The planets were split into two groups, lower S/N planets (generally cooler with longer periods) and higher S/N planets (short-period hot Jupiters). For the higher S/N planets, we let t_0, R_p/R_s, a/R_s, and i free in the initial fit with uniform priors on all parameters. We then performed a second MCMC fit where we used a 1σ Gaussian prior on a/R_s and i based on the results from the first fit. For the lower S/N planets, where it is difficult to detect the transit in each individual light curve, we need to fix a/R_s and i to the literature values for the fitting. For both of these methods, the walkers are initialized in a tight cluster around the best-fit Levenberg-Marquardt minimization. These lower S/N planets also had multiple transits in each band-pass; each of these was analyzed, and the average transit depth was calculated using the weighted sum, where the weight is the inverse variance multiplied by an "over dispersion" factor as done in Ingalls et al. (2016). The over dispersion factor allows for underestimation of the individual uncertainties; see Lyons (1992) for further information.

Special cases. The systematic errors caused by the intra-pixel variability of the IRAC detectors on one of the WASP-13b light curves were not properly captured by our pipeline, such that a bump at the end of the transit remained in the reduced light curve at 3.6 µm. This had the consequence of making our fitted transit depth shallower than it should be. We therefore removed these data from our fit and ran the pipeline again to get the optimal parameters and transit depths. In total, we removed 36 minutes from the last quarter of the in-transit flux, but the egress remained intact allowing us to still characterize the system.

Similarly, the 3.6 µm transit of WASP-131b showed a bump in the baseline before transit, likely a starspot occultation. Therefore, we also removed 50 min of flux in our MCMC fit.

Furthermore, our approach was slightly modified for HAT-P-26b due to its low S/N, and so we set Gaussian priors on the semi-major axis and inclination in the initial fits based on the literature values.

3.2. Interpreting transmission spectrophotometry with 1D atmospheric modeling

To interpret the results from our survey of transiting hot Jupiters, we compare the IRAC transit depths with a grid of simulated atmospheric spectra. First, double-gray analytical formulae are applied to construct the cloud-free temperature–pressure (T–P) profiles for a wide range of stellar irradiation Heng et al. (2014). Second, we use a photochemical kinetics model (VULCAN, Tsai et al. 2017 see Sect. 3.2.3) to compute the composition under the effects of photo-dissociation and vertical mixing. The T–P profiles and the chemical composition are not self-consistently computed; here, we focus on how the stellar flux impacts the disequilibrium chemistry. Last, a radiative transfer code (PLATON Zhang et al. 2019, see Sect. 3.2.4) is used to create transmission spectra to compare with the observational data. Our fiducial model grid spans a range of equilibrium temperatures (T_{eq}) from around 400 K to around 2400 K in ∼100 K steps, planetary surface gravities (g_p) 500, 1500, 5000 cm s^{-2}, planet radius (R_p) 0.5, 1, 1.5, and 2 R_{jup} and stellar radius (R_s) 0.5, 1, 1.5, and 2 $R_\odot$ with 1x solar composition and equilibrium chemistry (no vertical mixing, no photo-chemistry, no boundary fluxes). We then expand our modeling in two dimensions. First, we incorporate nonequilibrium processes and capture vertical mixing in the form of an eddy diffusion coefficient (K_{zz}). Second, we test the effects of higher metallicity by creating the full set of grids with 30x solar metallicity. We describe the creation of these grids in full detail below.

3.2.1. Stellar irradiation and T–P profiles

In our survey, most hot Jupiters populate a small range of close-in orbits, a_{mean} = 0.037 ± 0.013 AU, while the parent stars span

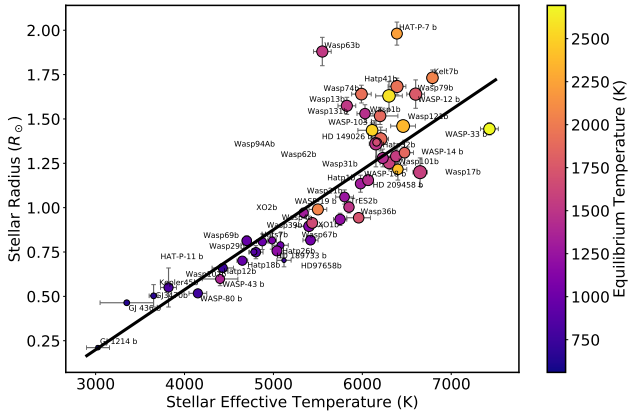


Fig. 2. Stellar radius as a function of stellar effective temperature. The black line shows the first-order polynomial best fit used for creation of the T-P grid (see Sect. 3.2.1). The color of the points shows the equilibrium temperature of the planets, and the size of the points is scaled to the planet radius.

several spectral types, from early M stars to F stars. In reality, the stellar temperature varies from about 3000 to 7000 K, while the radius also increases with earlier stellar types. For a planet at orbital distance (a) around a star with radius (R_s) and effective temperature ($T_{\rm eff}$), the equilibrium temperature of the planet ($T_{\rm eq}$) is proportional to $T_{\rm eff}(R_s/a)^{1/2}$. Therefore, changes in the stellar flux play a bigger role than changes in the orbital distance or the stellar radius when determining the irradiation the planet received and its effective temperature. In this regard, we assume a fixed orbital distance for our model grid to isolate the effects of stellar irradiation. The mean value of the samples, 0.035 AU, is taken across the grid. In this setting, the effective temperature of the model planet is entirely determined by the stellar luminosity, and not by the orbital distance. We also note that the intrinsic temperature ($T_{\rm int}$) is negligible and thus the effective temperature ($T^4_{\rm eff} = T^4_{\rm eq} + T^4_{\rm int}$) is the same as the equilibrium temperature. Additionally, our assumed value of $T_{\rm int} = 150$ K has little effect on our model temperature pressure profiles of the hot Jupiters.

The next step is to determine the size and therefore the energy flux of the stars. For main-sequence stars, which follow the mass–luminosity and mass–radius relations, we fit a power-law relation between the radius and effective temperature; see Fig. 2. The power-law fitting to our sample yields the following expression for the stellar radius: $R_S = m * T_{\rm eff} + b$ where m and b are 0.0003381 and −0.81495, respectively. Once the effective temperature and the radius of the star are known, there is enough information to specify the incident irradiation of the model atmospheres.

We then compute the T–P profiles for the given stellar irradiation using the analytical double-gray radiative equilibrium solutions in Heng et al. (2014, Eq. (126)).

The parameters used in this calculation are chosen to match the numerical radiative transfer results listed in Table 3. Similar to the prescriptions in Guillot (2010) and Parmentier & Guillot (2014), the opacities do not have a pressure dependence. We reiterate that this relation allows us to uniquely express the equilibrium temperature of a planet at a given orbital distance as a function of stellar temperature. Our stellar grid, with effective temperatures from 3250 to 7000 K, produces irradiated atmospheres of temperature from 446 to 2248 K at 0.035 AU. To reach the temperatures of the ultra-hot Jupiters we also run additional models with an orbital distance at 0.02 AU. The resulting temperature pressure profiles are shown in Fig. 3.

Table 3. Fixed parameters used in the double-gray radiative equilibrium solution for creating TP profiles.

$T_{\rm irr}$	$T_{\rm int}$	$\kappa_{\rm L}$	$\kappa_{\rm S}$	$\beta_{\rm L}$	$\beta_{\rm S}$
631	150	0.02	0.00035	1	1
775	150	0.02	0.00068	1	1
919	150	0.02	0.001	1	1
1069	150	0.02	0.0014	1	1
1222	150	0.02	0.0017	1	1
1379	150	0.02	0.0019	1	1
1540	150	0.02	0.0022	1	1
1706	150	0.02	0.0035	1	1
1875	150	0.02	0.0038	1	1
2049	150	0.02	0.004	1	1
2227	150	0.02	0.0043	1	1
2410	150	0.02	0.006	1	1
2595	150	0.02	0.006	1	1
2786	150	0.02	0.006	1	1
2980	150	0.02	0.0061	1	1
3179	150	0.02	0.0062	1	1

Notes. For each TP profile we show the fixed irradiation temperature ($T_{\rm irr}$), intrinsic temperature ($T_{\rm int}$), longwave opacity ($\kappa_{\rm L}$), shortwave opacity ($\kappa_{\rm S}$), longwave scattering parameter ($\beta_{\rm L}$), and the shortwave scattering parameter ($\beta_{\rm S}$).

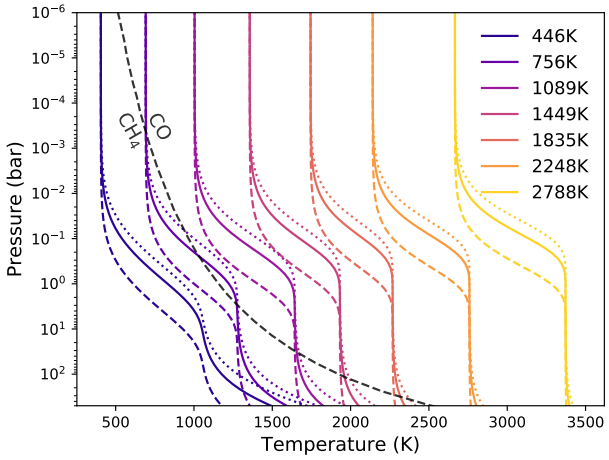


Fig. 3. Analytical TP profiles for a grid of models spanning equilibrium temperatures ∼400–2800 K, showing every ∼400 K. For each temperature, we show three profiles where the surface gravity is varied: dotted, solid, and dashed lines represent 500, 1000, and 5000 cm s^{-2} respectively. Grey dashed line represents the gas transition between CH_4- and CO-dominated atmospheres when chemical equilibrium is assumed.

The simple prescription allows us to explore the parameter space in a basic way and to focus on the correlation with stellar irradiation. Although the intrinsic temperature is held constant in our T–P profiles, the realistic interior can be potentially hotter. Tremblin et al. (2017) and Sainsbury-Martinez et al. (2019) showed that circulation can transport entropy downward and leads to a hotter deep interior over time. Thorngren et al. (2019) suggested much higher $T_{\rm int}$ for observed hot Jupiters (with $T_{\rm eq} \gtrsim 1300$ K) than the 100 K commonly assumed in GCMs. Fortney et al. (2020) also investigated the effects of heating from tidal dissipation for warm Jupiters (with $T_{\rm eq} \gtrsim 1300$ K) with simplified chemical timescale analysis. The upshot of the hotter interior is that it lowers the quenched [CH_4]/[CO] ratio. In short, a hot deep interior changes the expectation for equilibrium chemistry

in deep layers, hence the expectation for disequilibrium chemistry higher up. As the equilibrium abundance of CH_4 generally increases with depth (at least in our solar and 30x solar models), lowering vertical mixing also results in a lower [CH_4]/[CO] ratio and can effectively be degenerate with a hotter interior. However, we find high vertical mixing matches the hot Jupiters better, even with the lower T_{int} of 150 K. Increasing the interior temperature will reduce CH_4, so even higher vertical mixing would be required to recover the same CH_4 abundance for these planets. As for the cooler planets, the signature leading to our inference of low vertical mixing can also be explained by a hot interior if there is actually no CH_4 in the deep hot atmosphere. However, the sources of internal heating and their exact interior temperature for these cool planets are rather uncertain (see Fortney et al. 2020 for a detailed discussion).

In addition to this, our prescription for PT profiles is simplified compared to 1D radiative and convective models. Nevertheless, in this study, we are interested in the relative difference between two broad bandpasses (3.6 and 4.5 μm), and therefore the prescription used for the TP profiles is less critical than for absolute measurements. The relative difference between 3.6 and 4.5 μm is globally similar for our prescription as compared to the 1D RC models. We acknowledge that the vertical mixing is likely to be affected by the choice of TPs, but testing this difference is beyond the scope of our current study.

Our simple model emphasizes the importance of the degeneracies between vertical mixing, interior temperature, and equilibrium chemistry, but also limits the possible interpretations. A more detailed approach than the simple model we used is required to study the impact of the various processes on the observations with greater accuracy. However, such a detailed study will also be limited by the unknown interior temperature. Therefore, we limit ourselves to a simple approach as a sophisticated analysis with more advanced temperature pressure profiles is beyond the scope of this paper.

3.2.2. Grid of stellar spectra

As the effective temperature of the star rises, the spectral energy distribution shifts to shorter wavelengths. We therefore adopted the stellar spectral grid from Rugheimer et al. (2013), which ranges from 4250 to 7000 K and covers F0 to K7 spectral types. The models start with the synthetic ATLAS spectra (Kurucz 1979) and then we co-add the observed spectra from International Ultraviolet Explorer for UV (<= 300 nm); see Rugheimer et al. (2013) for the detailed stellar grid setup. Additionally, for late K and M stars (T_{eff} < 4250 K), we picked GJ 436 (T_{eff} = 3350 K) as our fiducial star. The high-resolution spectrum of GJ436 is taken from the MUSCLES survey (France et al. 2016)[1] and scaled for the stellar fluxes with effective temperatures of 3250, 3500, 3750, and 4000 K.

3.2.3. Modeling the photo-chemical kinetics with VULCAN

We explore the effects of photolysis, atmospheric mixing, and metallicity by using a photochemical kinetics model, VULCAN (Tsai et al. 2017)[2]. The code solves the steady-state chemical compositions for a given temperature-pressure profile and has been benchmarked for hot Jupiters. In this work, we use the updated version that includes nitrogen chemistry and photochemistry (Tsai et al., in prep.). The chemical model with updated nitrogen chemistry and photochemistry has been tested on nitrogen-dominated atmospheres for super-Earths (Zilinskas et al. 2020). The N-C-H-O network consists of about 600 thermal reactions (including forward and reverse) and 40 photodissociation reactions. We validate our updated model against the one-dimensional photochemical and thermochemical kinetics and diffusion model presented by Moses et al. (2011) for HD 209458b, see Fig. B.1.

Vertical mixing is simulated through means of an eddy diffusion co-efficient (K_{zz}), which assumes that atmospheric motion resembles diffusion when convection and turbulence occur on much smaller scales than the magnitude of the pressure scale height. We vary the eddy diffusion coefficient to explore various strengths of vertical mixing, with constant values of 10^8, 10^{10}, and 10^{12} cm^2 s^{-1}. The choice of the values is consistent with those extracted from GCM simulations (Moses et al. 2011; Parmentier et al. 2013; Zhang & Showman 2018; Komacek et al. 2019). Furthermore, the elemental abundance of the atmosphere is assigned to two different metallicities: 1x solar and 30x solar (Lodders et al. 2009).

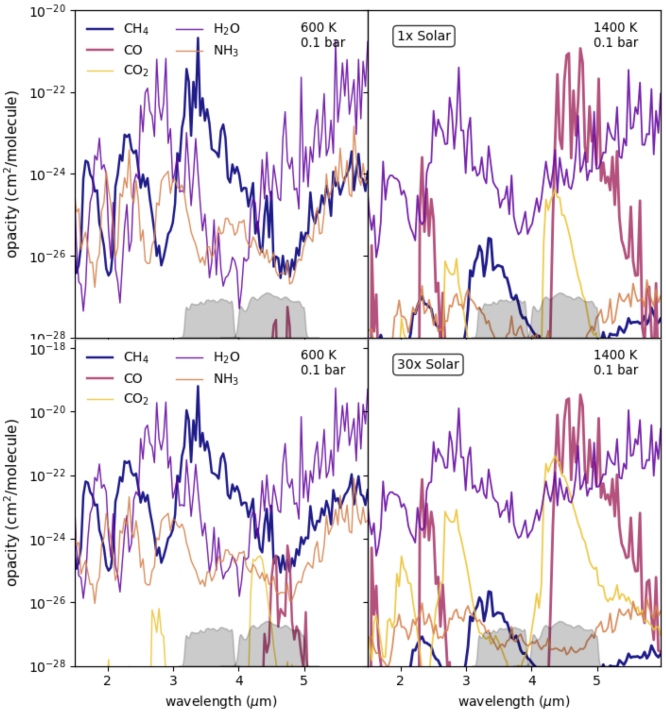


Fig. 4. Opacities for a chemical equilibrium atmosphere at 600 K (*left*) and 1400 K (*right*) at 0.1 bar. *Top panels*: abundance-weighted opacities for a solar composition atmosphere. *Bottom panels*: abundance-weighted opacities for a 30x solar composition atmosphere. Carbon monoxide, water, methane, and carbon dioxide (for 30x solar) are the dominant absorbing species at the two IRAC channels (3.6 and 4.5 μm).

3.2.4. Creating the transmission spectra with PLATON

Finally, transmission spectra are then simulated using the open-source, transit-depth calculator and retrieval tool, PLATON (Zhang et al. 2019)[3]. The code has been modified to take nonequilibrium compositions from our calculation, including CH_4, CO, CO_2, C_2H_2, H_2O, O_2, OH, C_2H_4, C_2H_6, H_2CO, HCN, NH_3, and NO. The main opacities relevant for the wavelengths of *Spitzer*/IRAC are displayed in Fig. 4. We assume chemical equilibrium for the rest of the species in PLATON. The details of the

[1] http://cos.colorado.edu/~kevinf/muscles.html
[2] https://github.com/exoclime/VULCAN
[3] https://platon.readthedocs.io/en/latest/intro.html

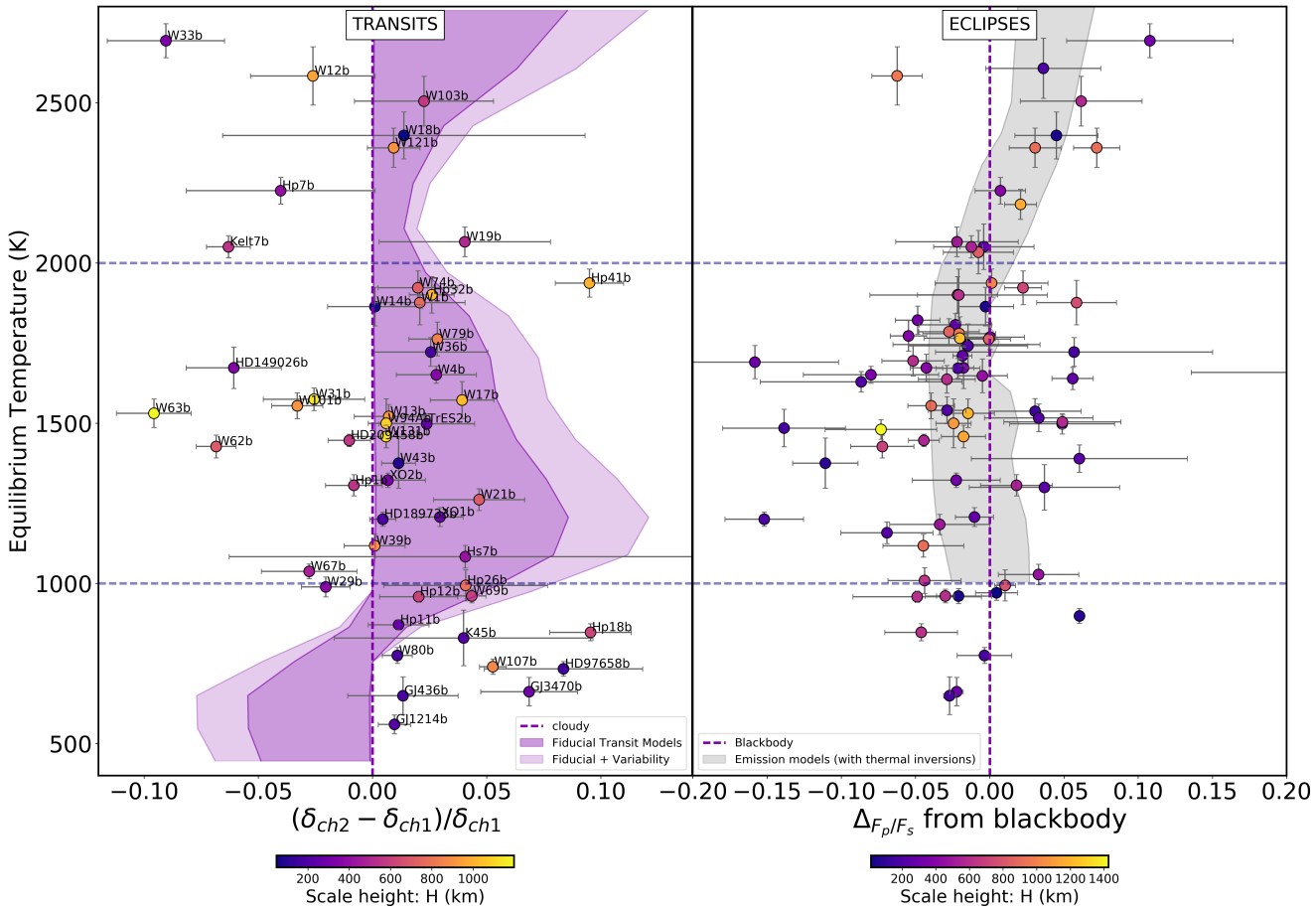


Fig. 5. *Left panel*: difference in transit depths between 4.5 and 3.6 μm normalized to the transit depth at 3.6 μm plotted against equilibrium temperature. The 1σuncertainties are shown in gray, and the color bar depicts the scale height in km. The shaded area on the *left panel* shows our grid of solar composition cloud-free equilibrium chemistry models; the extended lighter region is corrected for stellar variability. The dashed purple vertical line at zero is where planets with low-pressure gray clouds would lie. *Right panel*: deviation from the black body in emission against the equilibrium temperature, presented in Baxter et al. (2020). The color scale shows the scale height in km and the shaded region shows the grid of models containing temperature inversions.

forward model can be found in Zhang et al. (2019). We neglect stellar limb darkening in these models and the synthetic transit depth is expressed as $(R_p/R_s)^2$.

3.2.5. Calculating the model *Spitzer*/IRAC transit depths

We integrate the simulated transmission spectra with *Spitzer*/IRAC spectral response functions and weight with the stellar flux using the following equation:

$$\overline{\delta}_\lambda = \frac{\int_0^\infty \delta(\lambda)\lambda R(\lambda)F_s(\lambda)\mathrm{d}\lambda}{\int_0^\infty \lambda R(\lambda)F_s(\lambda)\mathrm{d}\lambda}, \quad (2)$$

where $R(\lambda)$ is the spectral response function at either 3.6 or 4.5 μm [e-/photon] (Quijada et al. 2004) and $\delta(\lambda)$ is the transmission spectrum from PLATON and $F_s(\lambda)$ is the stellar flux. The output, $\overline{\delta}_\lambda$, is the weighted average transit depth that would be observed with *Spitzer*/IRAC in either of the two bandpasses.

Figure 5 shows the interpolated grid of fiducial models (solar composition, cloud-free with equilibrium chemistry). Here, we plot the normalized IRAC transit depth difference against the equilibrium temperature, and overplot the results from our transit survey. Figure 6 shows the different tracks of the model grid that make up the shaded regions and Fig. 7 shows the different vertical mixing and metallicity interpolated grids with the data. For the cloudy grid, we simply assume a gray cloud opacity such that the spectra are flat and thus the transit depth difference would be zero, which is shown as a vertical line on Figs. 5 and 7.

4. Results

4.1. Measured transit depths and their ratios

4.1.1. Results of measured transit depths

Table 4 summarizes the results of the MCMC analysis of the light curves, and lists the final values and uncertainties for the transit depths, mid transit times, and impact parameters from the final fits as well as the inclination and semi-major axis obtained from the first fits. We checked that the initial fits of the semi-major axis and the inclination are in agreement with the literature values before fixing them with Gaussian priors for the second fit. The survey as a whole was in statistical agreement with the literature values within <1σ.

We also show the raw photometry with the best-fit model for each visit in Appendix A, and we show the corresponding plots of RMS versus bin size in Appendix A. Figure A.1 shows the reduced, normalized, and systematic corrected transit light curves for all planets in our sample for both channel 1 and channel 2 with the best-fit model resulting from the MCMC. We

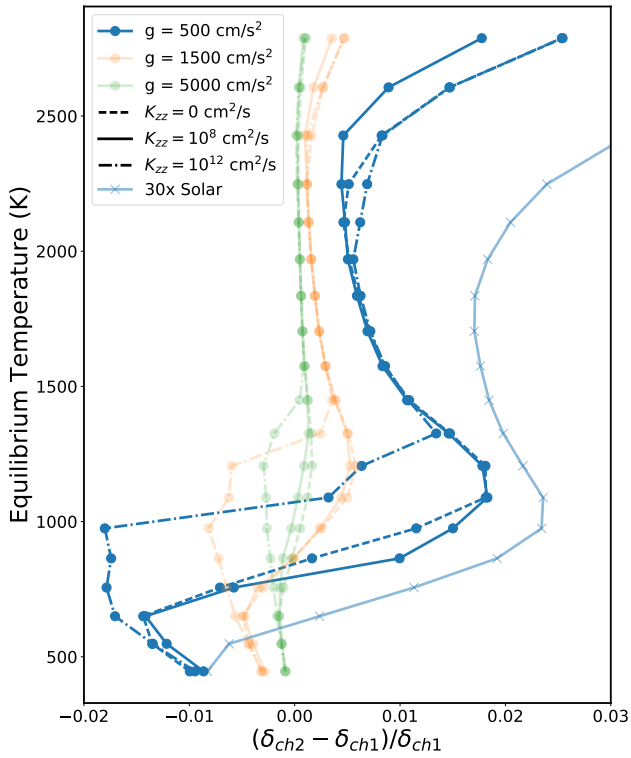


Fig. 6. Normalized *Spitzer* transit depth difference as a function of the equilibrium temperature for a selection of the grid tracks created with our atmospheric model framework described in Sects. 3.2.3 and 3.2.4. We show a selection of grids with 1x solar composition and $R_p = 2R_J$. Different colors show different surface gravities: blue is g = 500 cm s^{-2}, orange is g = 1500 cm s^{-2}, and green is g = 5000 cm s^{-2}. Different line styles show the effect of vertical mixing: solid line shows equilibrium chemistry, dashed is K_{zz} = 10^8 cm^2 s^{-1}, and dot-dashed is K_{zz} = 10^{12} cm^2 s^{-1}. The lighter blue line with '×' markers shows a 30x solar track with $R_p = 2R_J$, g = 500 cm s^{-2}, and K_{zz} = 0 cm^2 s^{-1}.

calculate the residuals, the χ^2, and the RMS of the residuals as sanity checks for each light curve (Table A.4).

As mentioned in Sect. 3.1.3, before performing a complete MCMC analysis, we first check the fraction above photon noise and scale up the errors accordingly. Figure 8 displays a histogram of the fraction above photon noise for all analyzed light curves. The histograms have a median of 1.36 and 1.27 times photon noise for 3.6 and 4.5 μm respectively, which is typical for what has been achieved with *Spitzer* in the past (Ingalls et al. 2016).

4.1.2. Comparison to literature

Several of the planets from our survey have had their *Spitzer* light curves previously analyzed (e.g., Sing et al. 2016; Garhart et al. 2020). We compare our results with those from Sing et al. (2016) and Garhart et al. (2020). Our measured transits are consistent within 3σ with those from the literature apart from a couple of outliers described below. Two of the largest outliers are the channel 2 transit depth of KELT-7b and the channel 1 transit depth of WASP-62b, both analyzed in Garhart et al. (2020) with PLD. We interpret the differences as due to the brightness of the host stars, and more specifically as due to the number of pixels selected for the pixel level decorrelation. These stars are bright and therefore 12 pixels are selected to model the systematic errors in Garhart et al. (2020) whereas we use 9 pixels uniformly for the entire survey (e.g., see Fig. A.3). We emphasize that these differences do not affect the general conclusion of the paper.

4.1.3. Transit depth ratio

We combine our results with transit measurements from the literature, which results in a survey of transit depths at 3.6 and 4.5 μm for 49 planets spanning a large range of equilibrium temperatures. We now compare all targets in our survey in a statistical manner. To do this, we opt to use a metric that is as free as possible from any assumptions: the normalized difference of the transit depths:

$$\bar{\Delta}_{tr} = \frac{(\delta_{ch2} - \delta_{ch1})}{\delta_{ch1}}. \quad (3)$$

With this calculation, we tested for correlations with a number of other parameters: stellar parameters (T_{eff}, log g, Fe/H, R_s), orbital parameters (semi-major axis (AU), eccentricity, inclination), and planetary parameters (T_{eq}, log g, R_p, M_p, scale height). We looked for correlations between these parameters using two statistical methods. First, we calculated the Pearson correlation coefficient (r) and its associated chance probability (p). We then fit a straight line using an orthogonal distance regression (ODR) to account for the errors on both the abscissa and ordinate values as in Boggs et al. (1989); we note the resulting residual variance of the fits.

4.1.4. Searching for trends in the difference of transit depths

We analyze our *Spitzer* survey by looking at the normalized difference in the transit depths. Our normalized transit depth difference metric confers the advantage that it does not include any additional assumptions on the composition of the atmosphere. Several studies look at the number of scale heights crossed at different wavelengths, including the strength of the water feature in the HST/ WFC3 bandpass (e.g., Sing et al. 2016). Including the scale height requires an assumption on the mean molecular weight, which includes errors from the surface gravity and equilibrium temperature. Furthermore, our metric is also independent of the stellar radius, unlike the difference in transit depths ($\delta_{ch2} - \delta_{ch1}$). Ultimately, this metric is a proxy for the ratio of the optical depths at these two wavelengths. We expect that the strength and magnitude of this metric can be used to test how the dominant expected atmospheric opacities change with the equilibrium temperature of the planets; see Sect. 5.1.

We search for any correlations that could be present between the calculated normalized transit depth difference and the physical parameters of the planetary systems that we are exploring. Table 5 summarizes the correlations for each of the parameters. The three parameters with the strongest Pearson correlation coefficients and the lowest chance probabilities are T_{eq}, T_{eff}, and R_s. Both T_{eff} and R_s are incidentally included in the calculation of the equilibrium temperature, T_{eq} (in our case with zero albedo and full redistribution). We also observe that the weakest correlations are with the planetary mass, planetary radius, and semi-major axis. This is not surprising because our sample is highly biased towards hot Jupiters with a relatively small range of radii and masses, and with similarly close-in orbits. This means that the span of these parameters is small and therefore the uncertainties will be large and the correlations will not be obvious.

4.1.5. Transit depth versus equilibrium temperature

In Fig. 5 (left panel), we plot the normalized transit depth difference ($(\delta_{ch2} - \delta_{ch1})/\delta_{ch1}$) against the equilibrium temperature for all planets in our sample. This plot contains 49 planets with masses 0.02–10.2 M_{jup}, radii 0.24–1.9 R_{jup}, and equilibrium temperatures 550–2690 K. The color scale on the data points shows

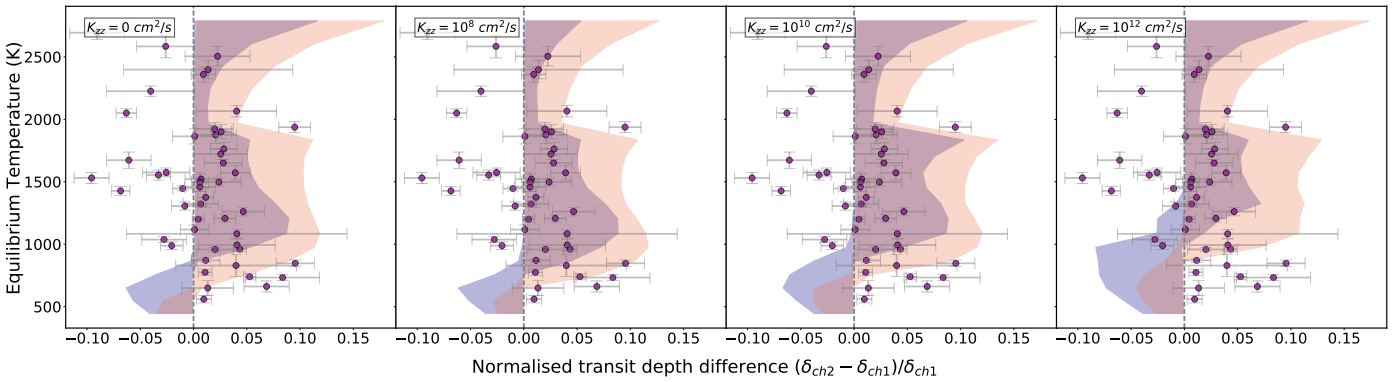


Fig. 7. Normalized *Spitzer* transit depth difference as a function of the equilibrium temperature for the complete grids of transmission models created with our atmospheric model framework described in Sects. 3.2.3 and 3.2.4. At each temperature, we show the models where the surface gravity is representative of our survey; i.e., at $T_{eq} > 1800$ K we only plot $g = 1500$ and 5000 cm s^{-2}. Panels *from left to right* show equilibrium chemistry (no vertical mixing), $K_{zz} = 10^8$, $K_{zz} = 10^{10}$ and $K_{zz} = 10^{12}$ cm^2 s^{-1}. The blue translucent shaded region shows the 1x solar composition and orange translucent shaded region shows the 30x solar composition (overlap in purple). Gray dashed line represents a gray opacity source showing no spectral features. Planets from our sample are overplotted in purple circles with their 1σ error bars.

Table 4. Results from the MCMC analysis.

Planet	λ (μm)	a/R^*	inc degrees	depth $(R_p/R_s)^2$ (%)	b	T0 BJD_UTC
HAT-P-32 *b*	3.6	$6.13^{+0.02}_{-0.02}$	$89.5^{+0.3}_{-0.5}$	$2.15^{+0.01}_{-0.01}$	$0.05^{+2.06}_{-2.90}$	$24\,56\,250.103520^{+0.000112}_{-0.000120}$
HAT-P-32 b	4.5	$6.13^{+0.02}_{-0.04}$	$89.4^{+0.4}_{-0.6}$	$2.21^{+0.02}_{-0.02}$	$0.06^{+2.62}_{-3.95}$	$24\,56\,370.504208^{+0.000154}_{-0.000152}$
XO-1 b	3.6	$11.46^{+0.05}_{-0.11}$	$89.5^{+0.3}_{-0.4}$	$1.67^{+0.01}_{-0.01}$	$0.09^{+3.56}_{-4.43}$	$24\,56\,426.076095^{+0.000115}_{-0.000120}$
XO-1 b	4.5	$11.24^{+0.20}_{-0.23}$	$88.8^{+0.5}_{-0.4}$	$1.72^{+0.01}_{-0.01}$	$0.24^{+5.40}_{-4.49}$	$24\,56\,437.900819^{+0.000158}_{-0.000157}$
HAT-P-1 b	3.6	$9.91^{+0.13}_{-0.13}$	$85.7^{+0.1}_{-0.1}$	$1.40^{+0.01}_{-0.01}$	$0.74^{+0.99}_{-0.99}$	$24\,56\,547.478364^{+0.000156}_{-0.000150}$
HAT-P-1 b	4.5	$10.07^{+0.16}_{-0.15}$	$85.8^{+0.1}_{-0.1}$	$1.39^{+0.01}_{-0.01}$	$0.73^{+1.25}_{-1.17}$	$24\,56\,556.409109^{+0.000187}_{-0.000190}$
WASP-17 b	3.6	$7.16^{+0.14}_{-0.16}$	$88.1^{+0.8}_{-0.7}$	$1.52^{+0.01}_{-0.01}$	$0.24^{+6.05}_{-4.97}$	$24\,56\,423.188874^{+0.000233}_{-0.000221}$
WASP-17 b	4.5	$7.24^{+0.09}_{-0.15}$	$88.6^{+0.8}_{-0.8}$	$1.57^{+0.02}_{-0.02}$	$0.17^{+6.13}_{-5.89}$	$24\,56\,426.923243^{+0.000288}_{-0.000285}$
WASP-39 b	3.6	$10.47^{+0.19}_{-0.17}$	$87.0^{+0.2}_{-0.2}$	$2.15^{+0.02}_{-0.02}$	$0.56^{+1.83}_{-1.68}$	$24\,56\,401.396438^{+0.000159}_{-0.000176}$
WASP-39 b	4.5	$11.38^{+0.28}_{-0.25}$	$87.7^{+0.3}_{-0.2}$	$2.16^{+0.02}_{-0.02}$	$0.45^{+3.14}_{-2.66}$	$24\,56\,575.774315^{+0.000200}_{-0.000194}$
HAT-P-12 b	3.6	$11.23^{+0.26}_{-0.26}$	$88.0^{+0.3}_{-0.3}$	$1.89^{+0.01}_{-0.01}$	$0.39^{+3.64}_{-3.30}$	$24\,56\,359.882148^{+0.000131}_{-0.000138}$
HAT-P-12 b	4.5	$10.90^{+0.35}_{-0.30}$	$87.8^{+0.4}_{-0.3}$	$1.93^{+0.03}_{-0.03}$	$0.41^{+4.47}_{-3.60}$	$24\,56\,363.095398^{+0.000197}_{-0.000187}$
HAT-P-18 b	3.6	$15.28^{+0.47}_{-0.41}$	$88.5^{+0.3}_{-0.3}$	$1.77^{+0.02}_{-0.02}$	$0.41^{+5.19}_{-4.07}$	$24\,56\,461.067141^{+0.000195}_{-0.000197}$
HAT-P-18 b	4.5	$15.48^{+0.45}_{-0.44}$	$88.5^{+0.3}_{-0.3}$	$1.93^{+0.02}_{-0.02}$	$0.41^{+5.07}_{-4.47}$	$24\,56\,483.099518^{+0.000215}_{-0.000215}$
TrES-2 b	3.6	$7.96^{+0.16}_{-0.15}$	$83.9^{+0.2}_{-0.2}$	$1.37^{+0.02}_{-0.02}$	$0.84^{+1.33}_{-1.34}$	$24\,56\,252.834601^{+0.000203}_{-0.000196}$
TrES-2 b	4.5	$8.20^{+0.25}_{-0.23}$	$84.2^{+0.3}_{-0.2}$	$1.40^{+0.02}_{-0.02}$	$0.83^{+2.09}_{-1.92}$	$24\,56\,257.775215^{+0.000268}_{-0.000267}$
WASP-4 b	3.6	$5.58^{+0.03}_{-0.04}$	$89.3^{+0.5}_{-0.7}$	$2.28^{+0.02}_{-0.02}$	$0.07^{+2.71}_{-4.14}$	$24\,56\,288.955465^{+0.000137}_{-0.000142}$
WASP-4 b	4.5	$5.46^{+0.05}_{-0.11}$	$88.7^{+0.9}_{-1.3}$	$2.34^{+0.03}_{-0.03}$	$0.12^{+4.80}_{-7.20}$	$24\,56\,292.969500^{+0.000208}_{-0.000212}$
XO-2 b	3.6	$8.17^{+0.09}_{-0.17}$	$88.9^{+0.7}_{-0.8}$	$1.07^{+0.01}_{-0.01}$	$0.15^{+5.81}_{-6.13}$	$24\,56\,295.370617^{+0.000139}_{-0.000140}$
XO-2 b	4.5	$7.77^{+0.22}_{-0.22}$	$87.6^{+0.7}_{-0.6}$	$1.07^{+0.01}_{-0.01}$	$0.33^{+5.43}_{-4.50}$	$24\,56\,292.754728^{+0.000198}_{-0.000191}$
GJ3470 b	3.6	$14.63^{+0.52}_{-0.50}$	$88.4^{+0.3}_{-0.3}$	$0.57^{+0.01}_{-0.01}$	$0.42^{+4.13}_{-3.73}$	$24\,56\,284.001794^{+0.000118}_{-0.000115}$
GJ3470 b	4.5	$14.41^{+0.65}_{-0.54}$	$88.4^{+0.4}_{-0.3}$	$0.61^{+0.01}_{-0.01}$	$0.41^{+5.23}_{-4.09}$	$24\,56\,294.011801^{+0.000151}_{-0.000150}$
WASP-21 b	3.6	$9.55^{+0.30}_{-0.28}$	$87.1^{+0.4}_{-0.4}$	$1.08^{+0.01}_{-0.01}$	$0.49^{+3.75}_{-3.34}$	$24\,56\,532.561048^{+0.000261}_{-0.000260}$
WASP-21 b	4.5	$9.61^{+0.40}_{-0.34}$	$87.1^{+0.5}_{-0.4}$	$1.14^{+0.02}_{-0.02}$	$0.48^{+5.28}_{-4.23}$	$24\,56\,536.882998^{+0.000308}_{-0.000322}$

Notes. We show the semi-major axis (a/R^*), the inclination (degrees), the percentage transit depth $(R_p/R_s)^2$, the corresponding impact parameter (b) and the mid-transit time in BJD_UTC. Values for the semi-major axis and the inclination are from the initial MCMC fits and then these are fixed with Gaussian priors for a second MCMC run where the final values for the transit depths are determined.

Table 4. continued.

Planet	λ (μm)	a/R^*	inc degrees	depth $(R_p/R_s)^2$ (%)	b	T0 BJD_UTC
WASP-31 b	3.6	$8.06^{+0.20}_{-0.18}$	$84.5^{+0.2}_{-0.2}$	$1.54^{+0.02}_{-0.02}$	$0.77^{+1.81}_{-1.66}$	$24\,56\,360.907660^{+0.000317}_{-0.000328}$
WASP-31 b	4.5	$8.86^{+0.34}_{-0.32}$	$85.2^{+0.3}_{-0.3}$	$1.50^{+0.03}_{-0.03}$	$0.74^{+2.86}_{-2.77}$	$24\,56\,371.125690^{+0.000407}_{-0.000412}$
WASP-1 b	3.6	$5.72^{+0.03}_{-0.05}$	$89.3^{+0.5}_{-0.8}$	$1.07^{+0.01}_{-0.01}$	$0.07^{+2.91}_{-4.60}$	$24\,56\,361.902274^{+0.000263}_{-0.000250}$
WASP-1 b	4.5	$5.41^{+0.17}_{-0.20}$	$86.5^{+1.2}_{-1.1}$	$1.09^{+0.02}_{-0.02}$	$0.33^{+6.58}_{-6.12}$	$24\,56\,371.982150^{+0.000354}_{-0.000364}$
HAT-P-26 b	3.6	$13.22^{+0.75}_{-0.94}$	$88.3^{+0.8}_{-0.7}$	$0.53^{+0.01}_{-0.01}$	$0.39^{+10.08}_{-9.85}$	$24\,56\,545.361384^{+0.000296}_{-0.000288}$
HAT-P-26 b	4.5	$13.92^{+0.16}_{-0.32}$	$89.5^{+0.3}_{-0.6}$	$0.55^{+0.01}_{-0.01}$	$0.11^{+4.33}_{-8.72}$	$24\,56\,405.622835^{+0.000356}_{-0.000364}$
WASP-107 b	3.6	$18.19^{+0.03}_{-0.04}$	$89.9^{+0.1}_{-0.1}$	$1.96^{+0.01}_{-0.01}$	$0.04^{+1.45}_{-2.26}$	$24\,57\,876.124941^{+0.000060}_{-0.000064}$
WASP-107 b	4.5	$18.09^{+0.05}_{-0.09}$	$89.8^{+0.1}_{-0.2}$	$2.06^{+0.01}_{-0.01}$	$0.06^{+2.54}_{-3.09}$	$24\,57\,870.403743^{+0.000081}_{-0.000077}$
WASP-13 b	3.6	$7.64^{+0.20}_{-0.19}$	$85.6^{+0.4}_{-0.3}$	$0.86^{+0.01}_{-0.01}$	$0.58^{+2.70}_{-2.50}$	$24\,56\,480.940869^{+0.000231}_{-0.000246}$
WASP-13 b	4.5	$7.78^{+0.27}_{-0.23}$	$85.7^{+0.4}_{-0.4}$	$0.87^{+0.01}_{-0.01}$	$0.59^{+3.43}_{-2.85}$	$24\,56\,315.526437^{+0.000293}_{-0.000303}$
WASP-121 b	3.6	$3.84^{+0.02}_{-0.03}$	$88.9^{+0.8}_{-1.1}$	$1.47^{+0.01}_{-0.01}$	$0.07^{+2.95}_{-4.10}$	$24\,57\,906.807311^{+0.000148}_{-0.000144}$
WASP-121 b	4.5	$3.82^{+0.02}_{-0.03}$	$89.0^{+0.8}_{-1.3}$	$1.49^{+0.01}_{-0.01}$	$0.07^{+3.02}_{-4.80}$	$24\,57\,910.632374^{+0.000183}_{-0.000171}$
WASP-69 b	3.6	$12.26^{+0.09}_{-0.08}$	$86.8^{+0.0}_{-0.0}$	$1.60^{+0.00}_{-0.00}$	$0.68^{+0.60}_{-0.58}$	$24\,57\,992.354188^{+0.000053}_{-0.000054}$
WASP-69 b	4.5	$12.30^{+0.11}_{-0.10}$	$86.8^{+0.1}_{-0.1}$	$1.67^{+0.01}_{-0.01}$	$0.68^{+0.77}_{-0.71}$	$24\,57\,996.222243^{+0.000066}_{-0.000069}$
WASP-67 b	3.6	$13.50^{+0.39}_{-0.33}$	$86.2^{+0.2}_{-0.2}$	$1.97^{+0.03}_{-0.03}$	$0.91^{+2.28}_{-2.72}$	$24\,57\,776.271136^{+0.000219}_{-0.000220}$
WASP-67 b	4.5	$13.90^{+0.31}_{-0.39}$	$86.3^{+0.1}_{-0.1}$	$1.92^{+0.03}_{-0.03}$	$0.89^{+1.84}_{-1.93}$	$24\,57\,979.305753^{+0.000282}_{-0.000276}$
HATS-7 b	3.6	$11.09^{+0.62}_{-1.07}$	$88.2^{+1.0}_{-1.3}$	$0.38^{+0.02}_{-0.02}$	$0.35^{+11.03}_{-14.14}$	$24\,57\,694.120917^{+0.000590}_{-0.000538}$
HATS-7 b	4.5	$10.80^{+0.48}_{-0.91}$	$88.4^{+1.1}_{-1.2}$	$0.40^{+0.03}_{-0.03}$	$0.30^{+12.05}_{-13.12}$	$24\,57\,697.305788^{+0.000797}_{-0.000795}$
WASP-29 b	3.6	$12.58^{+0.05}_{-0.11}$	$89.7^{+0.2}_{-0.4}$	$0.95^{+0.01}_{-0.01}$	$0.07^{+2.95}_{-4.91}$	$24\,57\,807.234478^{+0.000115}_{-0.000120}$
WASP-29 b	4.5	$12.53^{+0.05}_{-0.08}$	$89.7^{+0.2}_{-0.3}$	$0.93^{+0.01}_{-0.01}$	$0.06^{+2.59}_{-4.13}$	$24\,57\,826.848225^{+0.000150}_{-0.000149}$
HAT-P-41 b	3.6	$5.53^{+0.03}_{-0.06}$	$89.0^{+0.7}_{-0.9}$	$1.00^{+0.01}_{-0.01}$	$0.10^{+3.76}_{-4.92}$	$24\,57\,772.203860^{+0.000220}_{-0.000217}$
HAT-P-41 b	4.5	$5.55^{+0.03}_{-0.04}$	$89.3^{+0.5}_{-0.8}$	$1.09^{+0.01}_{-0.01}$	$0.07^{+2.78}_{-4.43}$	$24\,57\,788.367795^{+0.000274}_{-0.000263}$
WASP-101 b	3.6	$8.60^{+0.17}_{-0.16}$	$85.2^{+0.2}_{-0.2}$	$1.18^{+0.01}_{-0.01}$	$0.73^{+1.55}_{-1.54}$	$24\,57\,760.332526^{+0.000170}_{-0.000175}$
WASP-101 b	4.5	$8.51^{+0.19}_{-0.18}$	$85.0^{+0.2}_{-0.2}$	$1.14^{+0.01}_{-0.01}$	$0.74^{+1.72}_{-1.64}$	$24\,57\,771.089626^{+0.000225}_{-0.000227}$
WASP-131 b	3.6	$8.34^{+0.20}_{-0.19}$	$85.0^{+0.2}_{-0.2}$	$0.61^{+0.01}_{-0.01}$	$0.73^{+1.88}_{-1.80}$	$24\,57\,696.837080^{+0.000253}_{-0.000256}$
WASP-131 b	4.5	$8.41^{+0.28}_{-0.26}$	$85.0^{+0.3}_{-0.3}$	$0.61^{+0.01}_{-0.01}$	$0.73^{+2.63}_{-2.53}$	$24\,57\,909.718452^{+0.000336}_{-0.000332}$
WASP-36 b	3.6	$6.06^{+0.25}_{-0.22}$	$83.7^{+0.6}_{-0.5}$	$1.78^{+0.03}_{-0.03}$	$0.67^{+3.75}_{-3.19}$	$24\,57\,805.166629^{+0.000262}_{-0.000262}$
WASP-36 b	4.5	$6.19^{+0.44}_{-0.39}$	$84.4^{+1.1}_{-1.0}$	$1.82^{+0.03}_{-0.03}$	$0.60^{+6.70}_{-6.13}$	$24\,57\,975.813843^{+0.000346}_{-0.000353}$
WASP-63 b	3.6	$6.26^{+0.23}_{-0.21}$	$86.6^{+1.0}_{-0.8}$	$0.61^{+0.01}_{-0.01}$	$0.37^{+6.38}_{-5.07}$	$24\,57\,865.520635^{+0.000353}_{-0.000330}$
WASP-63 b	4.5	$6.52^{+0.16}_{-0.21}$	$87.7^{+1.1}_{-1.0}$	$0.55^{+0.01}_{-0.01}$	$0.26^{+7.01}_{-6.45}$	$24\,57\,922.436423^{+0.000470}_{-0.000461}$
WASP-79 b	3.6	$7.31^{+0.15}_{-0.14}$	$85.9^{+0.3}_{-0.3}$	$1.20^{+0.01}_{-0.01}$	$0.52^{+2.36}_{-2.05}$	$24\,57\,713.374126^{+0.000167}_{-0.000167}$
WASP-79 b	4.5	$7.12^{+0.15}_{-0.14}$	$85.6^{+0.3}_{-0.3}$	$1.17^{+0.01}_{-0.01}$	$0.55^{+2.29}_{-2.02}$	$24\,57\,720.699409^{+0.000215}_{-0.000213}$
WASP-94 Ab	3.6	$7.34^{+0.02}_{-0.04}$	$89.5^{+0.3}_{-0.5}$	$1.12^{+0.01}_{-0.01}$	$0.06^{+2.43}_{-3.56}$	$24\,57\,795.021530^{+0.000147}_{-0.000147}$
WASP-94 Ab	4.5	$7.34^{+0.02}_{-0.04}$	$89.5^{+0.4}_{-0.5}$	$1.13^{+0.01}_{-0.01}$	$0.07^{+2.62}_{-3.61}$	$24\,57\,972.780291^{+0.000187}_{-0.000180}$
WASP-74 b	3.6	$4.75^{+0.08}_{-0.07}$	$79.7^{+0.3}_{-0.2}$	$0.87^{+0.01}_{-0.01}$	$0.85^{+1.17}_{-1.01}$	$24\,57\,768.164558^{+0.000178}_{-0.000176}$
WASP-74 b	4.5	$5.13^{+0.11}_{-0.10}$	$80.8^{+0.3}_{-0.3}$	$0.86^{+0.01}_{-0.01}$	$0.82^{+1.44}_{-1.42}$	$24\,57\,770.304101^{+0.000228}_{-0.000230}$
WASP-62 b	3.6	$9.47^{+0.16}_{-0.16}$	$88.2^{+0.4}_{-0.3}$	$1.29^{+0.01}_{-0.01}$	$0.30^{+3.57}_{-3.02}$	$24\,57\,717.229937^{+0.000138}_{-0.000138}$
WASP-62 b	4.5	$9.32^{+0.20}_{-0.18}$	$87.9^{+0.4}_{-0.3}$	$1.20^{+0.01}_{-0.01}$	$0.35^{+3.88}_{-3.05}$	$24\,57\,730.466206^{+0.000165}_{-0.000167}$
Kepler-45 b	3.6	–	–	$3.37^{+0.13}_{-0.13}$	–	–
Kepler-45 b	4.5	–	–	$3.50^{+0.14}_{-0.14}$	–	–

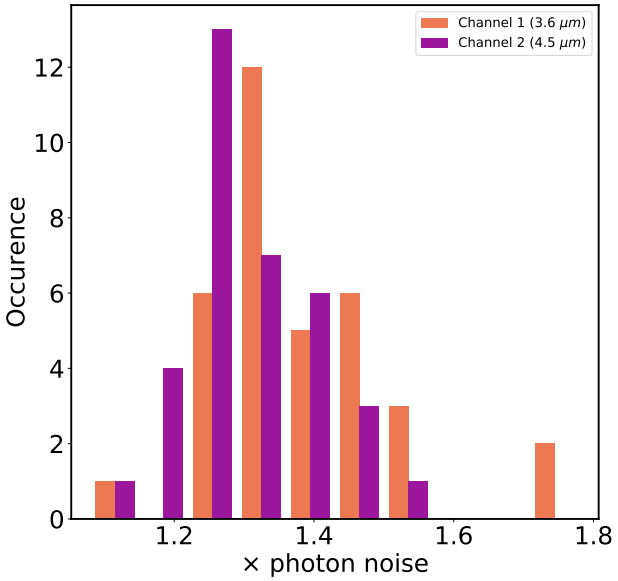


Fig. 8. Histogram showing the percentage above photon noise for each of the individual light curves. Channel 1 (3.6 μm) is displayed in orange and channel 2 (4.5 μm) in purple.

Table 5. Correlations between parameters and the transit depth ratio.

Parameter	r	p	Res Var
T_{eq} ($a=0$)	−0.35	0.01	7.23
T_{eff}	−0.34	0.02	7.14
Stellar log (g)	0.13	0.36	6.98
[Fe/H]	−0.21	0.15	4.48
R_p	−0.26	0.07	8.11
Inclination	0.20	0.18	7.03
a (AU)	0.07	0.63	8.46
Planetary log (g)	0.01	0.92	8.47
M_p (M_J)	0.09	0.56	8.78
H (km)	−0.17	0.25	8.50
R_s ($R_\odot$)	−0.40	0.00	7.06
Radius anomaly	−0.25	0.14	6.86

Notes. We show the Pearson correlation coefficient (r), the associated chance probability (p), and the residual variance from an ODR linear fit to the data.

the scale height (H) of each planet, ($H = kT_{eq}/\mu g$) calculated assuming a hydrogen-dominated atmosphere with mean molecular weight (μ) of 2.3, equilibrium temperature (T_{eq}) calculated with zero albedo and zero redistribution, and planetary surface gravity (g) from the literature.

In Table 6 we show the weighted mean of the normalized transit depth difference and the corresponding number of scale heights for each temperature bin in Fig. 5. We also calculate the weighted mean of the absolute value of the normalized transit depth difference and the number of scale heights.

We find that the weighted mean of the absolute value normalized transit depth difference and the number of scale heights to be significant to 8.0σ and 7.5σ respectively. This means that we are statistically detecting the atmosphere with a very high significance.

All nine of the cool (<1000 K) planets lie on the positive side of the transit depth metric with a weighted mean transit depth of 0.029 ± 0.007, 4.0σ from zero (gray assumption). We also find that the weighted mean transit depth difference and the number of scale heights of the 1000–2000 K planets and the >2000 K planets are not significant (<3σ). We therefore treat all planets >1000 K as one sample. These 36 hot planets have an absolute value weighted mean that is 0.3σ from zero (cloudy) assumption. In total, 14 of these planets are consistent with the cloudy models (zero) within 1σ. However, as these hot planets span both positive and negative values of the transit depth difference, it is unsurprising that their weighted mean transit depth is only marginally deviating from zero. The weighted mean of the absolute value of the difference in the transit depths for the hot planets is 0.025 ± 0.004 (5.9σ) and is more scattered than the cooler planets.

4.2. Results from the 1D grid of model transmission spectra

4.2.1. General trends observed in the grids of models

In Fig. 6 we show a selection of tracks from the complete grid of models and in Fig. 7 we show each interpolated grid as a shaded region in comparison with the survey data. The fiducial model grid (1x solar and equilibrium chemistry, no vertical mixing $K_{zz} = 0$) plotted in Fig. 6 shows the effect of increasing equilibrium temperatures on the transit depths. At ∼900 K, the model grid switches from a negative transit depth difference to a positive transit depth difference.

The interpolated grid shows a spread in the expected difference in the two transit depths. An important aspect of the model grid that largely influences the spread is the surface gravity. Lower surface gravities result in larger scale heights and lead to a larger signal in the difference of the two *Spitzer*/IRAC transit depths. The surface gravity also changes the shape of the TP profile as seen in Fig. 3. Figure 6 shows the effect of different surface gravities. We designed the model grid to span the parameters of the survey, notably with surface gravities of g = 500, 1000, 1500, and 5000 cm s^{-2}. However, for the ultra-hot model planets with low surface gravity of g = 500 cm s^{-2}, the upper atmosphere exceeds the Hill radius. These models do not represent any planets in our survey because the hottest planets in our survey tend to have larger surface gravity ($g \sim 1000$ cm s^{-2}. We therefore discard these model planets from Fig. 7.

The effect of vertical mixing can be seen in Fig. 6. A large amount of mixing results in the transition between CH_4 and CO occurring at higher temperatures. Increasing the metallicity to 30x solar has the effect of lowering the temperature of the transition between negative and positive transit depth difference. Increased metallicity also results in a stronger positive signal for the hotter planets >1000 K.

4.2.2. Statistical comparison of planet atmospheres with the model grid

We compare the data with the grids of models quantitatively by calculating the average number of standard deviations (based on the 1σ uncertainties) between each of the planets and their corresponding model grid point with the closest input parameters (T_{eq}, log (g_p), R_s and R_p). We then compute a weighted average for the whole grid, such that we can express the statistical significance of each grid with one number. We split this comparison into different temperature regimes based on the expected carbon chemistry. We compare the data to a transit depth difference of zero, representing a gray cloud opacity. Additionally, we also compare the data with the grids of models qualitatively by interpolating a shaded region between grid points, allowing us to

Table 6. Weighted means of the normalized transit depth difference ($(\delta_{ch2} - \delta_{ch1})/\delta_{ch1}$), the absolute value of the normalized transit depth difference, the corresponding number of scale heights (NH), and its absolute value.

Planet selection	$(\delta_{ch2} - \delta_{ch1})/\delta_{ch1}$	$N\sigma$	$\lvert(\delta_{ch2} - \delta_{ch1})/\delta_{ch1}\rvert$	$N\sigma$	NH	$N\sigma$	|NH|	$N\sigma$
All planets	0.010 ± 0.005	1.9σ	0.028 ± 0.003	8.0σ	0.2201 ± 0.0935	2.4σ	0.5032 ± 0.0669	7.5σ
<1000 K	0.029 ± 0.007	4.0σ	0.032 ± 0.006	5.1σ	0.4515 ± 0.1179	3.8σ	0.4900 ± 0.1043	4.7σ
1000–2000 K	0.002 ± 0.006	0.3σ	0.023 ± 0.005	5.0σ	0.0130 ± 0.1343	0.1σ	0.4840 ± 0.0968	5.0σ
>2000 K	−0.032 ± 0.015	2.2σ	0.042 ± 0.010	4.1σ	−0.5907 ± 0.4271	1.4σ	0.9239 ± 0.3322	2.8σ

Notes. This is shown for the different temperature ranges (<1000 K, 1000–2000 K, and >2000 K) presented in Fig. 5. The intermediate columns labeled Nσ indicate the significance of the previous weighted mean and weighted error.

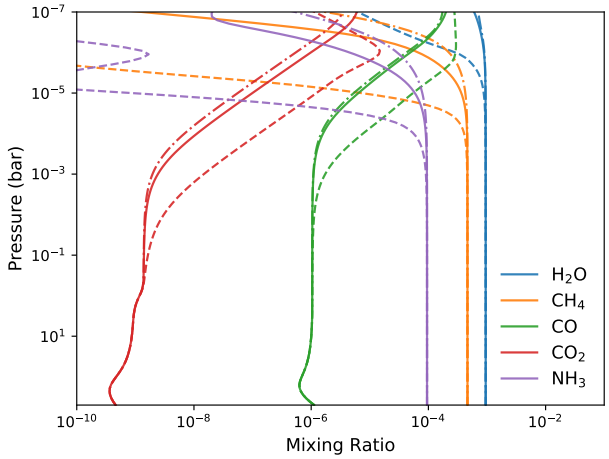


Fig. 9. Abundance mixing ratios at different pressures for the main species in the *Spitzer* bandpasses. The solid line shows the nominal situation ($a = 0.035$ AU, $T_{eff} = 3750$ K), the dashed line shows $a = 0.06$ AU, $T_{eff} = 4250$ K, and the dashed-dotted line shows $a = 0.017$ AU, $T_{eff} = 4250$ K.

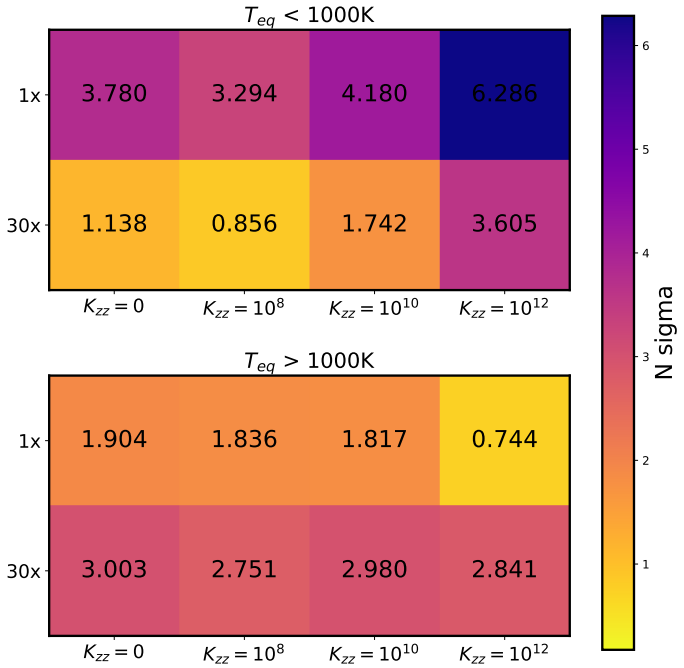


Fig. 10. Number of sigmas between the data and each model grid. We do this for eight grids and three sets or subsets of planets. The eight model grids are composed of two different metalicities (1x and 30x Solar) and four different vertical mixing scenarios ($K_{zz} = 0, 10^8, 10^{10}$ and 10^{12} cm^2 s^{-1}). The color bar represents the average number of sigmas between each model grid and the set of data; a lower N sigma (yellow) means a better fit. The *top panel* shows the results for the cool planets ($T_{eq} < 1000$ K) and the *bottom panel* shows the hot planets ($T_{eq} > 1000$ K). The number of sigmas is written on each cell.

visually compare the models with the *Spitzer*/IRAC transit depth difference; for example see Fig. 5.

In Sect. 3.2.1, we fix the orbital distance to 0.035 AU in our model grid creation. We do this because in our sample of planets the equilibrium temperature has a much larger correlation with the stellar effective temperature than with the semi-major axis. The range of semi-major axes in our sample spans ~0.017 to ~0.06 AU. We explore how much our choice of model parameterization (fixing the orbital distance to 0.035 AU) affects our results with the following two tests. We start by creating models with the minimum and maximum orbital distance of our sample, 0.017 and 0.06 AU.

In the first test, we match the equilibrium temperature by changing the effective temperature of the star. For a 650 K planet, an orbital distance of 0.017 AU corresponds to a stellar effective temperature of 3250 K and 0.06 AU corresponds to 4250 K. Figure 9 shows the effects on chemistry, where the star with higher T_{eff} provides greater flux even at larger orbit and leads to more photolysis. Nevertheless, it mainly impacts the main species at the lower pressures ($P < 1$ mbar). We find that the resulting difference in our transit depth metric for a planet placed at the minimum and maximum orbital distance is 0.0025. This is a factor of ten smaller than the mean error bar in our sample, so we do not expect this to change our results.

In the second test, we match the equilibrium temperature by changing the stellar radius. This time the resulting difference in our transit depth metric is 3.2e-6, which is three orders of magnitude smaller than the mean error bar of our sample. As the changes in the models are so small compared to the size of the uncertainties, we do not expect that the different orbital distances are the reason behind the scatter seen in Fig. 5.

Figure 10 displays the results of the statistical comparison of each model grid with the planets in our survey. Each planet transit depth measurement is compared to the corresponding transmission model with the closest parameters (T_{eq}, log (g_p), R_s and R_p). We calculate the statistical significance for a set of planets, which is quantified by the average number of sigmas, for all eight grids of models. In the two panels of Fig. 10 we show the results of the cool planets ($T_{eq} < 1000$ K), followed by the hot planets ($T_{eq} > 1000$ K). We find that the hot planets are best fit by 1x solar and high vertical mixing, $K_{zz} = 10^{12}$ cm^2 s^{-1}. We rule out high-metallicity models for these planets to ~3σ confidence.

On the other hand, we find that the cool planets are best fit by 30x solar and a low amount of vertical mixing ($K_{zz} = 10^8$ or $K_{zz} = 0$ cm^2 s^{-1}). We find that the 1x solar composition and high amounts of vertical mixing ($K_{zz} = 10^{12}$ cm^2 s^{-1}) are ruled out with $>3\sigma$ confidence for these cool planets.

Comparing the model grids to the full sample, we find that the full sample mimics the cool sample. This is because the different grids of models are divergent at the cool temperatures, and so the results from the cool temperatures drive the statistical results for the full grid.

5. Discussion

5.1. Expected opacities at 3.6 and 4.5 μm

The features we see in the transmission spectra are a result of the underlying chemistry at the pressures probed by our observations. Figure 4 shows the abundance-weighted opacities for the dominant opacity sources in the grid of models at the wavelengths of the *Spitzer* bandpasses. The dominating absorbing molecules in the *Spitzer* bandpasses are CH_4 and H_2O at 3.6 μm, and CO, H_2O, and CO_2 (for high metallicities) at 4.5 μm. As H_2O opacity is about equally present in both IRAC bandpasses, the two *Spitzer* transit depths can be used to understand the relative abundance of CO and CH_4. The following summary chemical reaction plays an important role in determining the dominating carbon-bearing species in an atmosphere (e.g., Visscher et al. 2010; Moses et al. 2011; Visscher & Moses 2011; Ebbing & Gammon 2016):

$$CH_4 + H_2O \rightleftharpoons CO + 3\,H_2.$$

At temperatures higher than ∼1100 K the forward reaction is favored (CO creation) for nominal pressures of ∼1 bar, whereas at temperatures lower than ∼1100 K the reverse reaction is favored (CH_4 creation; e.g., Madhusudhan 2012; Mollière et al. 2015; Molaverdikhani et al. 2019). The gas transition between CH_4 and CO is plotted as a function of temperature in Fig. 3. This shows where the abundance of CH_4 and CO are the same (Visscher 2012). A temperature pressure profile crossing this line results in CO or CH_4 becoming the dominant absorber.

We therefore expect that the atmospheres of planets in thermochemical equilibrium with temperatures above ∼1100 K have CO as the dominating carbon-bearing species and the cooler atmospheres have CH_4. The result of this on the normalized difference of the transit depths (Fig. 5) is that the CH_4 planets would have a negative difference whereas CO planets have a positive difference. The transition from negative to positive transit depth differences seen in Figs. 5, 6, and 7 shows the changing carbon chemistry (CH_4 to CO) with increasing equilibrium temperature. We find that the equilibrium temperature of the transition in the fiducial model grid (thermochemical equilibrium, 1x solar) is slightly lower than the 1100 K presented in a previous study (e.g., Madhusudhan 2012). We emphasize that the transition from CH_4 to CO depends on the temperature and pressure of the layer being probed with *Spitzer*/IRAC transmission photometry, and that this temperature is not necessarily at the equilibrium temperature of the planet.

5.2. The transit survey

5.2.1. Comparing transit depths to fiducial model grid

Figure 5 shows the normalized difference of the two *Spitzer* transit depths with the fiducial grid of models. The fiducial models are calculated with opacities from thermochemical equilibrium and 1x solar composition. The sample of planets with temperatures hotter than 1000 K follow the fiducial models, but we see that the cool planets appear to deviate from this model grid. As we see that different chemical and physical processes are likely occurring at these different equilibrium temperatures, we proceed by splitting Fig. 5 into three temperature regimes based on the expected chemistry from our model grid: the cooler, methane planets (<1000 K), the hotter, carbon monoxide hot planets (1000–2000 K), and the few ultra-hot planets where molecular dissociation can occur ($T_{eq} > 2000$ K).

There are 13 planets in our survey with $T_{eq} < 1000$ K. Our fiducial (1x solar and no vertical mixing) models demonstrate that the predicted carbon-bearing species for planets in this temperature regime is methane, which results in the models occupying the negative side of Fig. 5. However, we find that the data show the opposite trend: all planets lie on the right side of Fig. 5. We find that this equilibrium chemistry grid is ruled out at 3.8σ, which is statistically capturing the dearth of methane in the sample of coolest planets; see Sect. 4.2.2. This supports previous individual studies of cool gas giants with HST/WFC3 and indicates that there are more complex physical processes happening that are not included in the fiducial models.

There are 28 planets in the mid-temperate/hot range (1000–2000 K) and 8 planets in the hot/ultra-hot range (>2000 K) of Fig. 5. Of these 36 hot/ultra-hot planets, 14 are consistent to less than 1σ with the cloud-free solar composition model grid. In Sect. 4.2.2 we show that these planets are consistent with the fiducial model grid to 2σ. Additionally, we find that there is only 1 of these 36 hot/ultra-hot planets with a stronger positive signal than the fiducial model grid, meaning that a model grid with a higher CO abundance (e.g., 30x solar) is not required to explain our sample of observations. We find that 30x solar is ruled out with 3σ confidence for the hotter planets.

There are several effects not included in the fiducial grid of models that contribute to the statistical deviation. For example, we assume solar metallicity, no vertical mixing, and cloud-free atmospheres. We compare the survey of planets to the model grids in a statistical manner and discuss the effects of each of these in detail below.

5.2.2. Effect of metallicity in hot Jupiter atmospheric spectra

The metallicity of a planet contributes to the atmospheric molecular abundances. Our fiducial model grid assumes 1x solar composition and solar metallicity. Increasing the metallicity would increase the amount of CO in the atmosphere (e.g., Venot et al. 2014). Figure 6 shows a 30x solar track and Fig. 7 shows the whole interpolated grid (with no vertical mixing; see the first panel). Increasing the metallicity to 30x solar results in a lower temperature at which the model atmospheres transition between CH_4 and CO. This transition occurs at a temperature of around 600 K, much lower than the transition of 900 K for the fiducial grid.

In Sect. 4.2.2 we show that the cool planets lack the methane signature and are better fit with 30x solar composition models, with a significance of $>2.5\sigma$. This is the case for the lower values of vertical mixing ($K_{zz} = 0$, 10^8 and 10^{10} cm^2 s^{-1}) discussed in more detail in Sect. 5.2.3. These cool planets are also generally lower mass planets because of the detection biases for these systems; see Fig. 1. Lower mass planets typically have higher metallicities (Fortney et al. 2013; Welbanks et al. 2019). Therefore, a higher average metallicity in the 13 planets with temperatures <1000 K likely explains the lack of methane. Our

findings support the predicted high metal enrichment in cool gas giants presented by Espinoza et al. (2017). These latter authors predict C/O ratios for a sample of 50 gas giants with $T_{eq} < 1000$ K; 6 of our 13 planets in this temperature range are also in their sample. Furthermore, our finding of high metallicity for these coolest warm giant planets supports the individual high-metallicity measurements of several planets in the literature: HAT-P-12b (Line et al. 2013), HAT-P-26b (Wakeford et al. 2017), GJ 436b (Morley et al. 2017) and HAT-P-11b (Mansfield et al. 2018). All of these exoplanet atmospheres are found to have super-solar metallicities, except for GJ 3470b which is suggested to have a relatively low atmospheric metallicity for its planet mass (Benneke et al. 2019). Furthermore, upon reanalysis of the HST/WFC3 data from Mansfield et al. (2018), and combination with data from *Spitzer* and HST/STIS, Chachan et al. (2019) find that HAT-P-11 b's atmosphere might also have low metallicity.

On the other hand, the planets with equilibrium temperatures >1000 K are consistent with the 1x solar composition models to less than 2σ for all values of K_{zz}. The higher metallicity grid is less favored for these planets (2.6σ deviation). Similar to the high abundance of CO at cooler temperatures, the high-metallicity model grid shows stronger CO features throughout the entire temperature range, which is not favored by the planets in our survey. We do not find it necessary to statistically invoke high metallicity to explain the near-infrared spectral features of hot Jupiters.

Figure 4 shows the opacities for the 1x and 30x metallicity used in the creation of our model grids. In practice, differences in the opacities for the two cases would also affect the temperature pressure profile. However, in our analysis we do not compute the temperature pressure profiles self consistently. Nevertheless, we can predict what effect this might have. Higher metallicities would result in hotter temperatures in our TP profiles, which would in turn result in a larger CO/CH_4 ratio. This means that we could explain the dearth of methane with less extreme enhancements in the metallicity of the models.

5.2.3. Vertical mixing and nonequilibrium effects

Another aspect not included in our fiducial model grid is the presence of nonequilibrium effects such as photochemistry, advection, convection, and turbulence in the atmosphere. To capture some of these nonequilibrium atmospheric processes, we introduce an eddy diffusion coefficient, K_{zz}, into our modeling (see Sect. 3.2.3). Theory suggests that, for hot Jupiters, K_{zz} can range from 10^8 to 10^{12} cm^2 s^{-1} based on the estimation from the mean vertical wind in GCMs (Moses et al. 2011). We create four different grids of models spanning the range of eddy diffusion coefficients: equilibrium chemistry, $K_{zz} = 10^8$, $K_{zz} = 10^{10}$, and $K_{zz} = 10^{12}$ cm^2 s^{-1}.

The models incorporating different K_{zz} show that the transition between CH_4 and CO being the dominating carbon bearer in these atmospheres occurs at higher temperatures for larger values of K_{zz}. This is because with larger values of K_{zz}, the mixing penetrates deeper into the atmosphere and can therefore dredge up methane to the observable pressures of hotter planets where methane is not expected. The models on Fig. 7 (right panel) demonstrate that $K_{zz} = 10^{12}$ cm^2 s^{-1} can dredge up CH_4 for planets up to 1300 K.

For the cool planet data ($T < 1000$ K), we find that the models containing low amounts of vertical mixing are significantly favored over high vertical mixing for both metallicities. For 30x solar metallicity, the low mixing $K_{zz} = 10^8$ cm^2 s^{-1} fits marginally better than equilibrium chemistry ($K_{zz} = 0$) and is a 3σ better fit than the high vertical mixing ($K_{zz} = 10^{12}$ cm^2 s^{-1}). On the other hand, for the hot planets we find that $K_{zz} = 10^{12}$ cm^2 s^{-1} is favored over the lower mixing or no mixing for both the 1x and 30x solar metallicities.

Komacek et al. (2019) showed that for tidally locked hot Jupiters, vertical mixing increases with increasing equilibrium temperature and rotation rates: starting at $K_{zz} = 10^7$–10^8 cm^2 s^{-1} for the coolest (500 K) planets and going to $K_{zz} = 10^{11}$–10^{12} cm^2 s^{-1} for the hottest (1500–3000 K). We find that the cool planets support these results, with a vertical mixing of $K_{zz} = 10^8$ cm^2 s^{-1} favored by the data. However, the hotter planets seem to suggest a lower level of mixing than theory predicts, our models with $K_{zz} = 10^{10}$ cm^2 s^{-1} are marginally supported over the equilibrium and $K_{zz} = 10^8$ cm^2 s^{-1} grids, which is lower than the theoretical maximum of $K_{zz} = 10^{12}$ cm^2 s^{-1}. These findings are in line with the findings of Miles et al. (2020) for nonequilibrium processes in brown dwarfs. These latter authors found warmer brown dwarfs showed lower mixing than theory predicts, yet the cooler objects were close to the theoretical maximum.

Additionally, our nonequilibrium chemistry models include the effects of photochemical reactions. For hot planets ($T_{eq} > 1000$ K), CO is only dissociated in the upper atmosphere due to its strong bond, which has negligible influence on the *Spitzer* bandpasses. For cooler planets ($T_{eq} \leq 1000$ K), CH_4 is dissociated by atomic hydrogen produced by photolysis. This destruction of CH_4 can penetrate down to around 0.1 mbar with lower mixing ($K_{zz} = 10^8$ cm^2 s^{-1}). Nevertheless, the competing effects of mixing can overtake and efficiently transport methane to the upper atmosphere. HCN is also produced by photochemistry and can reach abundances close to CH4 in some cases. Nevertheless, HCN absorbs similarly at the two IRAC wavelengths, and so we do not expect it to have significant effects on the normalized transit depth difference.

As vertical mixing is responsible for dredging up CH_4 to observable pressures in the hotter planets, and not for dredging CO to observable pressures in the cooler planets, we conclude that the dearth of methane is not due to strong atmospheric mixing, but is likely due to the higher metallicity of these atmospheres. Another possible factor affecting the lack of methane signatures in the cool planets could be the amount of interior heating; see Fortney et al. (2020). We find that several of the coolest planets are eccentric (see Table A.1), which could cause some tidal heating. Our temperature pressure profile calculation assumes an interior heating of $T_{int} = 150$ K. However, substantial interior heating, $T_{int} > 300$ K, could result in pushing the deeper layers of these atmospheric TP profiles towards the CO regime (Morley et al. 2017; Benneke et al. 2019; Thorngren et al. 2019, 2020). If the interior is more CO dominated, then vertical mixing could dredge up CO in the cooler planets, resulting in a dearth of methane (e.g., Moses et al. 2013). We did not test this as it is beyond the scope of our paper.

5.2.4. Effects of clouds on the cool and hot Jupiter atmospheric spectra

Clouds are ubiquitous in transiting exoplanet atmospheres (Sing et al. 2016). There are several mechanisms responsible for producing homogeneous and inhomogeneous clouds on tidally locked planets (Parmentier et al. 2013, 2021; Helling et al. 2016, 2019b,a). An example can be found in Line & Parmentier (2016) in which HD 189733b and HAT-P-11b can be explained by

patchy clouds without the need to invoke global clouds or high mean molecular weight atmospheres.

Hazes are expected to be prominent in the cooler atmospheres. Morley et al. (2015) predicted that a transition between haze-free and hazy atmospheres will occur at 800–1100 K, implying that any planet below this temperature might show no molecular features. Gao et al. (2020) showed that the amplitude of the HST/WFC3 water feature on planets with temperatures <900 K is such that these atmospheres become dominated by haze formation. However, Kawashima & Ikoma (2019) predict that molecular features such as CO and CH_4 are still detectable in the infrared for their sample of warm Jupiters (<1000 K) with hazy atmospheres.

Furthermore, if all planets with temperatures <1000 K in our survey were characterized by a gray cloud opacity, then we would expect the transit depth difference to be evenly distributed around zero in Fig. 5. However, these 13 planets have a mean transit depth of 0.026 ± 0.008. This rules out a gray cloud (flat spectrum) at 4.0σ confidence for all planets, suggesting that these planets cannot be characterized by a gray cloud opacity, and that there is a molecular feature.

Molaverdikhani et al. (2020) suggested that clouds could play a role in the heating of the atmosphere, resulting in a lack of CH_4. However, such clouds would also dampen the CO feature significantly. This effect could be the reason for the few planets consistent with zero, but we do not expect that this effect explains the 4.0σ detection for the sample of cool planets (<1000 K).

There are 14 planets with equilibrium temperature >1000 K that have transit depth differences consistent with zero (flat spectrum). The weighted mean transit depth difference of all these planets is −0.002 ± 0.006, only 0.3σ. However, the weighted mean of the absolute value of the transit depth difference is 0.025 ± 0.004 (5.9σ).

Based on the prediction by Morley et al. (2015) we would not expect hazes at these temperatures. However, Gao et al. (2020) show that the HST water feature is dampened when compared to a cloud-free atmosphere, and they find the data is better fit by their models containing silicate clouds. Furthermore, Line & Parmentier (2016) suggested that patchy cloud cover can mimic the spectral features of a high-mean-molecular-weight atmosphere, resulting in a flatter transmission spectrum. Additionally, due to the varying temperature across the day and night sides of tidally locked highly irradiated hot Jupiters, clouds and hazes may behave differently at the east and west terminators of the planet (Kempton et al. 2017) such that photochemically generated hazes formed on the day side can be blown over to the nightside and dampen the transmission features. We therefore expect clouds to indeed play a role in dampening the spectral features in some of our planets, namely those in the temperature region predicted to be cloudy by Gao et al. (2020) (>1000 K).

However, as there is still a strong signal in the absolute value of the transit depths of these planets (5.9σ), there is indication that the population cannot be captured by a completely featureless model. Mie scattering theory results in a drop off in cloud opacity at 2–3 μm (e.g., Benneke et al. 2019). As we are detecting molecular features between 3 and 5 μm, it may be that any possible cloud particles exhibit Mie scattering in this regime. Including Mie scattering as a cloud prescription in our transmission-spectrum forward modeling is beyond the scope of this paper. However, cloud opacity that is lower at 4.5 μm than it is at 3.6 μm would result in a negative transit depth metric, similar to the expected methane signature. However, we do not find planets with a negative transit depth metric, and hence find no evidence for Mie scattering clouds.

5.2.5. Outliers and the effect of nightsides

According to our grids of models, we do not expect any of the planets above 1400 K to have CH_4 as the dominating carbon-bearing species in any of the metallicity or mixing scenarios. However, there are two hot planets that are significantly on the left: HD 149026b and WASP-33b (2.9σ and 3.5σ from zero respectively). HD 149026b has previously been discrepant from models. For example, Zhang et al. (2018) found that they needed 30x solar metallicity to reproduce the *Spitzer* 3.6 and 4.5 μm phase curves. Furthermore, the biggest outlier, WASP-33 b, is a planet that is orbiting a δ Scuti star, with pulsating periods close to the transit duration (Herrero et al. 2011). Both of these planets indicate that there may be additional factors that could significantly affect the transit light curves, but statistically it is not unexpected to have a couple of outliers. In Sect. 5.2.7 we discuss how we treat stellar variability for the whole survey.

Additionally, three of the seven hottest planets above 2000 K (WASP-33b, WASP-121b, and WASP-18b) show evidence of a temperature inversion (von Essen et al. 2015; Haynes et al. 2015; Evans et al. 2017; Arcangeli et al. 2018). However, transmission spectroscopy is not as sensitive to the temperature profile at low resolution (e.g., Brown 2001) and so we do not expect to see the effect of temperature inversions in the transit depth difference of the two *Spitzer*/IRAC bandpasses. Additionally, the H^- opacity seen at the WFC3 bandpass (e.g., Arcangeli et al. 2018) does not become important at the *Spitzer*/IRAC bandpasses until equilibrium temperatures as high as 3500 K.

5.2.6. Radius anomaly

Our sample subsequently spans a very large range of scale heights ranging from HAT-P-2b with a scale height of 26 km to WASP-31b with a scale height of 1150 km. Figure 5 demonstrates that there is no trend with the atmospheric scale height and the strength of the spectral features indicated by the magnitude of the transit depth metric. Furthermore, the radius anomaly is thought to correlate with incident flux, with hotter planets having a more inflated radius (Thorngren & Fortney 2018). However, we do not find a trend with the radius anomaly and the strength of the spectral features seen with *Spitzer* (see Fig. C.1).

5.2.7. Stellar variability

Contamination of the transmission spectrum from starspots, faculae, and flares generates brightness temperature differences between the disk-integrated spectra of the star and the region occulted by a transiting planet (Désert et al. 2011d; Pont et al. 2008; Sing et al. 2011). If a planet occults a star spot at a different temperature to the photospheric one, it can change the shape of the light curve by appearing as a change in the flux during transit. On the other hand, if the star spot is not occulted, then the disk-integrated spectrum of the star is fainter or brighter, depending on the spot properties, which can cause the measured transit depth to be different from the nominal one. Stellar variability can occur when star spots rotate in and out of view of the integrated stellar disk, which depends on the rotation period of the star.

To estimate the possible effect of stellar variability on our results, we aim to provide a quantitative estimate of how this would affect the sample as a whole by expanding the interpolated model grid. We do this by looking at a worst-case-scenario variable star, HD 189733, which has a peak-to-peak variability of ∼3% in the visible (Henry & Winn 2008). We follow the method in Désert et al. (2011d); Sing et al. (2011) and Berta et al. (2012)

to calculate the effect of this variability on the transit depth metric. We first translate this 3% in V-band to 0.8% at 3.6 µm using the ratio of black bodies; we set 2.8% spot coverage with spots at 1000 K less than the stellar photosphere. We can propagate this to a relative error on the transit depth and assuming it will affect 4.5 µm as much as 3.6 µm (in reality it will be a smaller effect), we can then propagate this to an error on the transit depth metric ($\delta_{ch2} - \delta_{\rm ch1}/\delta_{\rm ch1}$). This leads to a 42% maximum error on the transit depth metric, and we therefore extend the models positive and negative by this percentage, which is plotted in Fig. 5.

Despite choosing the worst-case scenario to expand our model grid, the features arising from the changing chemistry with equilibrium temperature can still be clearly distinguished in the grid of models in Fig. 5, that is, the transition regions at ∼1000 and ∼2200 K remain clear. The relative size of the variability region is on average one-third of the size of the average uncertainty on the data points. Nevertheless, this is a conservative upper estimate and will not apply as strongly to all planets in our sample, because not all stars are as variable as HD 189733. If the temperature difference between spot and photosphere is less or if the spot covering fraction is smaller, then this would result in a lower variability amplitude and smaller effect on the transmission spectrum. Additionally, 3% is the maximum peak-to-peak variability, and this would only apply if the observations were taken at the peak and trough of the variability period. As we designed the observations to have as few orbital periods as possible to be within one variability period of the star, it is unlikely that we reach the maximum variability between our two *Spitzer* observations.

5.3. Comparing transmission and emission with warm Spitzer/IRAC

Several of the planets from our survey have published secondary eclipse measurements. We utilize the secondary eclipse literature survey from Baxter et al. (2020, and references therein) which contains 3.6 and 4.5 µm eclipses for 78 planets in total. Several of the eclipse depths presented in Table 1 of Baxter et al. (2020) were taken from Garhart et al. (2020), and some of these planets had dilution corrections due to companions in the field of view. The dilution corrections were applied before any analysis in Baxter et al. (2020), but this was not reported in their Table 1. We therefore report the eclipse depths with dilution corrections in Table A.2 of this work using the dilution correction factors presented in Table 4 of Garhart et al. (2020). We use the eclipse depth, equilibrium temperature, brig and 4.5 µm, and the deviation from the black body presented in Baxter et al. (2020). The deviation from the black body probes the temperature pressure profile. A positive deviation is either methane in absorption at 3.6 µm with a nominal TP profile or CO in emission at 4.5 µm if the TP profile is inverted. Twenty-four of the planets in Baxter et al. (2020) are also in our transmission survey, which allows us to statistically compare the two samples. To better understand the dearth of methane planets presented in Sect. 4.2.2, we compare the difference in brightness temperature from emission with the normalized difference in transit depths for planets with both emission and transmission observations. Additionally, we create a color–magnitude plot and compare the emission to the brown dwarf spectral sequence with a focus on the coolest planets.

5.3.1. Probing different pressures with emission and transmission

In Baxter et al. (2020), we demonstrate that the relative opacities in the two *Spitzer*/IRAC bandpasses can act as a probe of

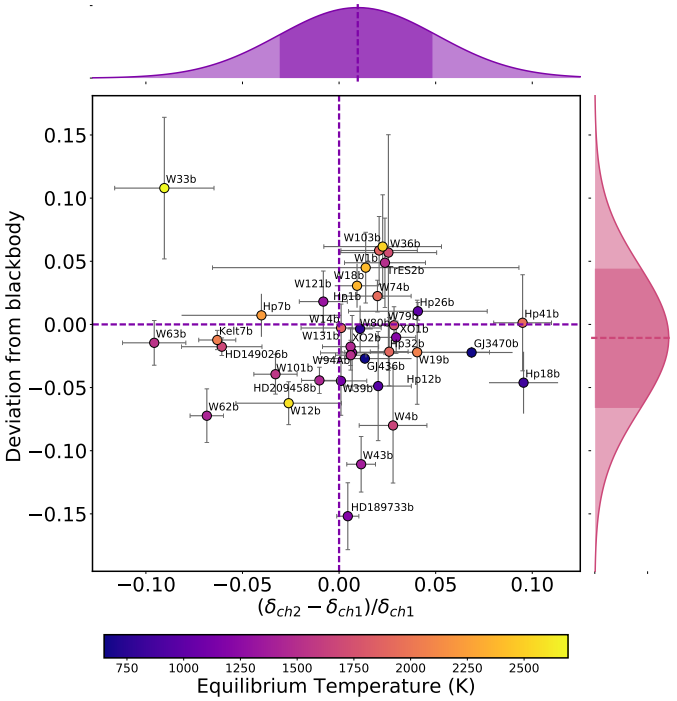


Fig. 11. Deviation from a black body calculated from emission against the normalized difference in the transit depth presented in Fig. 5. Histograms on each axis show the mean and standard deviation of each axis. The equilibrium temperature of each planet is shown with the color scale.

the atmospheric temperature structure when observing the dayside emission. The deviation from black body metric described in Baxter et al. (2020) plotted against the equilibrium temperature shows that ultra-hot Jupiters show statistical evidence for thermal inversion. In a noninverted atmosphere, a positive deviation indicates that the 3.6 µm brightness temperature is lower than that at 4.5 µm due to methane absorption at 3.6 µm and a negative deviation indicates that the 4.5 µm T_b is lower due to CO absorption at 4.5 µm. On the other hand, if the atmosphere is inverted, CO being the dominating carbon-bearing species in the atmosphere would result in a positive deviation due to seeing CO in emission at 4.5 µm. In this work we are focusing on the CH_4-to-CO transition temperature and thus we do not account for temperature inversions.

In Fig. 11 we compare the difference of the two IRAC brightness temperatures against the normalized difference in the transit depth. There appear to be no trends in the emission and transmission of the planets in our survey with both eclipses and transits, and we also find that the top left quadrant is almost empty, with the main outlier being WASP-33b. Given that the deviation from the black body can be positive or negative for a CO-dominated atmosphere depending on the TP profile, we test for trends in the planets with equilibrium temperatures below 1800 K, which are not expected to have thermal inversions in their atmospheres. We find that the top-left quadrant, which indicates CH_4 in transmission and CH_4 in emission, is empty, meaning that any planets that show signs of methane in their emission do not show it in their transmission, and vice versa. For example, HD 149026b lies in the bottom-left quadrant, and has a negative deviation from a black body, which indicates a CO absorption feature in emission (assuming a noninverted TP profile). The expected corresponding transmission spectrum would predict a positive transit depth difference. However, this is not what we see. Possible reasons for

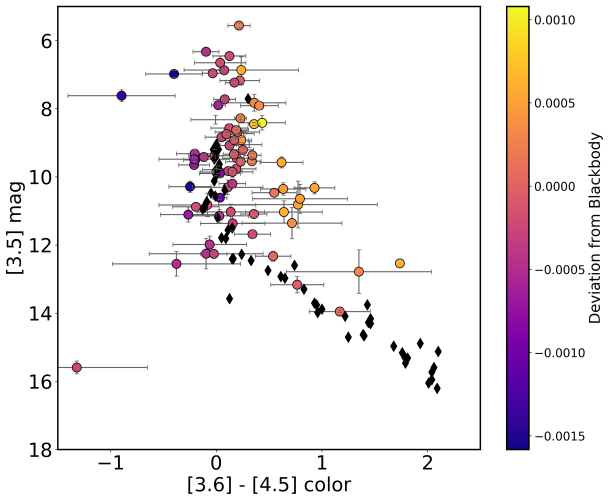


Fig. 12. [3.6]–[4.5] color vs. [3.6] magnitude diagram of exoplanets and brown dwarf planets with available eclipse depth measurements in the two warm *Spitzer* band-passes. Brown dwarf colors (estimated from the WISE catalog) are shown as black diamonds from Dupuy & Liu (2012). The color scale is the deviation from a black body metric described Baxter et al. (2020).

these differences include: longitudinal abundance differences, more complex atmospheric processes such as atmospheric mixing, different cloud composition/abundances at different layers in the atmosphere, or changes in the thermal structure between emission and transmission (e.g., Fortney 2005). Additionally, similar to the results for the planets in transmission, we do not find a correlation between the deviation of the black body and the radius anomaly.

5.3.2. Comparing to brown dwarfs with a color-magnitude diagram

We create also a color-magnitude plot using these *Spitzer* secondary eclipses. Our work expands on that presented in Triaud et al. (2014) by extending their survey from 37 planets to the 78 planets presented in Baxter et al. (2020) and by using the newly released *Gaia* DR2 for more accurate distances (Gaia Collaboration 2018). We calculate the planetary apparent magnitudes using the apparent stellar magnitudes from the WISE spacecraft (Cutri et al. 2012) in combination with the planet-to-star-flux ratio from *Spitzer*. The two WISE channels W1 and W2 are known to overlap the two remaining *Spitzer* channels (Kirkpatrick et al. 2011). We then use the *Gaia* DR2 distances which were calculated using a Bayesian prior from Gaia Collaboration (2018) and Bailer-Jones et al. (2018) to calculate the planetary absolute magnitudes. The equilibrium temperature, *Gaia* distances, and WISE magnitudes used are provided in Table A.2. Errors are propagated fully throughout the calculation from the errors on all input properties.

Figure 12 shows the [3.6]–[4.5] color versus [3.6] magnitude diagram. We have over-plotted the survey of brown dwarfs spanning M, L, and T spectral classes from Dupuy & Liu (2012) for comparison. The planets plotted in Fig. 12 show an increasing scatter with increasing 3.6 µm magnitude. This is unlike the brown dwarf spectral sequence which follows a very tight L/T transition. This increase in scatter confirms that seen in Triaud (2014); Beatty et al. (2014); Melville et al. (2020) and Dransfield & Triaud (2020), which is suggested to be due to an increase in atmospheric diversity.

Figure 12 shows that the increase in scatter is driven by a small family of planets which lie redder than the brown dwarf spectral sequence. The color scale shows that this family of planets shows a positive deviation from a black body (Baxter et al. 2020), which indicates methane absorption (nominal TP profile) or CO emission (inverted TP profile). As these planets are around 1200–1500 K, we do not expect their atmospheres to be inverted, and we therefore think that these warmer planets could be displaying a signature of methane in their atmospheres. In Sect. 4.1.5 we show that the cooler planets (<1000 K) deviate from equilibrium chemistry models by not showing signatures of methane in their atmospheres. Similarly, these warmer planets are not expected to have a high methane abundance given their equilibrium chemistry, and again we have to invoke nonequilibrium processes such as vertical mixing. Warmer planets are expected to have greater vertical mixing than their cooler counterparts (Komacek et al. 2019), creating an ideal scenario for methane dredge-up.

Furthermore, brown dwarfs are expected to undergo less mixing than gas giant planets, with K_{zz} ranging from 10^4 to $10^{8.5}$ for brown dwarfs and 10^7 to 10^{12} for gas giants (Zahnle & Marley 2014; Leggett et al. 2017; Miles et al. 2020). Although this prediction is based on nonirradiated, higher gravity objects with mostly convective atmospheres, GCMs of highly irradiated, radiative atmospheres of hot Jupiters do display stronger mixing (Parmentier et al. 2013; Komacek et al. 2019). We therefore propose that the increased atmospheric diversity of planets compared to their brown dwarf counterparts seen in Fig. 12 could be due in part to the diversity of the processes involved, such as the presence of vertical mixing.

6. Conclusion

We performed the data analysis of 70 light curves and presented a total of 49 planets with transit depths at 3.6 and 4.5 µm with *Spitzer*/IRAC. This survey represents the largest analysis of *Spitzer*/IRAC observations of gas giant transits to date, and spans equilibrium temperatures from 500 to 2700 K. We implemented our custom *Spitzer*/IRAC data analysis pipeline which thoroughly searches over a grid of data-reduction parameters before employing pixel-level decorrelation (Deming et al. 2015) to correct for the strong *Spitzer* systematic errors and extract the transit depths using an MCMC transit-fitting algorithm.

We then statistically studied the sample of all planets with transmission in these two bandpasses. We create a fiducial cloud-free 1D atmospheric model grid with 1x solar composition and equilibrium chemistry spanning the parameters of the planets in our sample. We compare the survey of planets with this model grid and note a family of outliers with equilibrium temperature <1000 K; they do not show the expected methane abundance from these equilibrium chemistry models.

Next, we expanded our grid in two dimensions by extending to 30x solar metallicity and incorporating nonequilibrium effects with different values of an eddy diffusion co-efficient (K_{zz}). We find that the best-fitting grid for the cool planets ($T < 1000$ K) has high metallicity (30x solar) and low or no vertical mixing ($K_{zz} = 0$ or 10^8 cm^2 s^{-1}). On the other hand, we find that the hot planets ($T > 1000$ K) are best explained with 1x solar composition with a marginally better fit with the high vertical mixing model ($K_{zz} = 10^{12}$ cm^2 s^{-1}). We conclude that the cool planets are better fit by models with higher metallicity due to an observational bias resulting in lower masses. We find evidence supporting nonequilibrium chemistry in a survey of planets and

find that our work agrees with the theory that hotter planets have higher vertical mixing. Blumenthal et al. (2018) investigate the *James Webb* Space Telescope observability of disequilibrium chemistry. They find that differences between equilibrium and disequilibrium could be detected with one eclipse of a planet similar to WASP-80b.

Furthermore, we combine our transits with our previous literature eclipse survey. We do not find any trend between eclipses and transits, and propose that this is due to several effects: clouds at different pressures or more complex atmospheric processes. We created a color–magnitude diagram using the emission observations and compared to L/T transition brown dwarfs. With a larger sample size than previous studies, we also see the increase in scatter with increasing magnitude first seen by Triaud et al. (2014). We see that the increase in scatter is driven by a family of mid-temperate planets showing a methane signature that is not expected from equilibrium chemistry. We propose that this increase in scatter is due to methane being dredged up due to high levels of vertical mixing in the atmosphere, which supports the theory that brown dwarfs have approximately 100 times lower levels of vertical mixing than planets.

Acknowledgements. This work is based on observations made with the *Spitzer* Space Telescope, which is operated by the Jet Propulsion Laboratory, California Institute of Technology under a contract with NASA. Support for this work was provided by NASA through an award issued by JPL/Caltech. J.M.D. acknowledges support from NASA grant NNX16AC64G, the Amsterdam Academic Alliance (AAA) Program, and the European Research Council (ERC) European Union's Horizon 2020 research and innovation program (grant agreement no. 679633; Exo-Atmos). S.-M. Tsai thanks Michael Zhang for supporting the free-chemistry version of PLATON. S.-M. Tsai acknowledges support from the European community through the ERC advanced grant EXOCONDENSE (PI: R. T. Pierrehumbert). This work has made use of the MUSCLES Treasury Survey High-Level Science Products; doi:10.17909/T9DG6F. The analysis done in this project made use of the SciPy stack (Virtanen et al. 2020), including NumPy (Oliphant 2006), Matplotlib (Hunter 2007), Pandas (Pandas development team 2020). It also made use of Astropy (Astropy Collaboration 2018), pysynphot (STScI Development Team 2013), sklearn (Pedregosa et al. 2011), photutils (Bradley et al. 2020), batman (Kreidberg 2015), emcee (Foreman-Mackey et al. 2013) and corner (Foreman-Mackey 2016). Models in this paper made use of the VULCAN code which is available at `https://github.com/exoclime/VULCAN`.

References

Agol, E., Cowan, N. B., Knutson, H. A., et al. 2010, ApJ, 721, 1861
Agúndez, M., Venot, O., Iro, N., et al. 2012, A&A, 548, A73
Agúndez, M., Venot, O., Selsis, F., & Iro, N. 2014, ApJ, 781, 68
Anderson, D. R., Collier Cameron, A., Hellier, C., et al. 2011a, A&A, 531, A60
Anderson, D. R., Smith, A. M. S., Lanotte, A. A., et al. 2011b, MNRAS, 416, 2108
Anderson, D. R., Smith, A. M. S., Madhusudhan, N., et al. 2013, MNRAS, 430, 3422
Anderson, D. R., Collier Cameron, A., Delrez, L., et al. 2014, MNRAS, 445, 1114
Arcangeli, J., Désert, J.-M., Line, M. R., et al. 2018, ApJ, 855, L30
Astropy Collaboration (Price-Whelan, A. M., et al.) 2018, AJ, 156, 123
Bailer-Jones, C. A. L., Rybizki, J., Fouesneau, M., Mantelet, G., & Andrae, R. 2018, AJ, 156, 58
Bakos, G. Á., Penev, K., Bayliss, D., et al. 2015, ApJ, 813, 111
Ballard, S., Charbonneau, D., Deming, D., et al. 2010, PASP, 122, 1341
Barros, S. C. C., Pollacco, D. L., Gibson, N. P., et al. 2012, MNRAS, 419, 1248
Barstow, J. K., Aigrain, S., Irwin, P. G. J., & Sing, D. K. 2017, ApJ, 834, 50
Baskin, N. J., Knutson, H. A., Burrows, A., et al. 2013, ApJ, 773, 124
Baxter, C., Désert, J.-M., Parmentier, V., et al. 2020, A&A, 639, A36
Beatty, T. G., Collins, K. A., Fortney, J., et al. 2014, ApJ, 783, 112
Beerer, I. M., Knutson, H. A., Burrows, A., et al. 2011, ApJ, 727, 23
Benneke, B., Knutson, H. A., Lothringer, J., et al. 2019, Nat. Astron., 3, 813
Berta, Z. K., Charbonneau, D., Désert, J.-M., et al. 2012, ApJ, 747, 35
Biddle, L. I., Pearson, K. A., Crossfield, I. J. M., et al. 2014, MNRAS, 443, 1810
Blecic, J., Harrington, J., Madhusudhan, N., et al. 2013, ApJ, 779, 5
Blecic, J., Harrington, J., Madhusudhan, N., et al. 2014, ApJ, 781, 116
Blumenthal, S. D., Mandell, A. M., Hébrard, E., et al. 2018, ApJ, 853, 138
Boggs, P. T., Donaldson, J. R., Byrd, R. h., & Schnabel, R. B. 1989, ACM Trans. Math. Softw., 15, 348
Bouchy, F., Hebb, L., Skillen, I., et al. 2010, A&A, 519, A98
Bradley, L., Sipocz, B., Robitaille, T., et al. 2020, `https://doi.org/10.5281/zenodo.4049061`
Brown, T. M. 2001, ApJ, 553, 1006
Burke, C. J., McCullough, P. R., Valenti, J. A., et al. 2007, ApJ, 671, 2115
Burke, C. J., McCullough, P. R., Bergeron, L. E., et al. 2010, ApJ, 719, 1796
Carone, L., Mollière, P., Zhou, Y., et al. 2021, A&A, 646, A168
Chachan, Y., Knutson, H. A., Gao, P., et al. 2019, AJ, 158, 244
Charbonneau, D., Allen, L. E., Megeath, S. T., et al. 2005, ApJ, 626, 523
Charbonneau, D., Knutson, H. A., Barman, T., et al. 2008, ApJ, 686, 1341
Christiansen, J. L., Ballard, S., Charbonneau, D., et al. 2010, ApJ, 710, 97
Collier Cameron, A., Bouchy, F., Hébrard, G., et al. 2007, MNRAS, 375, 951
Crossfield, I. J. M. 2015, PASP, 127, 941
Cubillos, P., Harrington, J., Madhusudhan, N., et al. 2013, ApJ, 768, 42
Cutri, R. M., et al. 2012, VizieR Online Data Catalog: II/311
Delrez, L., Santerne, A., Almenara, J. M., et al. 2016, MNRAS, 458, 4025
Deming, L. D., & Seager, S. 2017, J. Geophys. Res. Planets, 122, 53
Deming, D., Knutson, H., Agol, E., et al. 2011, ApJ, 726, 95
Deming, D., Fraine, J. D., Sada, P. V., et al. 2012, ApJ, 754, 106
Deming, D., Knutson, H., Kammer, J., et al. 2015, ApJ, 805, 132
Désert, J.-M., Bean, J., Miller-Ricci Kempton, E., et al. 2011a, ApJ, 731, L40
Désert, J.-M., Charbonneau, D., Demory, B.-O., et al. 2011b, ApJS, 197, 14
Désert, J.-M., Charbonneau, D., Fortney, J. J., et al. 2011c, ApJS, 197, 11
Désert, J. M., Sing, D., Vidal-Madjar, A., et al. 2011d, A&A, 526, A12
Diamond-Lowe, H., Stevenson, K. B., Bean, J. L., Line, M. R., & Fortney, J. J. 2014, ApJ, 796, 66
Doyle, L. R., Carter, J. A., Fabrycky, D. C., et al. 2011, Science, 333, 1602
Dransfield, G., & Triaud, A. H. M. J. 2020, MNRAS, 499, 505
Drummond, B., Tremblin, P., Baraffe, I., et al. 2016, A&A, 594, A69
Dupuy, T. J., & Liu, M. C. 2012, ApJS, 201, 19
Ebbing, D., & Gammon, S. D. 2016, General Chemistry (Boston: Cengage Learning)
Espinoza, N., Fortney, J. J., Miguel, Y., Thorngren, D., & Murray-Clay, R. 2017, ApJ, 838, L9
Esteves, L. J., De Mooij, E. J. W., & Jayawardhana, R. 2015, ApJ, 804, 150
Evans, T. M., Sing, D. K., Kataria, T., et al. 2017, Nature, 548, 58
Faedi, F., Barros, S. C. C., Anderson, D. R., et al. 2011, A&A, 531, A40
Fazio, G. G., Hora, J. L., Allen, L. E., et al. 2004, ApJS, 154, 10
Foreman-Mackey, D. 2016, J. Open Source Softw., 1, 24
Foreman-Mackey, D., Hogg, D. W., Lang, D., & Goodman, J. 2013, PASP, 125, 306
Fortney, J. J. 2005, MNRAS, 364, 649
Fortney, J. J., Shabram, M., Showman, A. P., et al. 2010, ApJ, 709, 1396
Fortney, J. J., Demory, B.-O., Désert, J.-M., et al. 2011, ApJS, 197, 9
Fortney, J. J., Mordasini, C., Nettelmann, N., et al. 2013, ApJ, 775, 80
Fortney, J. J., Visscher, C., Marley, M. S., et al. 2020, AJ, 160, 288
Fraine, J. D., Deming, D., Gillon, M., et al. 2013, ApJ, 765, 127
France, K., Loyd, R. O. P., Youngblood, A., et al. 2016, ApJ, 820, 89
Fressin, F., Knutson, H. A., Charbonneau, D., et al. 2010, ApJ, 711, 374
Fu, G., Deming, D., Knutson, H., et al. 2017, ApJ, 847, L22
Gaia Collaboration (Brown, A. G. A., et al.) 2018, A&A, 616, A1
Gao, P., Thorngren, D. P., Lee, G. K. H., et al. 2020, Nat. Astron., 4, 951
Garhart, E., Deming, D., Mandell, A., et al. 2020, AJ, 159, 137
Gelman, A., & Rubin, D. B. 1992, Stat. Sci., 7, 457
Gibson, N. P., Aigrain, S., Roberts, S., et al. 2012, MNRAS, 419, 2683
Guillot, T. 2010, A&A, 520, A27
Guilluy, G., Sozzetti, A., Brogi, M., et al. 2019, A&A, 625, A107
Guo, X., Crossfield, I. J. M., Dragomir, D., et al. 2020, AJ, 159, 239
Hartman, J. D., Bakos, G. Á., Kipping, D. M., et al. 2011a, ApJ, 728, 138
Hartman, J. D., Bakos, G. Á., Sato, B., et al. 2011b, ApJ, 726, 52
Hartman, J. D., Bakos, G. Á., Torres, G., et al. 2011c, ApJ, 742, 59
Hartman, J. D., Bakos, G. Á., Torres, G., et al. 2009, ApJ, 706, 785
Haynes, K., Mandell, A. M., Madhusudhan, N., Deming, D., & Knutson, H. 2015, ApJ, 806, 146
Hellier, C., Anderson, D. R., Collier Cameron, A., et al. 2010, ApJ, 723, L60
Hellier, C., Anderson, D. R., Collier Cameron, A., et al. 2012, MNRAS, 426, 739
Hellier, C., Anderson, D. R., Collier Cameron, A., et al. 2017, MNRAS, 465, 3693
Helling, C., Lee, G., Dobbs-Dixon, I., et al. 2016, MNRAS, 460, 855
Helling, C., Gourbin, P., Woitke, P., & Parmentier, V. 2019a, A&A, 626, A133
Helling, C., Iro, N., Corrales, L., et al. 2019b, A&A, 631, A79
Heng, K., Mendonça, J. M., & Lee, J.-M. 2014, ApJS, 215, 4
Henry, G. W., & Winn, J. N. 2008, AJ, 135, 68
Herrero, E., Morales, J. C., Ribas, I., & Naves, R. 2011, A&A, 526, L10
Holman, M. J., Fabrycky, D. C., Ragozzine, D., et al. 2010, Science, 330, 51
Hoyer, S., López-Morales, M., Rojo, P., et al. 2013, MNRAS, 434, 46

Hu, R., Seager, S., & Yung, Y. L. 2015, ApJ, 807, 8
Hunter, J. D. 2007, Comput. Sci. Eng., 9, 90
Ingalls, J. G., Krick, J. E., Carey, S. J., et al. 2016, AJ, 152, 44
Johnson, J. A., Gazak, J. Z., Apps, K., et al. 2012, AJ, 143, 111
Jones, E., Oliphant, T., Peterson, P., et al. 2001
Kammer, J. A., Knutson, H. A., Line, M. R., et al. 2015, ApJ, 810, 118
Kawashima, Y., & Ikoma, M. 2019, ApJ, 877, 109
Keating, D., Cowan, N. B., & Dang, L. 2019, Nat. Astron., 3, 1092
Kempton, E. M. R., Bean, J. L., & Parmentier, V. 2017, ApJ, 845, L20
Kirkpatrick, J. D., Cushing, M. C., Gelino, C. R., et al. 2011, ApJS, 197, 19
Knutson, H. A., Charbonneau, D., Allen, L. E., Burrows, A., & Megeath, S. T. 2008, ApJ, 673, 526
Knutson, H. A., Charbonneau, D., Burrows, A., O'Donovan, F. T., & Mandushev, G. 2009, ApJ, 691, 866
Knutson, H. A., Madhusudhan, N., Cowan, N. B., et al. 2011, ApJ, 735, 27
Komacek, T. D., Showman, A. P., & Parmentier, V. 2019, ApJ, 881, 152
Kreidberg, L. 2015, PASP, 127, 1161
Kreidberg, L., Line, M. R., Parmentier, V., et al. 2018a, AJ, 156, 17
Kreidberg, L., Line, M. R., Thorngren, D., Morley, C. V., & Stevenson, K. B. 2018b, ApJ, 858, L6
Kurucz, R. L. 1979, ApJS, 40, 1
Lanotte, A. A., Gillon, M., Demory, B. O., et al. 2014, A&A, 572, A73
Leggett, S. K., Tremblin, P., Esplin, T. L., Luhman, K. L., & Morley, C. V. 2017, ApJ, 842, 118
Lewis, N. K., Knutson, H. A., Showman, A. P., et al. 2013, ApJ, 766, 95
Line, M. R., & Parmentier, V. 2016, ApJ, 820, 78
Line, M. R., Vasisht, G., Chen, P., Angerhausen, D., & Yung, Y. L. 2011, ApJ, 738, 32
Line, M. R., Knutson, H., Deming, D., Wilkins, A., & Desert, J.-M. 2013, ApJ, 778, 183
Lodders, K., Palme, H., & Gail, H. P. 2009, Landolt Börnstein, 4B, 712
Lyons, L. 1992, J. Phys. A Math. General, 25, 1967
Machalek, P., McCullough, P. R., Burke, C. J., et al. 2008, ApJ, 684, 1427
Machalek, P., McCullough, P. R., Burrows, A., et al. 2009, ApJ, 701, 514
Machalek, P., Greene, T., McCullough, P. R., et al. 2010, ApJ, 711, 111
Maciejewski, G., Ohlert, J., Dimitrov, D., et al. 2014, Acta Astron., 64, 11
Maciejewski, G., Dimitrov, D., Mancini, L., et al. 2016, Acta Astron., 66, 55
Madhusudhan, N. 2012, ApJ, 758, 36
Mancini, L., Kemmer, J., Southworth, J., et al. 2016, MNRAS, 459, 1393
Mansfield, M., Bean, J. L., Oklopčić, A., et al. 2018, ApJ, 868, L34
Maxted, P. F. L., Anderson, D. R., Doyle, A. P., et al. 2013, MNRAS, 428, 2645
Melville, G., Kedziora-Chudczer, L., & Bailey, J. 2020, MNRAS, 494, 4939
Miles, B. E., Skemer, A. J. I., Morley, C. V., et al. 2020, AJ, 160, 63
Molaverdikhani, K., Henning, T., & Mollière, P. 2019, ApJ, 873, 32
Molaverdikhani, K., Henning, T., & Mollière, P. 2020, ApJ, 899, 53
Mollière, P., van Boekel, R., Dullemond, C., Henning, T., & Mordasini, C. 2015, ApJ, 813, 47
Morello, G., Waldmann, I. P., Tinetti, G., et al. 2015, ApJ, 802, 117
Morley, C. V., Fortney, J. J., Marley, M. S., et al. 2015, ApJ, 815, 110
Morley, C. V., Knutson, H., Line, M., et al. 2017, AJ, 153, 86
Moses, J. I., Visscher, C., Fortney, J. J., et al. 2011, ApJ, 737, 15
Moses, J. I., Line, M. R., Visscher, C., et al. 2013, ApJ, 777, 34
Močnik, T., Hellier, C., Anderson, D. R., Clark, B. J. M., & Southworth, J. 2017, MNRAS, 469, 1622
Neveu-VanMalle, M., Queloz, D., Anderson, D. R., et al. 2014, A&A, 572, A49
Nikolov, N., Sing, D. K., Pont, F., et al. 2014, MNRAS, 437, 46
Nymeyer, S., Harrington, J., Hardy, R. A., et al. 2011, ApJ, 742, 35
O'Donovan, F. T., Charbonneau, D., Harrington, J., et al. 2010, ApJ, 710, 1551
Oliphant, T. E. 2006, A Guide to NumPy (USA: Trelgol Publishing), 1
O'Rourke, J. G., Knutson, H. A., Zhao, M., et al. 2014, ApJ, 781, 109
Pandas development team 2020, https://doi.org/10.5281/zenodo.3509134
Parmentier, V., & Guillot, T. 2014, A&A, 562, A133
Parmentier, V., Showman, A. P., & Lian, Y. 2013, A&A, 558, A91
Parmentier, V., Showman, A. P., & Fortney, J. J. 2021, MNRAS, 501, 78
Pedregosa, F., Varoquaux, G., Gramfort, A., et al. 2011, J. Mach. Learning Res., 12, 2825
Petrucci, R., Jofré, E., Schwartz, M., et al. 2013, ApJ, 779, L23
Pont, F., Knutson, H., Gilliland, R. L., Moutou, C., & Charbonneau, D. 2008, MNRAS, 385, 109
Pont, F., Sing, D. K., Gibson, N. P., et al. 2013, MNRAS, 432, 2917
Quijada, M. A., Marx, C. T., Arendt, R. G., & Moseley, S. H. 2004, SPIE Conf. Ser., 5487, 244
Reach, W. T., Megeath, S. T., Cohen, M., et al. 2005, PASP, 117, 978
Rugheimer, S., Kaltenegger, L., Zsom, A., Segura, A., & Sasselov, D. 2013, Astrobiology, 13, 251
Sainsbury-Martinez, F., Wang, P., Fromang, S., et al. 2019, A&A, 632, A114
Seager, S., & Deming, D. 2010, ARA&A, 48, 631
Seager, S., & Sasselov, D. D. 2000, ApJ, 537, 916
Seeliger, M., Kitze, M., Errmann, R., et al. 2015, MNRAS, 451, 4060
Shporer, A., O'Rourke, J. G., Knutson, H. A., et al. 2014, ApJ, 788, 92
Sing, D. K. 2010, A&A, 510, A21
Sing, D. K., Désert, J. M., Fortney, J. J., et al. 2011, A&A, 527, A73
Sing, D. K., Fortney, J. J., Nikolov, N., et al. 2016, Nature, 529, 59
Skillen, I., Pollacco, D., Collier Cameron, A., et al. 2009, A&A, 502, 391
Smith, A. M. S., Anderson, D. R., Madhusudhan, N., et al. 2012, A&A, 545, A93
Southworth, J. 2008, MNRAS, 386, 1644
Sozzetti, A., Torres, G., Charbonneau, D., et al. 2007, ApJ, 664, 1190
Spake, J. J., Sing, D. K., Evans, T. M., et al. 2018, Nature, 557, 68
Stassun, K. G., Collins, K. A., & Gaudi, B. S. 2017, AJ, 153, 136
Stassun, K. G., Corsaro, E., Pepper, J. A., & Gaudi, B. S. 2018, AJ, 155, 22
Stassun, K. G., Oelkers, R. J., Paegert, M., et al. 2019, AJ, 158, 138
Steinrueck, M. E., Parmentier, V., Showman, A. P., Lothringer, J. D., & Lupu, R. E. 2019, ApJ, 880, 14
Stevenson, K., Harrington, J., Nymeyer, S., et al. 2010a, AAS/Div. Planet. Sci. Meeting Abstracts, 42, 27.13
Stevenson, K. B., Harrington, J., Nymeyer, S., et al. 2010b, Nature, 464, 1161
Stevenson, K. B., Harrington, J., Fortney, J. J., et al. 2012, ApJ, 754, 136
Stevenson, K. B., Bean, J. L., Madhusudhan, N., & Harrington, J. 2014, ApJ, 791, 36
Stevenson, K. B., Bean, J., Line, M. R., et al. 2016, AAS Meeting Abstracts, 227, 224.02
STScI Development Team 2013, pysynphot: Synthetic photometry software package [record ascl:1303.023]
Swain, M. R., Vasisht, G., & Tinetti, G. 2008, Nature, 452, 329
Thao, P. C., Mann, A. W., Johnson, M. C., et al. 2020, AJ, 159, 32
Thorngren, D. P., & Fortney, J. J. 2018, AJ, 155, 214
Thorngren, D. P., Fortney, J. J., Murray-Clay, R. A., & Lopez, E. D. 2016, ApJ, 831, 64
Thorngren, D., Gao, P., & Fortney, J. J. 2019, ApJ, 884, L6
Thorngren, D., Gao, P., & Fortney, J. J. 2020, ApJ, 889, L39
Tinetti, G., Deroo, P., Swain, M. R., et al. 2010, ApJ, 712, L139
Todorov, K., Deming, D., Harrington, J., et al. 2010, ApJ, 708, 498
Todorov, K. O., Deming, D., Knutson, H. A., et al. 2012, ApJ, 746, 111
Todorov, K. O., Deming, D., Knutson, H. A., et al. 2013, ApJ, 770, 102
Torres, G., Fressin, F., Batalha, N. M., et al. 2011, ApJ, 727, 24
Tremblin, P., Chabrier, G., Mayne, N. J., et al. 2017, ApJ, 841, 30
Triaud, A. H. M. J. 2014, MNRAS, 439, L61
Triaud, A. H. M. J., Lanotte, A. A., Smalley, B., & Gillon, M. 2014, MNRAS, 444, 711
Triaud, A. H. M. J., Gillon, M., Ehrenreich, D., et al. 2015, MNRAS, 450, 2279
Tsai, S.-M., Lyons, J. R., Grosheintz, L., et al. 2017, ApJS, 228, 20
Tsai, S.-M., Kitzmann, D., Lyons, J. R., et al. 2018, ApJ, 862, 31
Tsiaras, A., Waldmann, I. P., Zingales, T., et al. 2018, AJ, 155, 156
Venot, O., Agúndez, M., Selsis, F., Tessenyi, M., & Iro, N. 2014, A&A, 562, A51
Virtanen, P., Gommers, R., Oliphant, T. E., et al. 2020, Nat. Meth., 17, 261
Visscher, C. 2012, ApJ, 757, 5
Visscher, C., & Moses, J. I. 2011, ApJ, 738, 72
Visscher, C., Lodders, K., & Fegley, Bruce, J. 2010, ApJ, 716, 1060
von Essen, C., Mallonn, M., Albrecht, S., et al. 2015, A&A, 584, A75
Wakeford, H. R., Sing, D. K., Kataria, T., et al. 2017, Science, 356, 628
Wakeford, H. R., Sing, D. K., Deming, D., et al. 2018, AJ, 155, 29
Wallack, N. L., Knutson, H. A., Morley, C. V., et al. 2019, AJ, 158, 217
Welbanks, L., Madhusudhan, N., Allard, N. F., et al. 2019, ApJ, 887, L20
Werner, M. W., Roellig, T. L., Low, F. J., et al. 2004, ApJS, 154, 1
Wheatley, P. J., Collier Cameron, A., Harrington, J., et al. 2010, ArXiv eprints [arXiv:1004.0836]
Wong, I., Knutson, H. A., Lewis, N. K., et al. 2015, ApJ, 811, 122
Wong, I., Knutson, H. A., Kataria, T., et al. 2016, ApJ, 823, 122
Wright, J. T., Fakhouri, O., Marcy, G. W., et al. 2011, PASP, 123, 412
Zahnle, K. J., & Marley, M. S. 2014, ApJ, 797, 41
Zhang, X., & Showman, A. P. 2018, ApJ, 866, 2
Zhang, M., Knutson, H. A., Kataria, T., et al. 2018, AJ, 155, 83
Zhang, M., Chachan, Y., Kempton, E. M. R., & Knutson, H. A. 2019, PASP, 131, 034501
Zhao, M., O'Rourke, J. G., Wright, J. T., et al. 2014, ApJ, 796, 115
Zilinskas, M., Miguel, Y., Mollière, P., & Tsai, S.-M. 2020, MNRAS, 494, 1490

Appendix A: Pipeline results figures and tables

Table A.1. Jump parameters used as starting points for the MCMC analysis.

Planet	a/R_s	inc $^\circ$	R_p/R_s	Period days	Eccentricity	T_{eff} Kelvin	$\log(g_*)$ $\log_{10}(\mathrm{cm\,s^{-2}})$	[Fe/H] dex	Ref.
HAT-P-32 b	6.05(4)	88.9(4)	0.1508(4)	2.150008(1)	0.16(6)	6207(88)	4.33(1)	−0.04(8)	13
XO-1 b	11.24(9)	88.8(2)	0.1320(5)	3.94150685(91)	0	5750(75)	4.50(1)	0.02(8)	6
HAT-P-1 b	9.85(7)	85.63(06)	0.1180(2)	4.46529976(55)	0	5980(49)	4.36(1)	0.13(1)	19
WASP-17 b	7.05(7)	86.83(68)	0.13	3.7354380(68)	0.03(2)	6650(80)	4.16(3)	−0.19(9)	1
WASP-39 b	11.37(24)	87.75(27)	0.1457(16)	4.0552765(35)	0	5400(150)	4.4(2)	−0.12(10)	18,10
HAT-P-12 b	11.77(21)	89.0(4)	0.1406(13)	3.2130598(21)	0.03(3)	4650(60)	4.61(1)	−0.29(5)	11
HAT-P-18 b	16.04(75)	88.8(3)	0.1365(15)	5.508023(6)	0.08(5)	4803(80)	4.57(4)	0.10(08)	14
TrES2 b	7.90(2)	83.87(02)	0.1254(5)	2.47061317(9)	0.02(2)	5850(50)	4.43(2)	−0.15(10)	9, 22
WASP-4 b	5.46(2)	88.52(39)	0.1544(2)	1.33823204(16)	0.003(7)	5436(34)	4.46(5)	−0.05(4)	15,20
XO-2 b	8.18(3)	88.9(7)	0.1	2.615857(50)	0	5340(32)	4.48(5)	0.45(2)	5
GJ3470 b	13.94(49)	88.88(72)	0.0764(4)	3.3366487(43)	0.02(2)	3652(50)	4.78(12)	0.17(6)	3
WASP-21 b	9.62(17)	87.12(24)	0.1030(8)	4.3225126(22)	0	5800(100)	4.2(1)	−0.46(11)	21,4
WASP-31 b	8.00(19)	84.41(22)	0.127	3.4059096(50)	0	6302(102)	4.31(2)	−0.20(09)	2
WASP-1 b	5.69(6)	90.0(1.3)	0.1036(8)	2.5199454(5)	0.01(3)	6200(200)	4.3(3)	0.1(2)	17,7
HAT-P-26 b	13.44(83)	88.6(9)	0.0737(12)	4.234516(15)	0.12(6)	5079(88)	4.56(6)	−0.04(8)	12
WASP-107 b	18.2(1)	89.56(08)	0.1446(2)	5.72149242(46)	0	4430(120)	4.5(1)	0.02(10)	23
WASP-13 b	7.58(15)	85.64(24)	0.0922(8)	4.353011(13)	0	5826(100)	4.04(20)	0.0(2)	24,25
WASP-121 b	3.75(3)	87.6(6)	0.1245(5)	1.27492550(25)	0	6459(140)	4.24(1)	0.13(9)	26
WASP-69 b	11.96(17)	86.71(20)	0.1336(16)	3.8681382(17)	0	4700(50)	4.54(2)	0.15(8)	35
WASP-67 b	13.42(13)	85.8(3)	0.1345(48)	4.61442(1)	0	5417(85)	4.53(2)	0.18(6)	36
HATS7 b	10.59(51)	87.92(75)	0.0711(19)	3.185315(5)	0	4985(50)	4.54(5)	0.25(8)	37
WASP-29 b	12.15(44)	88.8(7)	0.101(2)	3.922719(7)	0.03(5)	4875(65)	4.54(4)	0.11(14)	38
HAT-P-41 b	5.45(18)	87.7(1.0)	0.1028(16)	2.694050(4)	0	6390(100)	4.14(2)	0.21(10)	32
WASP-101 b	8.45(30)	85.0(2)	0.1140(9)	3.585720(4)	0	6380(120)	4.31(8)	0.20(12)	32
WASP-131 b	8.53(9)	85.0(3)	0.0815(7)	5.322023(5)	0	6030(90)	4.09(3)	−0.18(8)	39
WASP-36 b	5.85(6)	83.15(13)	0.1368(6)	1.53736596(24)	0	5959(134)	4.49(1)	−0.26(10)	40
WASP-63 b	6.59(30)	87.8(1.3)	0.0781(11)	4.378080(6)	0	5550(100)	4.01(3)	0.08(7)	32
WASP-79 b	7.03(36)	85.4(6)	0.1049(24)	3.662380(5)	0	6600(100)	4.20(15)	0.03(1)	32
WASP-94 Ab	7.3(7)	88.7(7)	0.1094(8)	3.9501907(44)	0	6153(75)	4.18(1)	0.26(15)	41
WASP-74 b	4.86(20)	79.81(24)	0.0964(7)	2.137750(1)	0	5990(110)	4.39(7)	0.03(10)	33
WASP-62 b	9.55(41)	88.30(75)	0.1095(9)	4.411950(3)	0	6230(80)	4.45(10)	0.04(6)	34
Kepler-45 b	10.6(1.0)	87.0(7)	0.179(2)	2.455239(4)	0.11(10)	3820(90)	3.1(1)	0.13(13)	16

Notes. Eccentricity was fixed to zero for all planets because it did not affect the resulting transit depths. Stellar parameters (T_{eff}, $\log g$ and [Fe/H]) are used to calculate linear limb-darkening parameters.

References. (1) Anderson et al. (2011b); (2) Anderson et al. (2011a); (3) Biddle et al. (2014); (4) Bouchy et al. (2010); (5) Burke et al. (2007); (6) Burke et al. (2010); (7) Collier Cameron et al. (2007); (8) Doyle et al. (2011); (9) Esteves et al. (2015); (10) Faedi et al. (2011); (11) Hartman et al. (2009); (12) Hartman et al. (2011a); (13) Hartman et al. (2011c); (14) Hartman et al. (2011b); (15) Hoyer et al. (2013); (16) Johnson et al. (2012); (17) Maciejewski et al. (2014); (18) Maciejewski et al. (2016); (19) Nikolov et al. (2014); (20) Petrucci et al. (2013); (21) Seeliger et al. (2015); (22) Sozzetti et al. (2007); (23) Močnik et al. (2017); (24) Barros et al. (2012); (25) Skillen et al. (2009); (26) Delrez et al. (2016); (27) Holman et al. (2010); (28) Torres et al. (2011); (32) Stassun et al. (2017); (33) Stassun et al. (2018); (34) Stassun et al. (2019); (35) Anderson et al. (2014); (36) Hellier et al. (2012); (37) Bakos et al. (2015); (38) Hellier et al. (2010); (39) Hellier et al. (2017); (40) Mancini et al. (2016) and (41) Neveu-VanMalle et al. (2014).

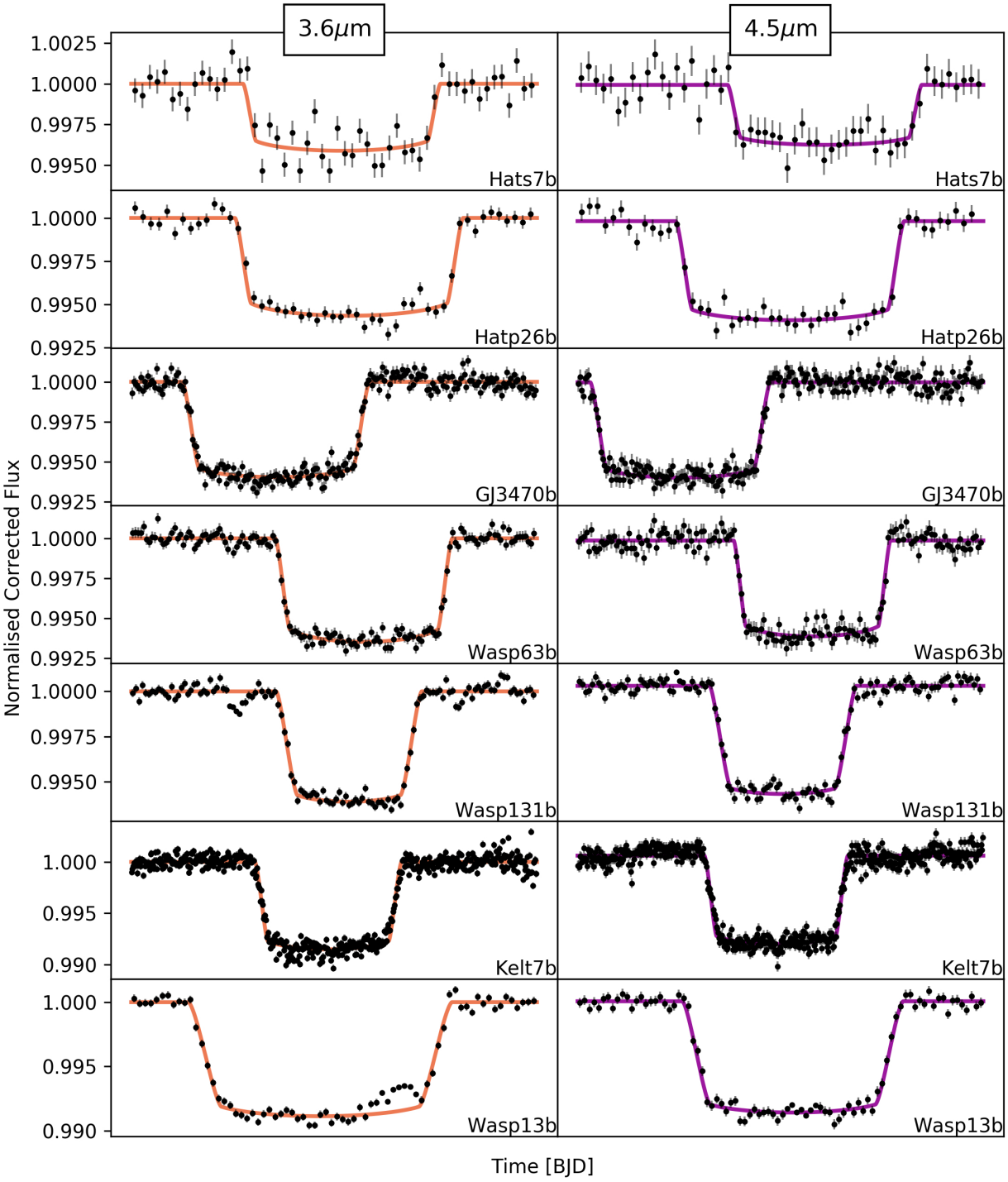


Fig. A.1. Normalized and systematic-error-corrected transit light curves for each planet at 3.6 (*left column*, orange) and 4.5 μm (*right column*, purple). 1 σerror bars are those originally calculated from scaled photon noise. The data and the error bars are binned in five-minute intervals for display purposes. Continuous curves show the best-fit transit models in each band-pass for comparison. Kepler-45b displays the result of four phase folded light curves in each channel.

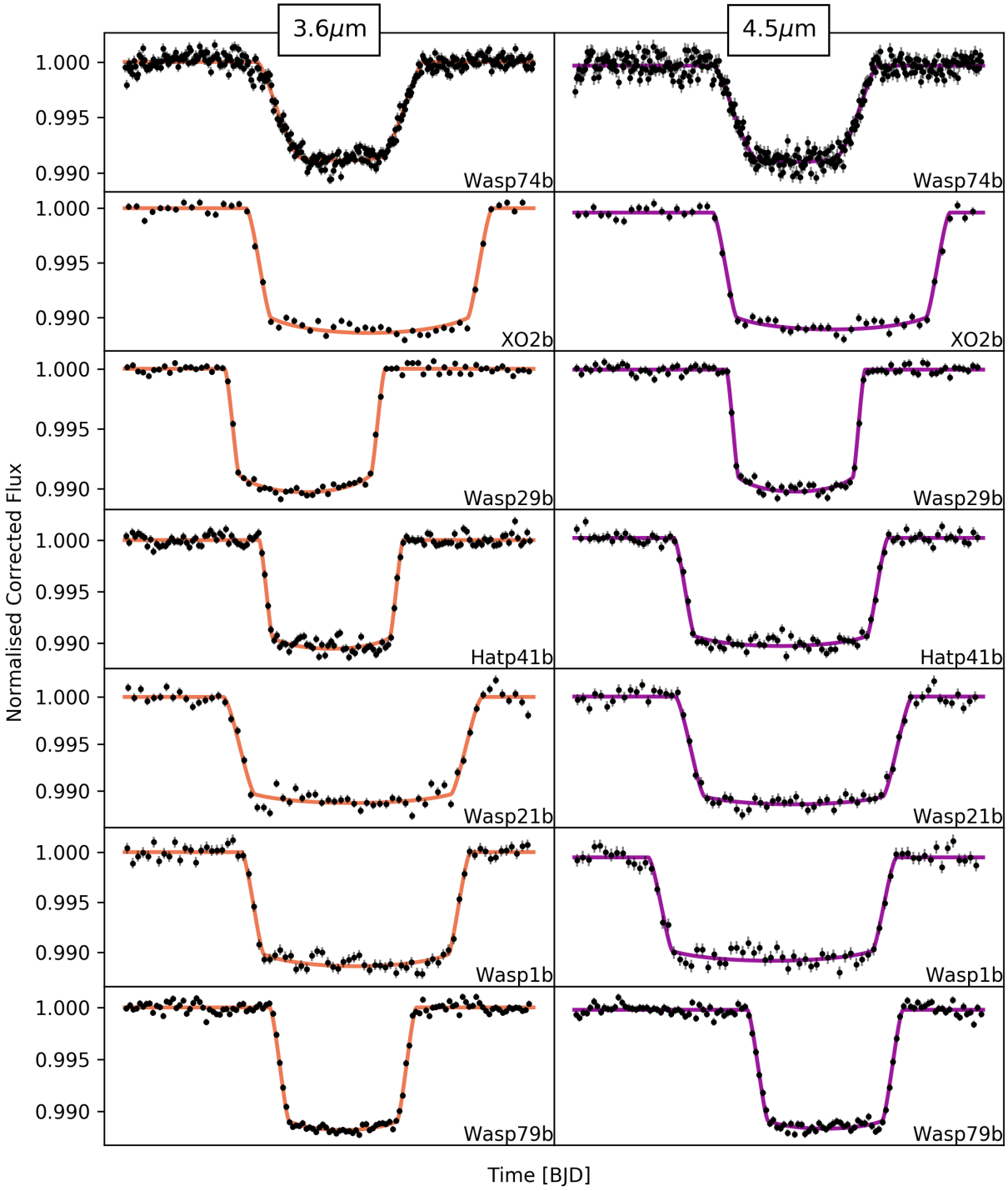


Fig. A.1. continued.

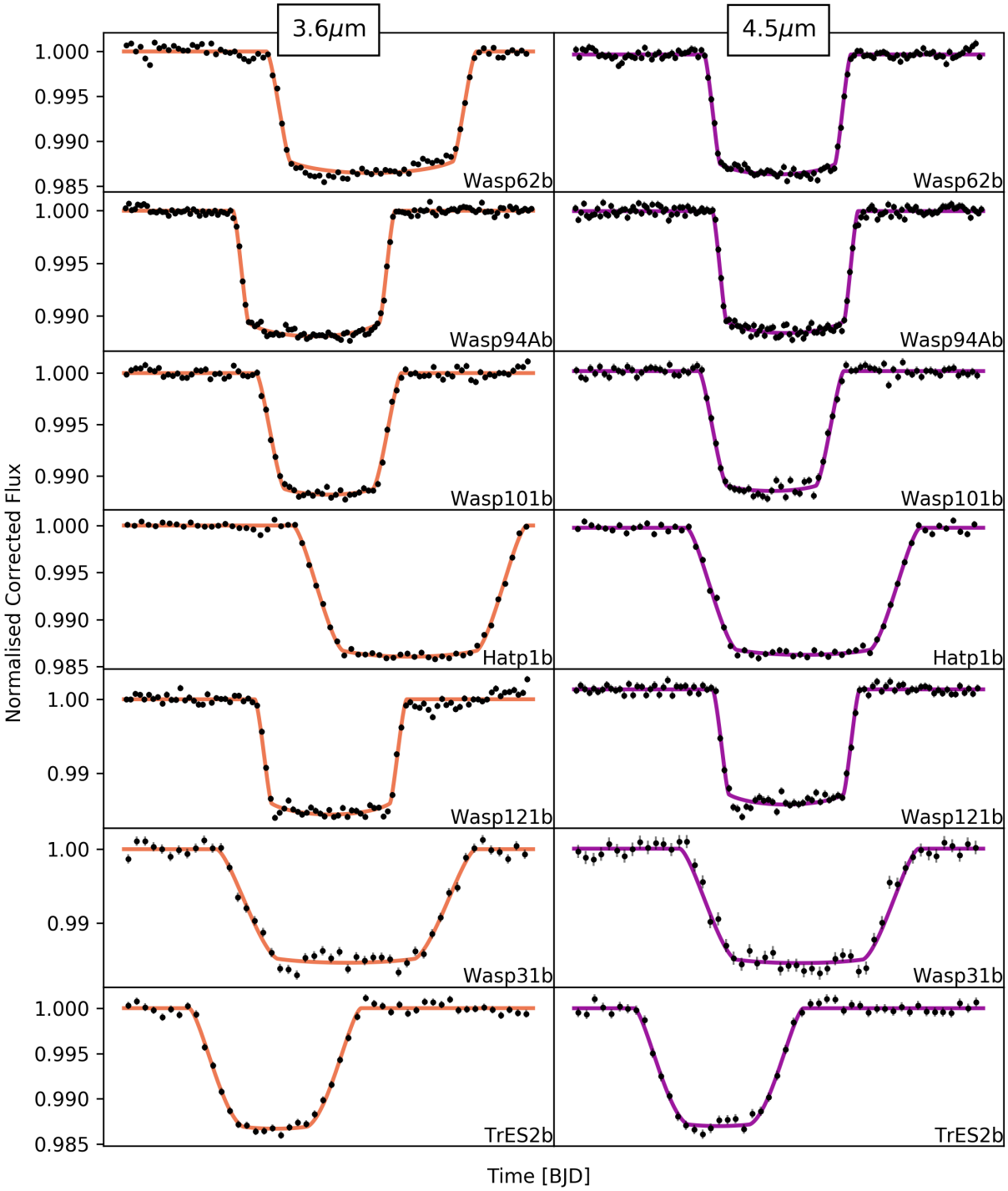


Fig. A.1. continued.

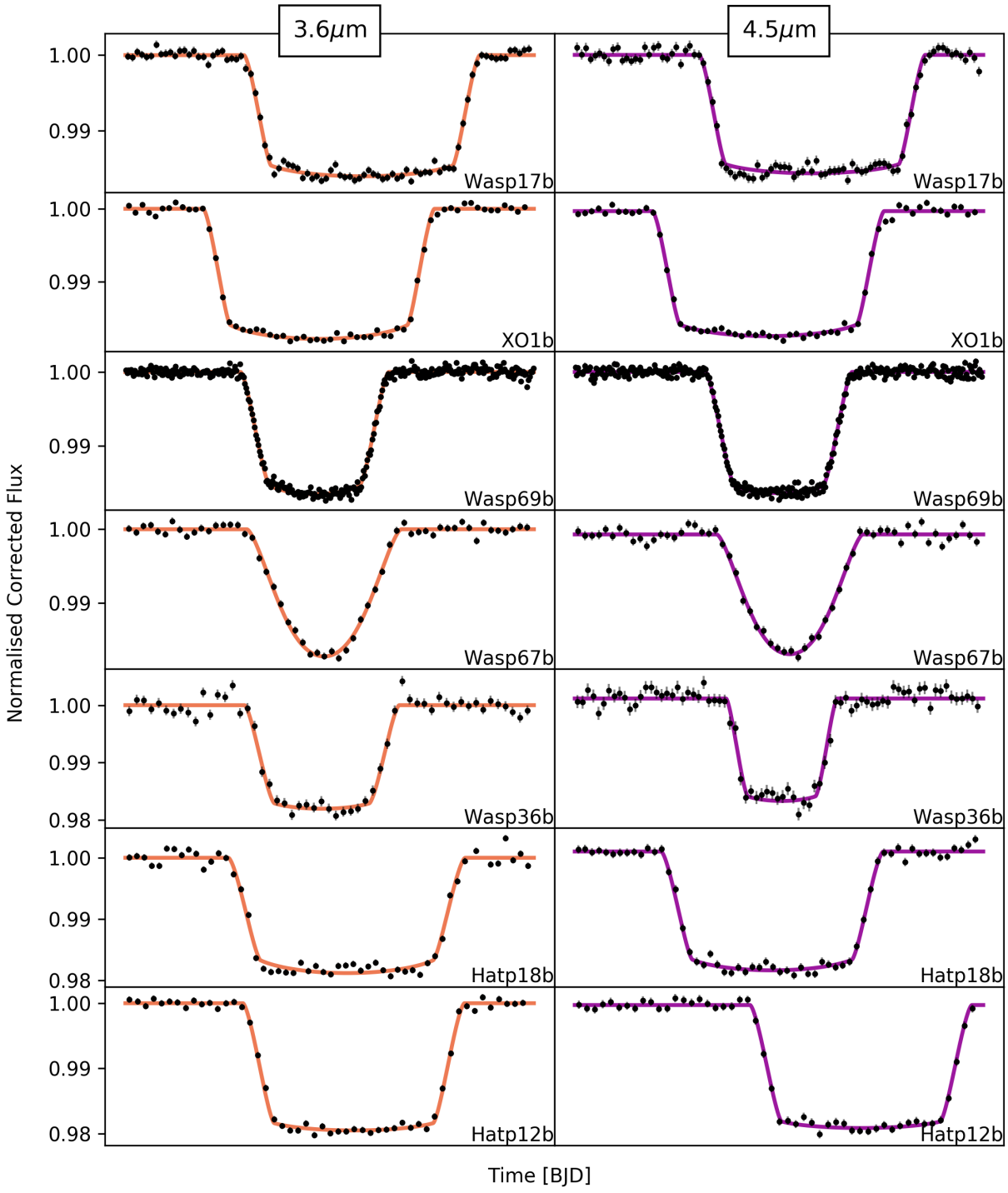


Fig. A.1. continued.

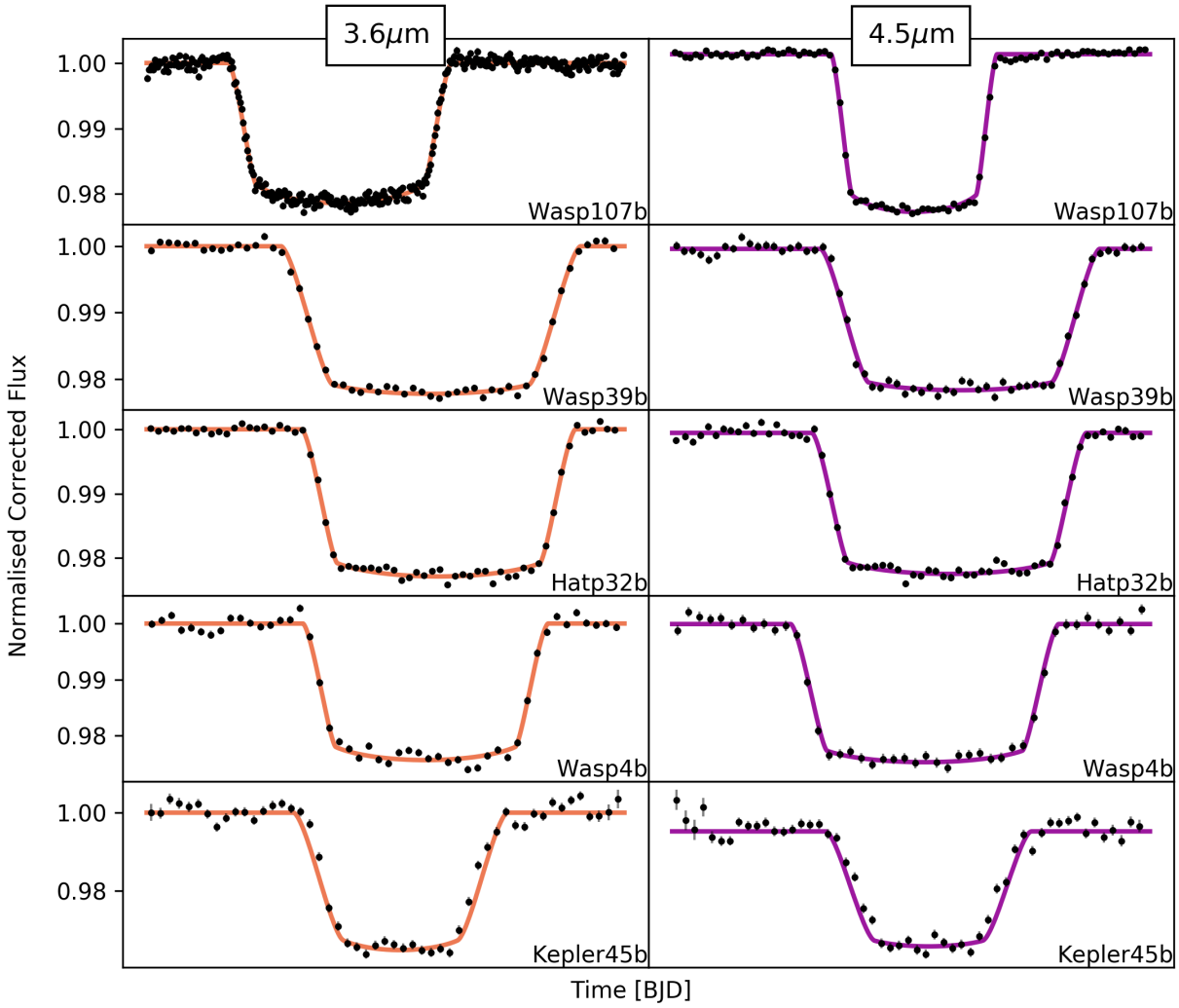


Fig. A.1. continued.

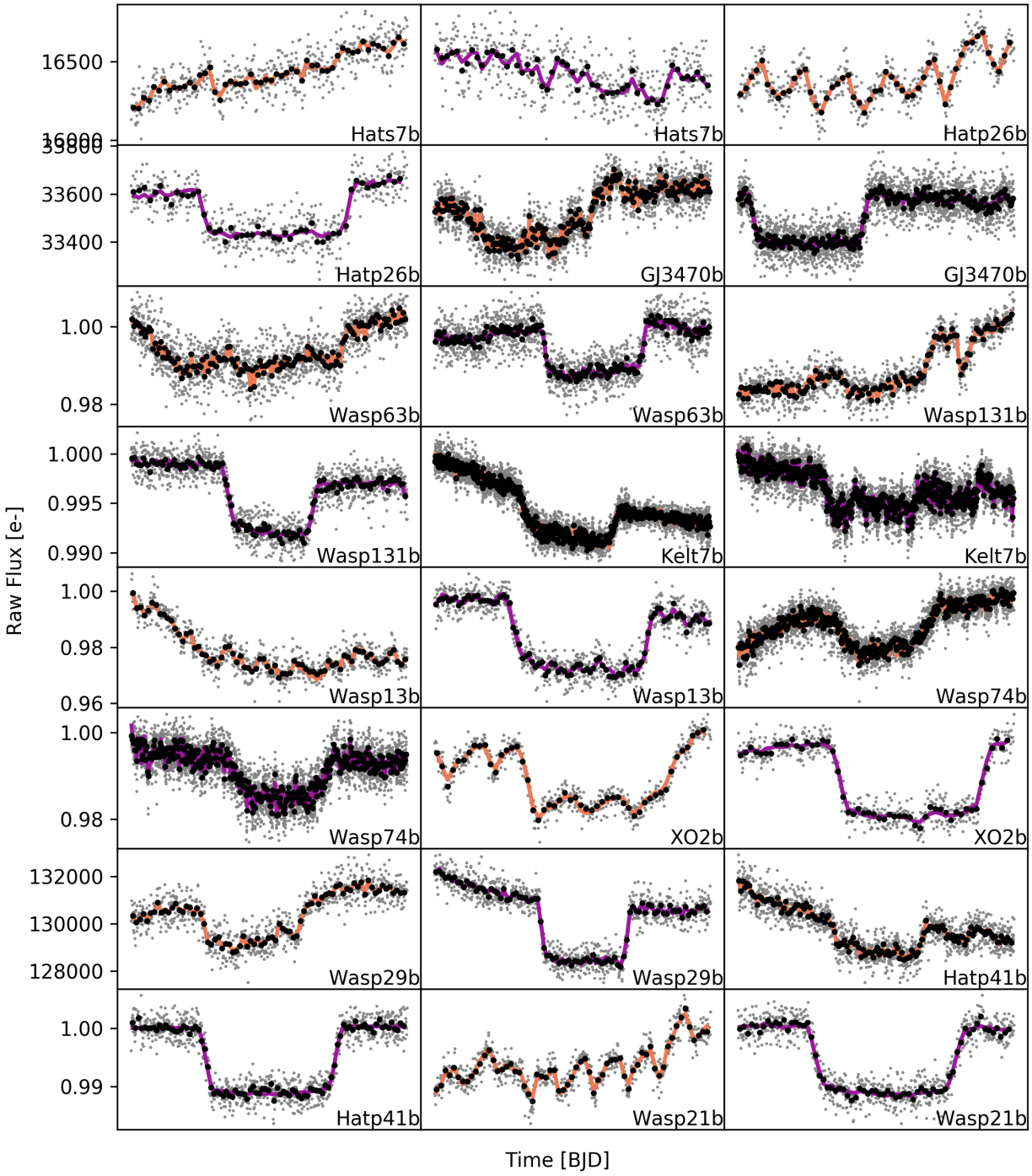


Fig. A.2. Raw light curves for each planet. Flux binned in 5 min is shown in black and 30 s is shown in gray. Colored lines indicate the best-fit instrumental and transit model from our MCMC analysis.

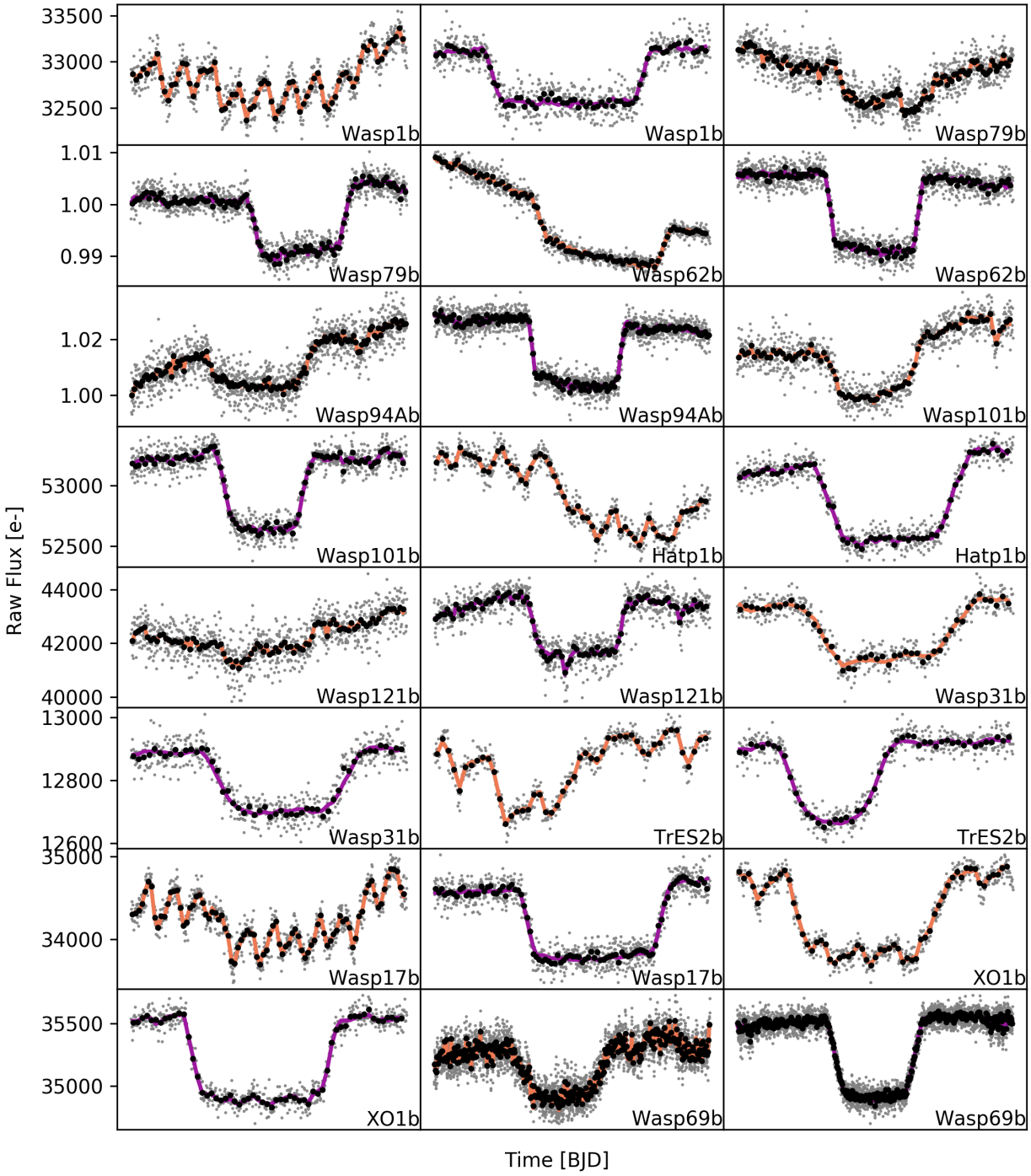


Fig. A.2. continued.

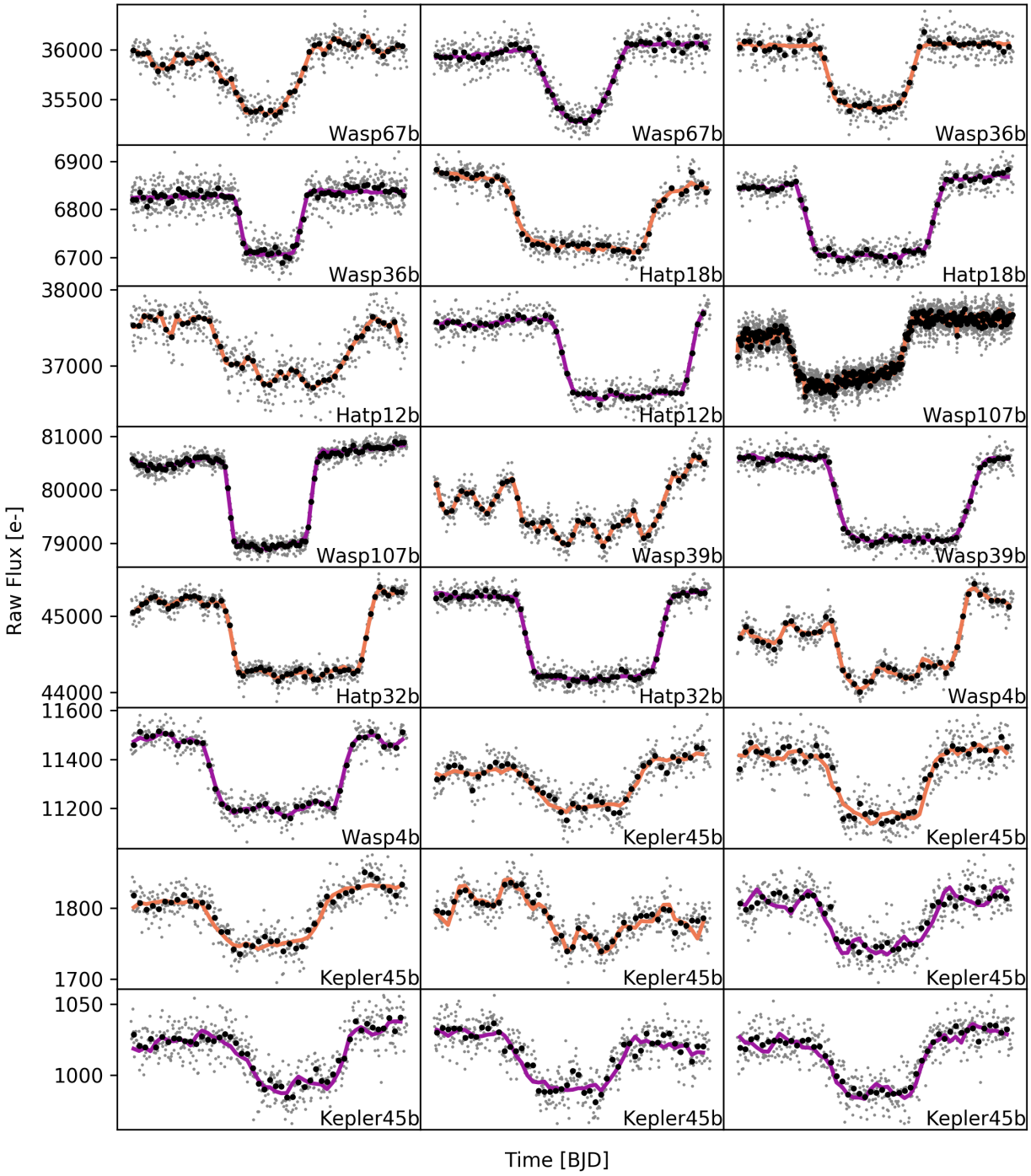


Fig. A.2. continued.

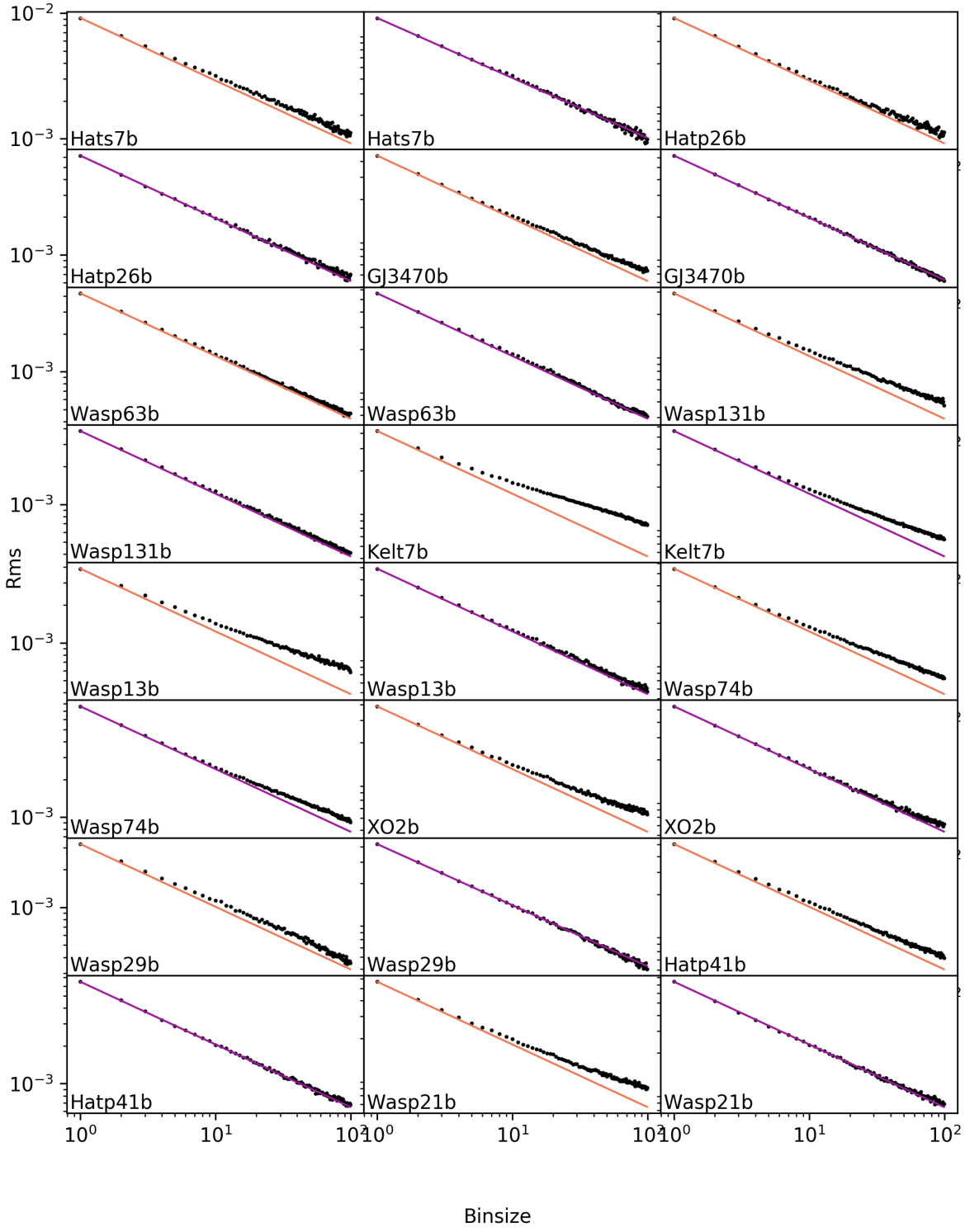


Fig. A.3. RMS vs. normalized bin size of each of the fitted light curves. Straight line is the sqrt(N) theoretical value.

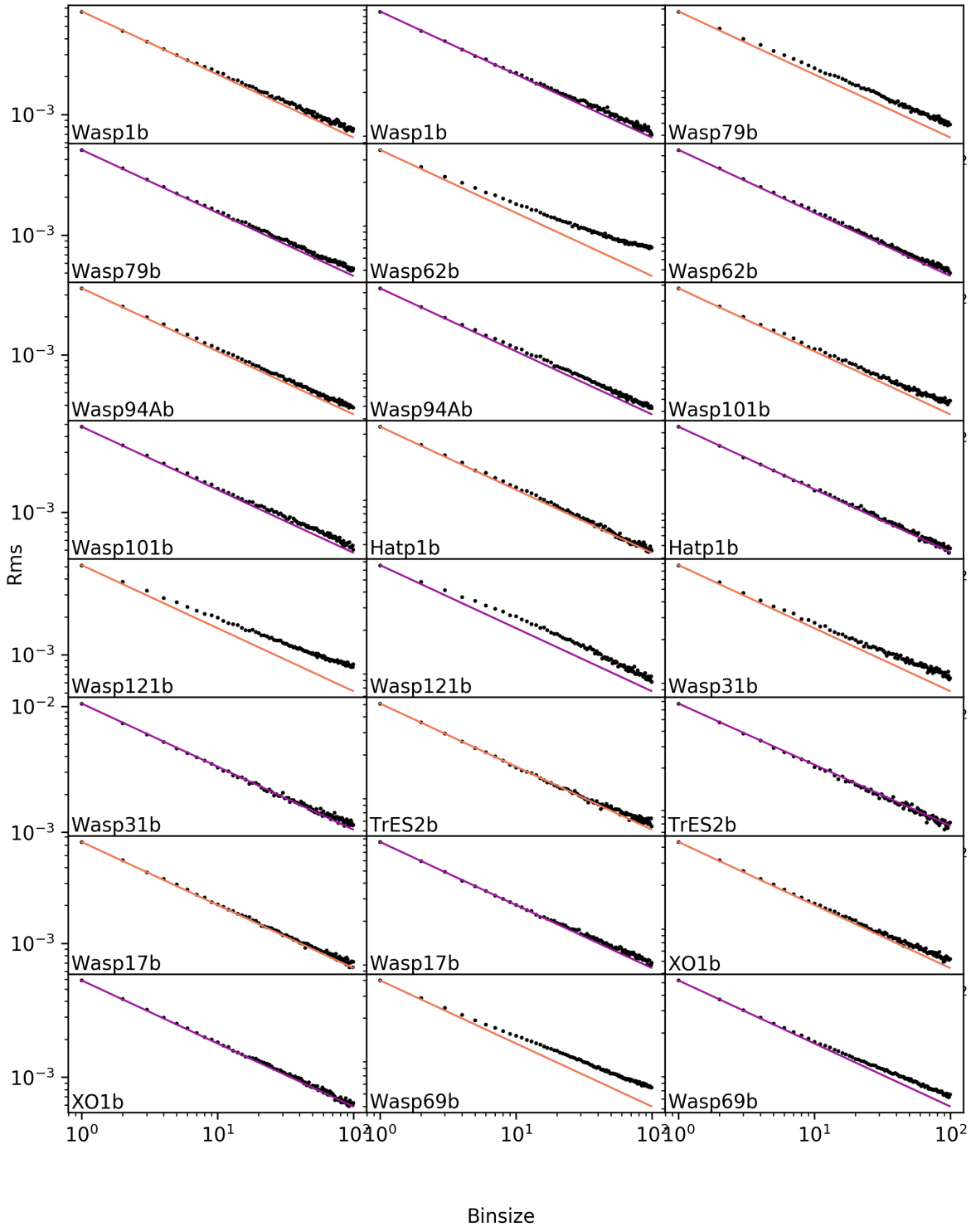


Fig. A.3. continued.

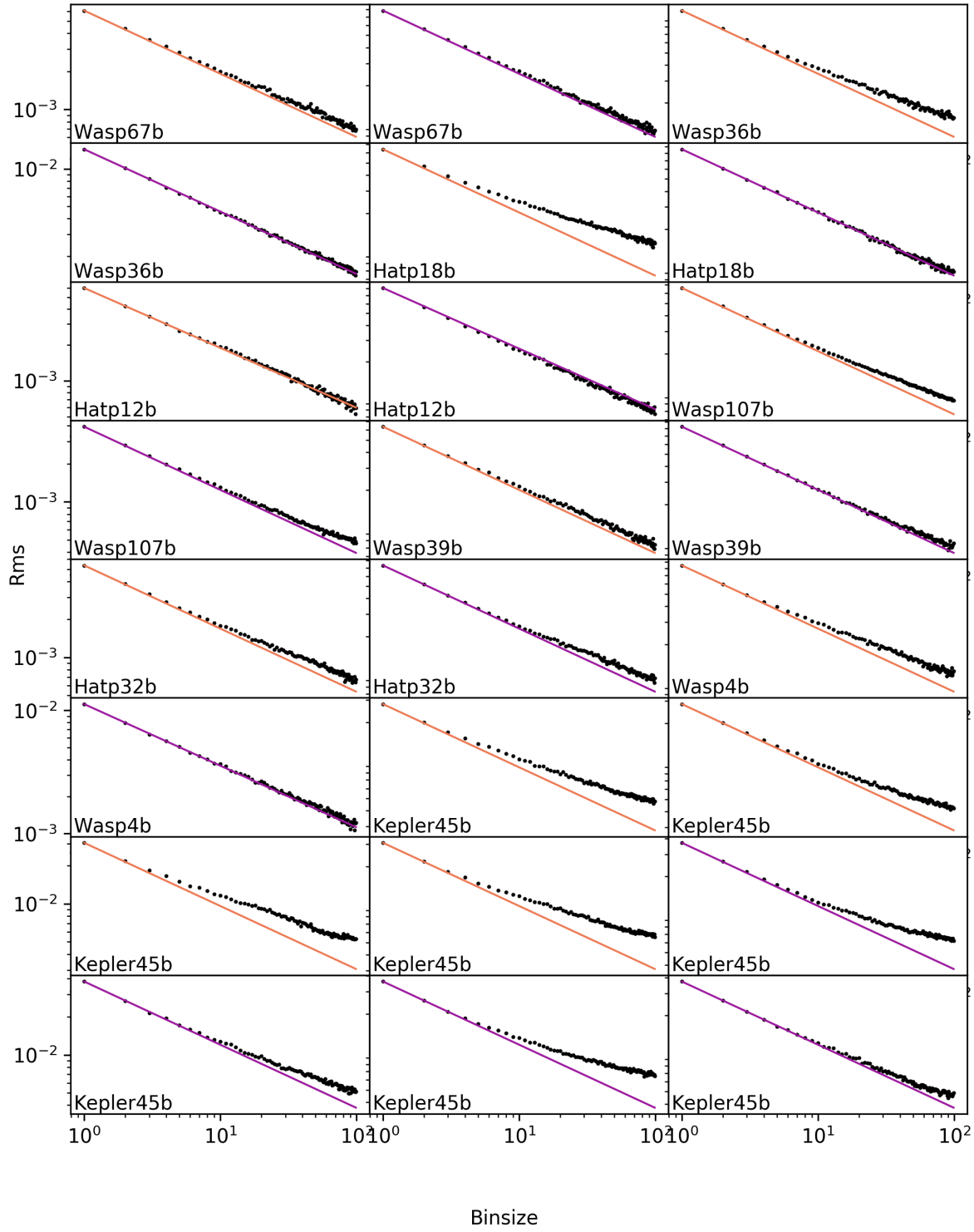


Fig. A.3. continued.

Table A.2. Eclipse depths at 3.6 and 4.5 μm collected from the literature ($(F_p/F_s)_{3.6}$ and $(F_p/F_s)_{4.5}$ respectively).

Planet	$(F_p/F_s)_{3.6}$ ppm	$(F_p/F_s)_{4.5}$ ppm	T_{eq} $(a=0)$ Kelvin	Distance parsec	$M^{pl}_{3.6}$ mag	$M^{pl}_{4.5}$ mag	m^s_{W1} mag	m^s_{W2} mag	color mag	Eclipse reference
HAT-P-32 b	3640 ± 160	4380 ± 200	1901 ± 57	289.2 ± 5.3	8.7 ± 0.1	8.5 ± 0.07	9.9 ± 0.02	9.91 ± 0.02	0.2 ± 0.09	1
XO-1 b	860 ± 70	1220 ± 90	1207 ± 30	163.6 ± 0.6	11.1 ± 0.1	10.73 ± 0.08	9.49 ± 0.02	9.52 ± 0.02	0.36 ± 0.12	2
HAT-P-1 b	800 ± 80	1350 ± 220	1306 ± 33	159.0 ± 1.0	10.5 ± 0.1	9.92 ± 0.18	8.73 ± 0.02	8.75 ± 0.02	0.55 ± 0.21	3
WASP-39 b	880 ± 150	960 ± 180	1118 ± 35	214.0 ± 1.7	11.1 ± 0.2	11.12 ± 0.21	10.16 ± 0.02	10.22 ± 0.02	0.03 ± 0.28	4
HAT-P-12 b	660 ± 270	640 ± 180	958 ± 18	142.8 ± 0.5	12.3 ± 0.4	12.35 ± 0.31	10.08 ± 0.02	10.14 ± 0.02	−0.1 ± 0.54	5
HAT-P-18 b	437 ± 145	326 ± 146	847 ± 26	161.4 ± 0.6	12.6 ± 0.4	12.93 ± 0.49	10.2 ± 0.02	10.25 ± 0.02	−0.38 ± 0.61	6
TrES2 b	1270 ± 210	2300 ± 240	1498 ± 32	215.3 ± 1.0	10.4 ± 0.2	9.72 ± 0.12	9.78 ± 0.02	9.79 ± 0.02	0.63 ± 0.21	7
WASP-4 b	3190 ± 310	3430 ± 270	1651 ± 27	267.2 ± 3.7	9.8 ± 0.1	9.78 ± 0.09	10.68 ± 0.02	10.75 ± 0.02	0.01 ± 0.15	8
XO-2 b	810 ± 170	980 ± 200	1322 ± 23	154.3 ± 1.4	11.0 ± 0.2	10.89 ± 0.22	9.24 ± 0.02	9.31 ± 0.02	0.14 ± 0.32	9
GJ3470 b	113 ± 24	3 ± 22	662 ± 45	29.4 ± 0.1	15.3 ± 0.2	19.25 ± 7.96	7.81 ± 0.03	7.78 ± 0.02	−3.92 ± 7.97	10
WASP-1 b	1170 ± 160	2120 ± 210	1876 ± 69	393.1 ± 10.5	9.6 ± 0.2	8.96 ± 0.12	10.22 ± 0.02	10.25 ± 0.02	0.62 ± 0.2	11
HAT-P-26 b	85 ± 0	265 ± 70	994 ± 48	141.8 ± 1.1	14.0 ± 0.0	12.78 ± 0.29	9.54 ± 0.02	9.6 ± 0.02	1.17 ± 0.29	6
WASP-121 b	3685 ± 114	4684 ± 121	2359 ± 61	269.9 ± 1.6	8.3 ± 0.0	8.05 ± 0.04	9.36 ± 0.02	9.39 ± 0.02	0.23 ± 0.06	12
WASP-87 b	2080 ± 127	2708 ± 137	2343 ± 68	298.4 ± 3.6	8.7 ± 0.1	8.47 ± 0.06	9.4 ± 0.02	9.43 ± 0.02	0.26 ± 0.1	12
WASP-100 b	1267 ± 98	1720 ± 119	2200.pm 171	364.4 ± 2.7	9.1 ± 0.1	8.74 ± 0.08	9.62 ± 0.02	9.64 ± 0.02	0.31 ± 0.12	12
WASP-78 b	2001 ± 218	2013 ± 351	1957.pm 256	754.3 ± 16.7	8.3 ± 0.1	8.33 ± 0.2	10.96 ± 0.02	10.98 ± 0.02	−0.01 ± 0.24	12
HAT-P-41 b	1842 ± 319	2303 ± 177	1937 ± 44	348.2 ± 4.5	8.7 ± 0.2	8.49 ± 0.09	9.56 ± 0.02	9.6 ± 0.02	0.2 ± 0.21	12
WASP-101 b	1161 ± 111	1194 ± 113	1554 ± 40	201.2 ± 1.1	9.9 ± 0.1	9.86 ± 0.11	9.04 ± 0.02	9.07 ± 0.02	0.0 ± 0.15	12
WASP-131 b	304 ± 96	289 ± 80	1458 ± 35	200.1 ± 2.6	10.8 ± 0.3	10.91 ± 0.3	8.54 ± 0.02	8.57 ± 0.02	−0.08 ± 0.46	12
WASP-36 b	914 ± 578	1953 ± 544	1722 ± 45	386.3 ± 5.2	10.8 ± 0.7	10.04 ± 0.3	11.15 ± 0.02	11.2 ± 0.02	0.77 ± 0.75	12
WASP-63 b	486 ± 96	560 ± 130	1531 ± 45	290.7 ± 2.0	10.3 ± 0.2	10.2 ± 0.25	9.34 ± 0.02	9.39 ± 0.02	0.11 ± 0.33	12
WASP-94 A b	867 ± 59	995 ± 93	1500 ± 76	211.2 ± 2.5	9.8 ± 0.1	9.72 ± 0.11	8.8 ± 0.02	8.84 ± 0.02	0.11 ± 0.13	12
WASP-62 b	1616 ± 146	1359 ± 130	1427 ± 35	175.6 ± 0.6	9.7 ± 0.1	9.86 ± 0.11	8.9 ± 0.02	8.92 ± 0.02	−0.21 ± 0.15	12
CoRoT-1 b	4150 ± 420	4820 ± 420	1900 ± 81	787.9 ± 23.5	8.6 ± 0.1	8.45 ± 0.12	12.1 ± 0.02	12.14 ± 0.02	0.12 ± 0.17	13
CoRoT-2 b	3550 ± 200	5000 ± 200	1537 ± 40	213.3 ± 2.5	9.5 ± 0.1	9.21 ± 0.05	10.06 ± 0.02	10.1 ± 0.02	0.34 ± 0.09	13
GJ 436 b	155 ± 22	34 ± 20	649 ± 59	9.8 ± 0.0	15.6 ± 0.2	16.92 ± 0.64	6.02 ± 0.11	5.69 ± 0.05	−1.32 ± 0.67	14
HAT-P-19 b	620 ± 140	620 ± 140	1009 ± 40	202.1 ± 1.5	12.0 ± 0.2	12.05 ± 0.25	10.5 ± 0.02	10.56 ± 0.02	−0.06 ± 0.35	4
HAT-P-2 b	996 ± 72	1031 ± 61	1540 ± 30	127.8 ± 0.4	9.5 ± 0.1	9.52 ± 0.07	7.57 ± 0.02	7.58 ± 0.02	0.03 ± 0.11	15
HAT-P-20 b	615 ± 82	1096 ± 77	971 ± 24	71.0 ± 0.2	12.3 ± 0.1	11.79 ± 0.08	8.56 ± 0.03	8.65 ± 0.02	0.54 ± 0.17	16
HAT-P-23 b	2480 ± 190	3090 ± 260	2051 ± 71	364.8 ± 4.7	9.5 ± 0.1	9.26 ± 0.1	10.75 ± 0.02	10.79 ± 0.02	0.19 ± 0.13	17
HAT-P-26 b	−27 ± 50	223 ± 81	994 ± 48	141.8 ± 1.1	− ± 2.0	12.97 ± 0.4	9.54 ± 0.02	9.6 ± 0.02	− ± 2.05	6
HAT-P-3 b	1120 ± 225	940 ± 125	1158 ± 34	134.6 ± 0.5	11.1 ± 0.2	11.37 ± 0.15	9.38 ± 0.02	9.45 ± 0.02	−0.26 ± 0.26	5
HAT-P-4 b	1420 ± 160	1220 ± 130	1694 ± 47	320.5 ± 2.8	9.3 ± 0.1	9.52 ± 0.12	9.73 ± 0.02	9.77 ± 0.02	−0.2 ± 0.17	5
HAT-P-6 b	1170 ± 80	1060 ± 60	1673 ± 42	275.4 ± 3.6	9.4 ± 0.1	9.54 ± 0.07	9.29 ± 0.02	9.3 ± 0.02	−0.12 ± 0.11	18
HAT-P-7 b	1560 ± 130	1900 ± 110	2225 ± 41	341.1 ± 2.4	8.6 ± 0.1	8.44 ± 0.07	9.28 ± 0.02	9.3 ± 0.02	0.19 ± 0.12	19
HAT-P-8 b	1310 ± 85	1110 ± 75	1772 ± 48	211.6 ± 1.7	9.5 ± 0.1	9.71 ± 0.08	8.93 ± 0.02	8.95 ± 0.02	−0.2 ± 0.11	18
HD 149026 b	400 ± 30	340 ± 60	1673 ± 65	75.9 ± 0.2	10.9 ± 0.1	11.07 ± 0.19	6.79 ± 0.07	6.8 ± 0.02	−0.19 ± 0.22	20
HD 189733 b	2560 ± 140	2140 ± 200	1200 ± 22	19.8 ± 0.0	10.3 ± 0.2	10.54 ± 0.11	5.29 ± 0.15	5.34 ± 0.05	−0.25 ± 0.2	21
HD 209458 b	1190 ± 70	1230 ± 60	1446 ± 19	48.3 ± 0.1	10.2 ± 0.1	10.05 ± 0.06	6.31 ± 0.09	6.19 ± 0.03	0.15 ± 0.13	22
Kepler-12 b	1370 ± 200	1160 ± 310	1481 ± 31	881.4 ± 9.7	9.5 ± 0.2	9.69 ± 0.29	12.05 ± 0.02	12.08 ± 0.02	−0.21 ± 0.33	23
Kepler-17 b	2500 ± 300	3100 ± 350	1745 ± 39	720.8 ± 10.3	9.8 ± 0.1	9.58 ± 0.13	12.55 ± 0.02	12.59 ± 0.02	0.19 ± 0.19	24
Kepler-5 b	1030 ± 170	1070 ± 150	1807 ± 35	899.8 ± 16.5	9.4 ± 0.2	9.4 ± 0.16	11.68 ± 0.02	11.74 ± 0.02	−0.02 ± 0.24	25
Kepler-6 b	690 ± 270	1510 ± 190	1504 ± 21	587.0 ± 5.0	10.6 ± 0.4	9.85 ± 0.14	11.58 ± 0.02	11.64 ± 0.02	0.79 ± 0.45	26
KOI-13 b	1560 ± 310	2220 ± 230	2607 ± 94	519.1 ± 29.1	7.8 ± 0.2	7.47 ± 0.17	9.39 ± 0.02	9.41 ± 0.02	0.36 ± 0.3	27
Qatar-1 b	1511 ± 455	2907 ± 415	1389 ± 43	185.6 ± 0.8	11.0 ± 0.3	10.39 ± 0.16	10.32 ± 0.02	10.4 ± 0.02	0.64 ± 0.36	28

Notes. T_{eq} is the equilibrium temperature assuming no redistribution and zero albedo. Distance is the estimated distance in parsecs taken from Bailer-Jones et al. (2018). m^s_{W1} and m^s_{W2} are the stellar apparent magnitudes. $M^{pl}_{3.6}$ and $M^{pl}_{4.5}$ and the planetary absolute magnitudes in the wise 1 and wise 2 bandpasses (which are equivalent to the *Spitzer* channel 1 and channel 2 respectively) calculated using the planet-to-star-flux ratio. Color is the 4.5 minus 3.6 micron magnitude color of the planets. The final column details the reference for each of the eclipse depths in the literature, the majority of which were collected from exoplanets.org (Wright et al. 2011) and have been individually verified.

References. (1) Zhao et al. (2014); (2) Machalek et al. (2008); (3) Todorov et al. (2010); (4) Garhart et al. (2020); (5) Kammer et al. (2015); (6) Todorov et al. (2013); (7) Wallack et al. (2019); (8) O'Donovan et al. (2010); (9) Beerer et al. (2011); (10) Machalek et al. (2009); (11) Benneke et al. (2019); (12) Wheatley et al. (2010); (13) Deming et al. (2011); (14) Morley et al. (2017); (15) Lewis et al. (2013); (16) Deming et al. (2015); (17) O'Rourke et al. (2014); (18) Todorov et al. (2012); (19) Christiansen et al. (2010); (20) Stevenson et al. (2012); (21) Charbonneau et al. (2008); (22) Diamond-Lowe et al. (2014); (23) Fortney et al. (2011); (24) Désert et al. (2011b); (25) Désert et al. (2011c); (26) Désert et al. (2011a); (27) Shporer et al. (2014); (28) Garhart et al. (2020); (29) Fressin et al. (2010); (30) Knutson et al. (2009); (31) Kreidberg et al. (2018a); (32) Stevenson et al. (2014); (33) Blecic et al. (2013); (34) Nymeyer et al. (2011); (35) Anderson et al. (2013); (36) Smith et al. (2012); (37) Deming et al. (2012); (38) Blecic et al. (2014); (39) Baskin et al. (2013); (40) Cubillos et al. (2013); (41) Triaud et al. (2015) and (42) Machalek et al. (2010).

Table A.2. continued.

Planet	$(F_p/F_s)_{3.6}$ ppm	$(F_p/F_s)_{4.5}$ ppm	T_{eq} $(a=0)$ Kelvin	Distance parsec	$M^{pl}_{3.6}$ mag	$M^{pl}_{4.5}$ mag	m^s_{W1} mag	m^s_{W2} mag	color mag	Eclipse reference
TrES-3 b	3460 ± 350	3720 ± 540	1629 ± 32	231.3 ± 1.3	9.9 ± 0.1	9.86 ± 0.16	10.57 ± 0.02	10.61 ± 0.02	0.04 ± 0.2	29
TrES-4 b	1370 ± 110	1480 ± 160	1785 ± 41	516.0 ± 6.9	8.8 ± 0.1	8.79 ± 0.12	10.24 ± 0.02	10.28 ± 0.02	0.05 ± 0.15	30
WASP-10 b	1000 ± 110	1460 ± 160	960 ± 24	141.0 ± 0.7	11.7 ± 0.1	11.34 ± 0.12	9.93 ± 0.02	10.0 ± 0.02	0.34 ± 0.17	4
WASP-103 b	4458 ± 383	5686 ± 138	2505 ± 78	883.3 ± 153.1	6.9 ± 0.4	6.63 ± 0.38	10.72 ± 0.02	10.75 ± 0.02	0.24 ± 0.54	31
WASP-12 b	4210 ± 110	4280 ± 120	2584 ± 91	427.2 ± 6.0	7.9 ± 0.0	7.88 ± 0.05	10.11 ± 0.02	10.11 ± 0.02	0.02 ± 0.07	32
WASP-121 b	3150 ± 103	4510 ± 107	2359 ± 61	269.9 ± 1.6	8.5 ± 0.0	8.1 ± 0.03	9.36 ± 0.02	9.39 ± 0.02	0.36 ± 0.06	12
WASP-14 b	1870 ± 70	2240 ± 180	1864 ± 60	162.0 ± 0.8	9.3 ± 0.0	9.17 ± 0.09	8.57 ± 0.02	8.6 ± 0.02	0.17 ± 0.1	33
WASP-18 b	3000 ± 200	3900 ± 200	2398 ± 73	123.5 ± 0.4	8.9 ± 0.1	8.69 ± 0.06	8.07 ± 0.02	8.12 ± 0.02	0.24 ± 0.1	34
WASP-19 b	4830 ± 250	5720 ± 300	2066 ± 46	268.3 ± 1.7	9.1 ± 0.1	8.96 ± 0.06	10.44 ± 0.02	10.49 ± 0.02	0.13 ± 0.09	35
WASP-2 b	830 ± 350	1690 ± 170	1300 ± 71	153.2 ± 1.6	11.4 ± 0.5	10.64 ± 0.11	9.58 ± 0.02	9.64 ± 0.02	0.72 ± 0.47	11
WASP-24 b	1590 ± 130	2020 ± 180	1769 ± 39	322.1 ± 4.4	9.6 ± 0.1	9.33 ± 0.1	10.1 ± 0.02	10.13 ± 0.02	0.23 ± 0.14	36
WASP-33 b	2600 ± 500	4100 ± 200	2694 ± 53	121.9 ± 1.0	8.4 ± 0.2	7.98 ± 0.06	7.38 ± 0.04	7.44 ± 0.02	0.43 ± 0.22	37
WASP-43 b	3460 ± 130	3820 ± 150	1375 ± 79	86.7 ± 0.3	10.6 ± 0.0	10.58 ± 0.05	9.15 ± 0.02	9.22 ± 0.02	0.03 ± 0.07	38
WASP-48 b	1760 ± 130	2140 ± 200	2033 ± 68	454.1 ± 4.4	8.9 ± 0.1	8.76 ± 0.11	10.33 ± 0.02	10.37 ± 0.02	0.17 ± 0.14	17
WASP-5 b	1970 ± 280	2370 ± 240	1742 ± 68	309.1 ± 3.4	9.9 ± 0.2	9.7 ± 0.11	10.54 ± 0.02	10.59 ± 0.02	0.15 ± 0.19	39
WASP-6 b	940 ± 190	1150 ± 220	1184 ± 32	197.1 ± 1.6	11.4 ± 0.2	11.21 ± 0.21	10.28 ± 0.02	10.34 ± 0.02	0.16 ± 0.3	4
WASP-67 b	220 ± 130	800 ± 180	1028 ± 32	189.5 ± 1.5	12.8 ± 0.6	11.43 ± 0.25	10.03 ± 0.02	10.08 ± 0.02	1.35 ± 0.69	4
WASP-69 b	421 ± 29	463 ± 39	961 ± 21	50.0 ± 0.1	12.3 ± 0.1	12.28 ± 0.09	7.32 ± 0.04	7.44 ± 0.02	−0.02 ± 0.13	6
WASP-8 b	1130 ± 180	690 ± 70	927 ± 27	90.0 ± 0.4	10.5 ± 0.2	11.05 ± 0.11	7.91 ± 0.02	7.92 ± 0.02	−0.55 ± 0.21	40
WASP-80 b	455 ± 100	944 ± 65	775 ± 25	49.8 ± 0.1	13.2 ± 0.2	12.4 ± 0.08	8.3 ± 0.02	8.32 ± 0.02	0.77 ± 0.25	41
XO-3 b	1010 ± 40	1580 ± 36	2046 ± 40	213.1 ± 2.7	9.6 ± 0.1	9.13 ± 0.04	8.75 ± 0.02	8.76 ± 0.02	0.47 ± 0.07	42
XO-4 b	560 ± 90	1350 ± 85	1639 ± 35	272.7 ± 2.9	10.3 ± 0.2	9.39 ± 0.08	9.37 ± 0.02	9.4 ± 0.02	0.93 ± 0.19	18
HAT-P-13 b	851 ± 107	1090 ± 124	1648 ± 53	246.8 ± 2.2	7.2 ± 0.1	6.95 ± 0.13	8.96 ± 0.02	9.01 ± 0.02	0.22 ± 0.19	12
HAT-P-30 b	1603 ± 107	1783 ± 147	1637 ± 43	214.0 ± 2.2	6.9 ± 0.1	6.8 ± 0.09	9.04 ± 0.02	9.08 ± 0.02	0.08 ± 0.12	12
HAT-P-33 b	1663 ± 127	1896 ± 199	1780 ± 34	396.1 ± 7.5	6.5 ± 0.1	6.33 ± 0.12	10.0 ± 0.02	10.02 ± 0.02	0.13 ± 0.16	12
HAT-P-40 b	988 ± 168	1057 ± 145	1765 ± 66	464.5 ± 6.4	6.7 ± 0.2	6.62 ± 0.15	9.98 ± 0.02	10.01 ± 0.02	0.04 ± 0.24	12
KELT-2 A b	739 ± 38	761 ± 47	1710 ± 31	134.1 ± 0.8	7.0 ± 0.1	6.99 ± 0.07	7.27 ± 0.04	7.34 ± 0.02	−0.03 ± 0.1	12
KELT-3 b	1788 ± 97	1677 ± 104	1822 ± 44	210.3 ± 5.4	6.3 ± 0.1	6.43 ± 0.09	8.57 ± 0.02	8.6 ± 0.02	−0.1 ± 0.12	12
WASP-104 b	1709 ± 195	2643 ± 303	1516 ± 43	185.9 ± 1.5	7.9 ± 0.1	7.5 ± 0.13	9.84 ± 0.02	9.91 ± 0.02	0.41 ± 0.18	12
WASP-46 b	1360 ± 701	4446 ± 589	1658 ± 55	375.3 ± 4.4	8.1 ± 0.6	6.88 ± 0.15	11.35 ± 0.02	11.37 ± 0.02	1.27 ± 0.58	12
WASP-64 b	2859 ± 270	2071 ± 471	1690 ± 52	369.9 ± 3.0	7.0 ± 0.1	7.38 ± 0.25	10.96 ± 0.02	11.01 ± 0.02	−0.4 ± 0.27	12
WASP-65 b	1587 ± 245	724 ± 318	1485 ± 59	273.7 ± 2.7	7.6 ± 0.2	8.52 ± 0.48	10.31 ± 0.02	10.35 ± 0.02	−0.9 ± 0.51	12
WASP-76 b	2979 ± 63	3762 ± 82	2183 ± 47	194.5 ± 6.0	5.6 ± 0.1	5.35 ± 0.07	8.19 ± 0.02	8.23 ± 0.02	0.22 ± 0.1	12
WASP-77 A b	2016 ± 94	2487 ± 127	1671 ± 31	105.2 ± 1.2	7.2 ± 0.1	7.06 ± 0.06	8.11 ± 0.02	8.16 ± 0.02	0.17 ± 0.09	12
WASP-97 b	1359 ± 84	1534 ± 101	1540 ± 42	151.1 ± 0.5	7.7 ± 0.1	7.65 ± 0.07	8.96 ± 0.02	9.01 ± 0.02	0.08 ± 0.1	12
WASP-74 b	1446 ± 66	2075 ± 100	1923 ± 53	149.2 ± 1.1	9.4 ± 0.1	9.03 ± 0.06	8.14 ± 0.02	8.19 ± 0.02	0.34 ± 0.08	12
KELT-7 b	1688 ± 46	1896 ± 57	2050 ± 35	136.7 ± 0.9	8.7 ± 0.0	8.65 ± 0.04	7.5 ± 0.03	7.52 ± 0.02	0.1 ± 0.06	12
WASP-79 b	1394 ± 88	1783 ± 106	1762 ± 53	246.7 ± 1.8	9.2 ± 0.1	8.96 ± 0.07	9.03 ± 0.02	9.04 ± 0.02	0.25 ± 0.1	12

Table A.3. Optimum parameters used for our pipeline which minimise the χ^2 of a least-squares fit to the systematic errors and the transit.

Planet	Channel	Aperture size pixels	Background method	Background params pixels	Centroiding method	Centroiding params pixels
HAT-P-32 b	ch1	2.50	Annulus	–, 6, 4	Barycenter	3.0
HAT-P-32 b	ch2	2.50	Annulus	–, 6, 4	Barycenter	5.0
XO-1 b	ch1	2.50	Annulus	–, 6, 4	Moffat	–
XO-1 b	ch2	2.50	Annulus	–, 6, 4	Gaussian	–
HAT-P-1 b	ch1	3.00	Box	4, –, –	Barycenter	5.0
HAT-P-1 b	ch2	3.50	Box	4, –, –	Barycenter	5.0
WASP-17 b	ch1	2.50	Annulus	–, 6, 4	Barycenter	5.0
WASP-17 b	ch2	2.50	Annulus	–, 6, 4	Barycenter	3.0
WASP-39 b	ch1	2.50	Annulus	–, 6, 4	Barycenter	3.0
WASP-39 b	ch2	2.50	Annulus	–, 6, 4	Barycenter	7.0
HAT-P-12 b	ch1	2.50	Annulus	–, 6, 4	Moffat	–
HAT-P-12 b	ch2	2.50	Annulus	–, 6, 4	Moffat	–
HAT-P-18 b	ch1	2.50	Annulus	–, 6, 4	Barycenter	5.0
HAT-P-18 b	ch2	2.50	Annulus	–, 6, 4	Moffat	–
TrES-2 b	ch1	2.50	Annulus	–, 6, 4	Barycenter	5.0
TrES-2 b	ch2	2.50	Histogram	–, –, –	Barycenter	3.0
WASP-4 b	ch1	2.50	Annulus	–, 6, 4	Moffat	–
WASP-4 b	ch2	2.50	Annulus	–, 6, 4	Barycenter	5.0
XO-2 b	ch1	2.50	Annulus	–, 6, 4	Moffat	–
XO-2 b	ch2	2.50	Annulus	–, 6, 4	Barycenter	7.0
GJ3470 b	ch1	2.50	Annulus	–, 6, 4	Barycenter	3.0
GJ3470 b	ch2	2.50	Annulus	–, 6, 4	Barycenter	3.0
WASP-21 b	ch1	2.50	Annulus	–, 6, 4	Barycenter	5.0
WASP-21 b	ch2	2.50	Annulus	–, 6, 4	Barycenter	5.0
WASP-31 b	ch1	2.50	Annulus	–, 6, 4	Barycenter	7.0
WASP-31 b	ch2	2.50	Annulus	–, 6, 4	Barycenter	7.0
WASP-1 b	ch1	2.50	Annulus	–, 6, 4	Barycenter	7.0
WASP-1 b	ch2	2.50	Annulus	–, 6, 4	Barycenter	3.0
HAT-P-26 b	ch1	2.50	Annulus	–, 6, 4	Barycenter	7.0
HAT-P-26 b	ch2	2.50	Annulus	–, 6, 4	Barycenter	5.0
WASP-107 b	ch1	2.25	Histogram	–, –, –	Barycenter	5.0
WASP-107 b	ch2	2.25	Histogram	–, –, –	Barycenter	3.0
WASP-13 b	ch1	2.25	Histogram	–, –, –	Gaussian	–
WASP-13 b	ch2	2.50	Histogram	–, –, –	Barycenter	3.0
WASP-121 b	ch1	1.00	Histogram	–, –, –	Barycenter	3.0
WASP-121 b	ch2	1.00	Box	4, –, –	Barycenter	3.0
WASP-69 b	ch1	2.00	Histogram	–, –, –	Gaussian	–
WASP-69 b	ch2	2.25	Histogram	–, –, –	Barycenter	3.0
WASP-67 b	ch1	2.00	Histogram	–, –, –	Moffat	–
WASP-67 b	ch2	2.00	Histogram	–, –, –	Moffat	–
HATS-7 b	ch1	2.00	Histogram	–, –, –	Barycenter	3.0
HATS-7 b	ch2	2.00	Histogram	–, –, –	Gaussian	–
WASP-29 b	ch1	2.25	Histogram	–, –, –	Gaussian	–
WASP-29 b	ch2	2.25	Histogram	–, –, –	Barycenter	3.0
HAT-P-41 b	ch1	2.25	Histogram	–, –, –	Barycenter	3.0
HAT-P-41 b	ch2	2.25	Histogram	–, –, –	Gaussian	–
WASP-101 b	ch1	2.25	Histogram	–, –, –	Barycenter	5.0
WASP-101 b	ch2	2.25	Histogram	–, –, –	Barycenter	3.0
WASP-131 b	ch1	2.25	Histogram	–, –, –	Barycenter	5.0
WASP-131 b	ch2	2.25	Histogram	–, –, –	Barycenter	3.0
WASP-36 b	ch1	2.00	Histogram	–, –, –	Gaussian	–
WASP-36 b	ch2	2.00	Histogram	–, –, –	Barycenter	3.0
WASP-63 b	ch1	2.25	Histogram	–, –, –	Barycenter	5.0
WASP-63 b	ch2	2.25	Histogram	–, –, –	Gaussian	–

Notes. If background method is "Annulus", then the two parameters are the radius and width of a circular annulus; if it is "box" then the parameter is the size of the box taken in all of the four corners of the image. If the centroiding method is "baycenter" then the parameter is the number of pixels over which to create a box over the star for the flux weighting.

Table A.3. continued.

Planet	Channel	Aperture size pixels	Background method	Background params pixels	Centroiding method	Centroiding params pixels
WASP-79 b	ch1	2.50	Histogram	-, -, -	Barycenter	5.0
WASP-79 b	ch2	2.25	Histogram	-, -, -	Barycenter	3.0
WASP-94 Ab	ch1	2.50	Histogram	-, -, -	Moffat	–
WASP-94 Ab	ch2	2.25	Histogram	-, -, -	Barycenter	3.0
WASP-74 b	ch1	2.25	Histogram	-, -, -	Barycenter	3.0
WASP-74 b	ch2	2.00	Histogram	-, -, -	Barycenter	3.0
WASP-62 b	ch1	2.25	Histogram	-, -, -	Barycenter	3.0
WASP-62 b	ch2	2.25	Box	4, -, -	Barycenter	3.0
KELT-7 b	ch1	2.25	Histogram	-, -, -	Moffat	–
KELT-7 b	ch2	2.00	Histogram	-, -, -	Barycenter	3.0
Kepler-45 b	ch1	1.00	Histogram	-, -, -	Barycenter	3.0
Kepler-45 b	ch1	1.00	Histogram	-, -, -	Gaussian	–
Kepler-45 b	ch1	1.00	Histogram	-, -, -	Gaussian	–
Kepler-45 b	ch1	1.00	Histogram	-, -, -	Gaussian	–
Kepler-45 b	ch2	1.00	Histogram	-, -, -	Gaussian	–
Kepler-45 b	ch2	1.00	Histogram	-, -, -	Barycenter	3.0
Kepler-45 b	ch2	1.00	Histogram	-, -, -	Moffat	–
Kepler-45 b	ch2	1.00	Box	2, -, -	Gaussian	–

Table A.4. Statistical tests outputted by our custom-built pipeline.

Planet	λ (μm)	Vary ld 3σ	Bad pix %	Cut time (min)	Photon noise %	MCMC acceptance fraction
HAT-P-32 b	3.6	0.804	0.306	0.0	1.31	0.384
HAT-P-32 b	4.5	0.603	0.056	0.0	1.32	0.383
XO-1 b	3.6	0.442	0.113	10.0	1.31	0.384
XO-1 b	4.5	0.194	0.061	10.0	1.23	0.385
HAT-P-1 b	3.6	0.018	0.270	10.0	1.47	0.386
HAT-P-1 b	4.5	0.035	0.052	10.0	1.34	0.385
WASP-17 b	3.6	0.198	0.309	50.0	1.41	0.385
WASP-17 b	4.5	0.106	0.058	30.0	1.37	0.386
WASP-39 b	3.6	1.188	0.294	20.0	1.39	0.382
WASP-39 b	4.5	0.416	0.062	0.0	1.32	0.381
HAT-P-12 b	3.6	0.387	0.289	10.0	1.35	0.382
HAT-P-12 b	4.5	0.273	0.062	10.0	1.34	0.383
HAT-P-18 b	3.6	0.382	0.243	20.0	1.47	0.382
HAT-P-18 b	4.5	0.183	0.067	0.0	1.34	0.385
TrES2 b	3.6	0.332	0.275	10.0	1.33	0.383
TrES2 b	4.5	0.193	0.069	5.0	1.26	0.385
WASP-4 b	3.6	1.424	0.295	10.0	1.53	0.384
WASP-4 b	4.5	0.771	0.049	30.0	1.48	0.385
XO-2 b	3.6	0.156	0.250	30.0	1.27	0.385
XO-2 b	4.5	0.052	0.048	20.0	1.24	0.383
GJ3470 b	3.6	0.523	0.007	5.0	1.22	0.382
GJ3470 b	4.5	0.246	0.006	5.0	1.28	0.383
WASP-21 b	3.6	0.029	0.242	40.0	1.39	0.383
WASP-21 b	4.5	0.020	0.070	10.0	1.32	0.383
WASP-31 b	3.6	0.034	0.317	30.0	1.46	0.383
WASP-31 b	4.5	0.037	0.055	10.0	1.43	0.383

Notes. We measure the strength of the dependence on the chosen limb-darkening parameters by varying them within 3σ of their error for 500 iterations. For each iteration we perform a least-squares fit and measure the variation on the measured R_p/R_s as a function of the final calculated error on R_p/R_s. 'Bad pix' is the number of bad pixels corrected at the beginning of the analysis. Cut time (min) is the number of minutes cut from the beginning of each observation; this value is chosen such that we keep as much baseline as possible while minimizing the chi2 of the different possible baselines. Photon noise is the percentage above pure statistical noise we have for each light curve; typical values for *Spitzer* are 30–60% above photon noise.

Table A.4. continued.

Planet	λ (μm)	Vary ld 3σ	Bad pix %	Cut time (min)	Photon noise %	MCMC acceptance fraction
WASP-1 b	3.6	0.742	0.331	10.0	1.43	0.384
WASP-1 b	4.5	0.490	0.055	40.0	1.39	0.387
HAT-P-26 b	3.6	1.501	0.265	10.0	1.35	0.384
HAT-P-26 b	4.5	0.689	0.069	10.0	1.29	0.383
WASP-107 b	3.6	9.628	0.010	95.0	1.30	0.384
WASP-107 b	4.5	4.939	0.048	15.0	1.26	0.385
WASP-13 b	3.6	0.319	0.263	55.0	1.25	0.383
WASP-13 b	4.5	0.137	0.060	10.0	1.26	0.384
WASP-121 b	3.6	0.585	0.248	45.0	1.13	0.384
WASP-121 b	4.5	0.343	0.070	30.0	1.08	0.382
WASP-69 b	3.6	0.078	0.008	30.0	1.25	0.383
WASP-69 b	4.5	0.057	0.009	25.0	1.21	0.382
WASP-67 b	3.6	0.548	0.193	45.0	1.33	0.385
WASP-67 b	4.5	0.196	0.075	30.0	1.24	0.385
HATS-7 b	3.6	0.039	0.240	35.0	1.38	0.386
HATS-7 b	4.5	0.017	0.056	30.0	1.40	0.385
WASP-29 b	3.6	1.719	0.274	70.0	1.35	0.384
WASP-29 b	4.5	0.822	0.054	10.0	1.22	0.381
HAT-P-41 b	3.6	0.403	0.221	30.0	1.31	0.382
HAT-P-41 b	4.5	0.201	0.061	150.0	1.27	0.384
WASP-101 b	3.6	0.231	0.261	30.0	1.33	0.385
WASP-101 b	4.5	0.140	0.064	30.0	1.21	0.384
WASP-131 b	3.6	0.027	0.304	30.0	1.26	0.383
WASP-131 b	4.5	0.033	0.068	35.0	1.25	0.383
WASP-36 b	3.6	0.001	0.320	110.0	1.49	0.384
WASP-36 b	4.5	0.003	0.075	40.0	1.42	0.383
WASP-63 b	3.6	0.298	0.307	60.0	1.30	0.385
WASP-63 b	4.5	0.107	0.058	10.0	1.23	0.384
WASP-79 b	3.6	0.169	0.291	35.0	1.45	0.385
WASP-79 b	4.5	0.158	0.062	10.0	1.22	0.385
WASP-94 Ab	3.6	0.591	0.268	105.0	1.35	0.384
WASP-94 Ab	4.5	0.348	0.065	30.0	1.21	0.385
WASP-74 b	3.6	0.894	0.008	90.0	1.26	0.384
WASP-74 b	4.5	0.560	0.007	70.0	1.24	0.384
WASP-62 b	3.6	0.373	0.255	85.0	1.47	0.384
WASP-62 b	4.5	0.239	0.064	40.0	1.21	0.384
KELT-7 b	3.6	0.248	0.009	60.0	1.29	0.384
KELT-7 b	4.5	0.182	0.007	50.0	1.21	0.382
Kepler-45 b	3.6	0.022	0.277	30.0	1.50	0.383
Kepler-45 b	3.6	0.021	0.280	10.0	1.55	0.384
Kepler-45 b	3.6	0.026	0.269	40.0	1.71	0.384
Kepler-45 b	3.6	0.024	0.265	20.0	1.78	0.384
Kepler-45 b	4.5	0.005	0.047	20.0	1.44	0.384
Kepler-45 b	4.5	0.006	0.065	20.0	1.51	0.383
Kepler-45 b	4.5	0.008	0.059	20.0	1.41	0.383
Kepler-45 b	4.5	0.005	0.052	20.0	1.46	0.385

Appendix B: VULCAN validation on HD 209458b

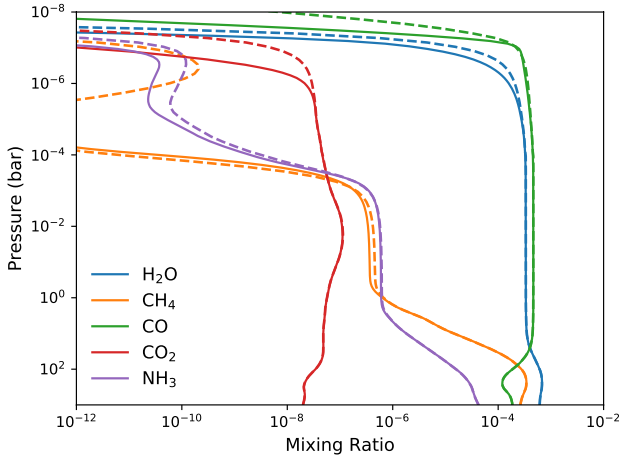


Fig. B.1. Abundance mixing ratios at different pressures for the main species in the *Spitzer* bandpasses in HD 209458 b. The solid line shows the results from our VULCAN calculation and the dashed line the results from Moses et al. (2011). The temperature and eddy-diffusion structure are taken the same as the dayside-average P-T profile in Moses et al. (2011). The solar flux is also used as an analog for HD 290458 at a distance of 0.04747 AU.

Appendix C: Radius anomaly

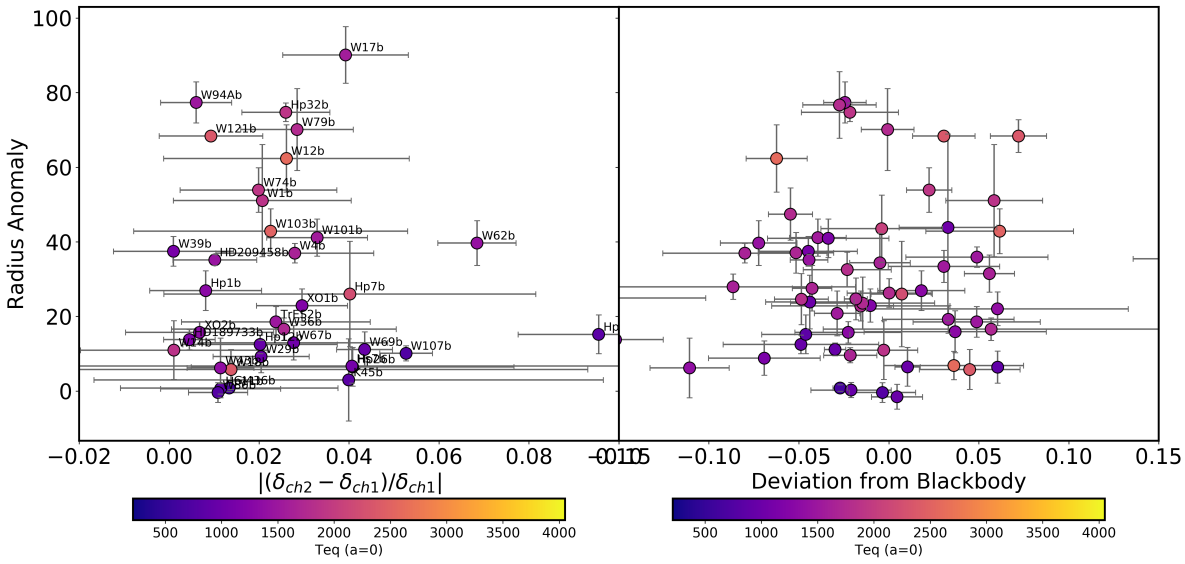


Fig. C.1. Radius anomaly (calculated using models from Thorngren et al. (2016) and Thorngren & Fortney (2018) against the absolute value of the normalized difference in transit depths for the available planets. The color scale is the equilibrium temperature of the planet.